REPORT DOCUMENTATION PAGE

Form Approved
OMB No. 0704-0188

1. AGENCY USE ONLY *(Leave blank)*	2. REPORT DATE	3. REPORT TYPE AND DATES COVERED
	March 1996	

4. TITLE AND SUBTITLE

Electron Spin Relaxation in Irradiated Solids

5. FUNDING NUMBERS

6. AUTHOR(S)

Barnard Tongjoo Ghim

7. PERFORMING ORGANIZATION NAME(S) AND ADDRESS(ES)

AFIT Student Attending:

University of Denver

8. PERFORMING ORGANIZATION REPORT NUMBER

96-002D

9. SPONSORING / MONITORING AGENCY NAME(S) AND ADDRESS(ES)

DEPARTMENT OF THE AIR FORCE
AFIT/CI
2950 P STREET, BLDG 125
WRIGHT-PATTERSON AFB OH 45433-7765

10. SPONSORING / MONITORING AGENCY REPORT NUMBER

11. SUPPLEMENTARY NOTES

12a. DISTRIBUTION / AVAILABILITY STATEMENT

Approved for Public Release IAW AFR 190-1
Distribution Unlimited
BRIAN D. GAUTHIER, MSgt, USAF
Chief Administration

12b. DISTRIBUTION CODE

13. ABSTRACT *(Maximum 200 words)*

14. SUBJECT TERMS

15. NUMBER OF PAGES

163

16. PRICE CODE

17. SECURITY CLASSIFICATION OF REPORT	18. SECURITY CLASSIFICATION OF THIS PAGE	19. SECURITY CLASSIFICATION OF ABSTRACT	20. LIMITATION OF ABSTRACT

GENERAL INSTRUCTIONS FOR COMPLETING SF 298

The Report Documentation Page (RDP) is used in announcing and cataloging reports. It is important that this information be consistent with the rest of the report, particularly the cover and title page. Instructions for filling in each block of the form follow. It is important to ***stay within the lines*** to meet ***optical scanning requirements***.

Block 1. Agency Use Only *(Leave blank)*.

Block 2. Report Date. Full publication date including day, month, and year, if available (e.g. 1 Jan 88). Must cite at least the year.

Block 3. Type of Report and Dates Covered. State whether report is interim, final, etc. If applicable, enter inclusive report dates (e.g. 10 Jun 87 - 30 Jun 88).

Block 4. Title and Subtitle. A title is taken from the part of the report that provides the most meaningful and complete information. When a report is prepared in more than one volume, repeat the primary title, add volume number, and include subtitle for the specific volume. On classified documents enter the title classification in parentheses.

Block 5. Funding Numbers. To include contract and grant numbers; may include program element number(s), project number(s), task number(s), and work unit number(s). Use the following labels:

C	- Contract	**PR**	- Project
G	- Grant	**TA**	- Task
PE	- Program Element	**WU**	- Work Unit Accession No.

Block 6. Author(s). Name(s) of person(s) responsible for writing the report, performing the research, or credited with the content of the report. If editor or compiler, this should follow the name(s).

Block 7. Performing Organization Name(s) and Address(es). Self-explanatory.

Block 8. Performing Organization Report Number. Enter the unique alphanumeric report number(s) assigned by the organization performing the report.

Block 9. Sponsoring/Monitoring Agency Name(s) and Address(es). Self-explanatory.

Block 10. Sponsoring/Monitoring Agency Report Number. *(If known)*

Block 11. Supplementary Notes. Enter information not included elsewhere such as: Prepared in cooperation with...; Trans. of...; To be published in.... When a report is revised, include a statement whether the new report supersedes or supplements the older report.

Block 12a. Distribution/Availability Statement. Denotes public availability or limitations. Cite any availability to the public. Enter additional limitations or special markings in all capitals (e.g. NOFORN, REL, ITAR).

- **DOD** - See DoDD 5230.24, "Distribution Statements on Technical Documents."
- **DOE** - See authorities.
- **NASA** - See Handbook NHB 2200.2.
- **NTIS** - Leave blank.

Block 12b. Distribution Code.

- **DOD** - Leave blank.
- **DOE** - Enter DOE distribution categories from the Standard Distribution for Unclassified Scientific and Technical Reports.
- **NASA** - Leave blank.
- **NTIS** - Leave blank.

Block 13. Abstract. Include a brief *(Maximum 200 words)* factual summary of the most significant information contained in the report.

Block 14. Subject Terms. Keywords or phrases identifying major subjects in the report.

Block 15. Number of Pages. Enter the total number of pages.

Block 16. Price Code. Enter appropriate price code *(NTIS only)*.

Blocks 17. - 19. Security Classifications. Self-explanatory. Enter U.S. Security Classification in accordance with U.S. Security Regulations (i.e., UNCLASSIFIED). If form contains classified information, stamp classification on the top and bottom of the page.

Block 20. Limitation of Abstract. This block must be completed to assign a limitation to the abstract. Enter either UL (unlimited) or SAR (same as report). An entry in this block is necessary if the abstract is to be limited. If blank, the abstract is assumed to be unlimited.

★U.S.GPO:1990-0-273-271

Electron Spin Relaxation in Irradiated Solids

A Dissertation

Presented to

the Faculty of Natural Sciences, Mathematics, and Engineering

University of Denver

In Partial Fulfillment

of the Requirements for the Degree

Doctor of Philosophy

by

Barnard Tongjoo Ghim

March 1996

Table of Contents

List of Tables

List of Figures

Abbreviations used in text

A	amp (unit of measure for current)
B	applied magnetic field
C-band	microwave frequency from 4-8 GHz
CPMG	Carr-Purcell-Meiboom-Gill
CW	continuous-wave
ELDOR	electron-electron double resonance
END	electron nuclear dipole
ENDOR	electron-nuclear double resonance
EPR	electron paramagnetic resonance
ESE	electron spin echo
ESEEM	electron spin echo envelope modulation
ESR	electron spin resonance
FID	free induction decay
FT	Fourier transform
G	gauss (unit of measurement for magnetic field)
Gy	gray (unit of measurement for irradiation)
K-band	microwave frequency from 18.0-26.5 GHz
L-band	microwave frequency from 1-2 GHz
LGR	loop gap resonator
NBS	National Bureau of Standards
MFEPR	multi-frequency electron paramagnetic resonance
mT	millitesla (unit of measurement for magnetic field)
PTFE	poly-tetrafluorinoethylene
PTU	programmable timing unit

Q	quality factor
Q-band	microwave frequency from 33-50 GHz
Rad	rad (unit of measure for irradiation)
s	seconds (unit of measure for time)
S-band	microwave frequency from 2-4 GHz
S/N	signal to noise
SR	saturation recovery
STELDOR	stepped-field electron-electron double resonance
T	tesla (unit of measurement for magnetic field)
T_1	spin-lattice relaxation time
T_2	spin-spin relaxation time
T_m	phase memory time
T_x	cross-relaxation time
X-band	microwave frequency from 8-12.4 GHz
W	watt (unit of measure for power)
W_e	electron relaxation rate
W_n	nuclear relaxation rate
W_x	cross-relaxation rate

Acknowledgment

I wish to thank the United States Air Force for sponsoring my degree.

I thank Professors Gareth R. Eaton and Sandra S. Eaton for the opportunity to study EPR under their tutelage, and Seiler Research Laboratories at the United States Air Force Academy for their material support of my project.

I would also like to thank Dr. George A. Rinard and Mr. Richard W. Quine of the Engineering Department for their invaluable help and guidance in this project.

I also owe gratitude to Dr. Jing-Long Du for his work on irradiated L-alanine, Dr. Susanne Pfenninger for her K-band work on irradiated L-alanine and irradiated vitreous silica at the Medical College of Wisconsin, and Dr. Thomas F. Prisner and Dr. Klaus Möbius for their 95 GHz work on irradiated vitreous silica at the Institue für Molekulphysik, Freie Universitat Berlin. I am also indebted to Dr. Lowell Kispert and Dr. Michael Bowman for their discussions at the 18th International EPR symposium, Denver, July 1995.

I would also like to acknowledge Cobe Laboratories, Lakewood, Colorado, for irradiating the samples used in this study, and the National Science Foundation and the National Institute of Health for their funding for the contributions of Richard Quine and George Rinard.

CHAPTER ONE

Introduction

Electron Paramagnetic Resonance (EPR) was discovered in 1944 by Zavoisky in Kazan and by Bleaney at Oxford and has proven to be the premier method for studying the characteristics of chemical species with unpaired electrons. Initially EPR was done at very low frequencies, but by 1947, EPR experiments were conducted around 9 GHz. Since then, most EPR work (with some notable exceptions) has been accomplished at X-band (8-12.5 GHz) microwave frequencies. There are compelling reasons to use frequencies lower than X-band. Lower microwave frequencies have been shown to enhance resolution of some hyperfine components in some materials, especially copper complexes, by reducing anisotropic effects (*1*). Many materials have less dielectric loss at lower microwave frequencies, which permits study of larger amounts of lossy materials, including for example, animals.

Since the instrumentation was not commercially available, this need for observing EPR at lower frequencies at the University of Denver has translated to a flexible instrument called the Multi-Frequency EPR (MFEPR). The MFEPR is an instrument with a Q-band (35 GHz) bridge and three lower frequency microwave bridges built at the University of Denver. The three lower frequency bridges can be interchanged to allow EPR investigation at L-band (1-2 GHz); S-band (2-4 GHz); and C-Band (4-8 GHz). There are small differences among the lower frequency bridges, but the overall design of the bridges is consistent throughout the three bridges. This is the first spectrometer designed and built to perform

Continuous Wave (CW), Electron Spin Echo (ESE), Electron-Electron Double Resonance (ELDOR), and Saturation-Recovery (SR) spectroscopy. The fundamental design philosophy was that the same microwave bridge was to be used for CW, ESE, and SR experiments by only changing front panel switches, and specifically without requiring the operator to break any microwave connections or change modules *(2)*. This bridge design coupled with a versatile programmable timing unit (PTU) provides a powerful tool for low frequency EPR *(3)*.

This dissertation is separated into six parts. The first part (chapter 2) is a general description of the principles of EPR and an overview of some of the experiments reported in subsequent sections. The techniques discussed include CW; 2-pulse spin echo to measure the phase memory time, T_m; 2-pulse spin-echo field-swept absorption; 3-pulse inversion-recovery spin-echo; 3-pulse spin-echo to measure electron spin-echo envelope modulation; long-pulse saturation with spin-echo detection of the recovery; and long-pulse SR.

The second part (chapter 3) describes the design and fabrication of copper-film loop-gap resonators (LGR) for the MFEPR system *(4)*. The goal was to build an LGR that would pass a very rapid magnetic field step required in the pulsed Stepped field Electron-Electron Double Resonance (STELDOR) experiments (*5-12*). This effort was successful and the specifics of the pulsed STELDOR LGR are discussed in chapter six. Along the way to developing the pulsed STELDOR LGR, the copper-film resonators were an integral part of testing the MFEPR.

Part three (chapters 4 and 5) describes room-temperature multi-frequency time domain study of the electron spin relaxation of irradiated fused vitreous silica and irradiated L-alanine. Few measurements are available that comprehensively describe the spin relaxation in any chemical system. The goal was to measure (and

understand) some of the many contributions to spin relaxation and spin diffusion. These samples were chosen because of their inherent interest and because the radicals were sufficiently persistent at room temperature to facilitate method development. The magnetic field and frequency dependence of electron spin relaxation times of the E' center in irradiated vitreous silica provide the data necessary for using the irradiated quartz standard sample as a testing standard for time-domain EPR instrumentation for other frequencies than X-band *(13)*. The multifrequency EPR of irradiated L-alanine showed that the lower frequency CW results were consistent with the assignment of the satellite lines present at X-band as spin-flip transitions *(14, 15)*. The comparison of the apparent recovery times for irradiated L-alanine obtained by inversion recovery, 3-pulse spin echo, and long pulse saturation recovery methods revealed how the presence of spectral diffusion can be a major contributor to the time dependence of the signal depending on the method of T_1 measurement. The studies of relaxation for the two materials provided valuable insight into the diverse environments of the electron spins in two different samples.

Part four (chapters 6 and 7) presents the development and use of a pulsed stepped-field electron-electron double resonance (STELDOR) system (*5*) and a two-frequency pulsed ELDOR technique to study relaxation processes in irradiated L-alanine (*16*). The pulsed STELDOR copper film LGR is fully described as is the hardware to produce the very rapid (approximately 200 ns duration) 26 gauss (1 gauss = 10^{-4} Tesla) field jump.

Chapter 7 describes the results from the two-frequency pulsed ELDOR study. The first pulse of the inversion recovery echo sequence was at one microwave frequency, and the subsequent two-pulse sequence was at a different

microwave frequency. The two-frequency pulsed ELDOR experiments and pulsed STELDOR experiments under comparable conditions yielded identical results. The two-frequency ELDOR yielded even more interesting results when a long, low power (compared to the subsequent pulses) saturating first pulse was used in the saturation ESE detected recovery sequence, a reduction as well as an enhancement of the spin echo amplitude was found for irradiated L-alanine.

Part five (chapter 8) is the analysis of the relaxation behavior of irradiated organic solids based on all of the accumulated data on the irradiated organic radicals. A model involving four relaxation rates among four energy levels is presented as an approximation to the L-alanine spin system. Simulation of SR, pulsed STELDOR, and pulsed two-frequency ELDOR results using this model provides a basis for assigning the relaxation times in some of these irradiated organic solids. The multi-frequency and multi-technique relaxation measurements give a more detailed and comprehensive picture of the spin relaxation and spin diffusion in these systems than in any other.

The last part (chapter 9) is a brief listing of future work envisioned for the MFEPR, LGR development, and extending the study of relaxation in organic radicals. The MFEPR is a versatile, powerful analytic instrument and further extensions of its usefulness are possible. The latest two-frequency ELDOR shows great potential for studying a variety of samples, and great advances are possible in the development of cryogenic temperature capability. The possibilities are great for the MFEPR.

REFERENCES

1. J. S. Hyde and W. Froncisz, *Ann. Rev. Biophys. Bioeng.* **11**, 391 (1982).

2. R. W. Quine, G. A. Rinard, B. T. Ghim, S. S. Eaton, and G. R. Eaton, to be published.

3. R. W. Quine, S. S. Eaton, and G. R. Eaton, to be published.

4. B. T. Ghim, G. A. Rinard, R. W. Quine, S. S. Eaton, and G. R. Eaton, submitted for publication.

5. J. Gorcester and J. H. Freed, *J. Chem. Phys.* **88,** 4678 (1988).

6. S. K. Rengan, V. R. Bhagat, V. S. S. Sastry and B. Venkataraman. *J. Magn. Reson.* **33**, 227 (1979).

7. J. P. Hornak and J. H. Freed, *Chem. Phys. Lett.* **101**, 115 (1983).

8. S. Pfenninger, A. Schweiger, J. Forrer, and R. R Ernst, *XXIII Con. Amp. on Magn. Res.* 568 (1986).

9. G. A. Sierra, A. Schweiger, and R. R. Ernst, *Chem. Phys. Lett.* **184**, 363 (1991).

10. A. Schweiger, *in* "Modern Pulsed and Continuous-wave Electron Spin Resonance", (L. Kevan and M. K. Bowman eds.) John Wiley & Sons, New York, 43 (1990).

11. P. T. Callaghan, A. Coy, E. Dormann, R. Ruf, and N. Kaplan, *J. Magn. Res.* A., **111**, 127 (1994).

12. S. A. Dzuba, A. G. Maryasov, K. M. Salikhov, and Y. D. Tsvetkov, *J. Magn. Res.*, **58,** 95 (1984).

13. B. T. Ghim, S. S. Eaton, G. R. Eaton, R. W. Quine, G. A. Rinard, and S. Pfenninger, *J. Magn. Reson.* A, **115**, 230 (1995).

14. B. T. Ghim, J-L. Du, S. Pfenninger, G. A. Rinard, R. W. Quine, S. S. Eaton, and G. R. Eaton, *Appl. Radiat. Iso.*, accepted for publication.

15. J. M. Arber, P. H. G. Sharpe, H. A. Joly, J. R. Morton, and K. F. Preston, *Appl. Radiat. Isot.* **42**, 665 (1991).

16. B. T. Ghim, G. A. Rinard, R. W. Quine, S. S. Eaton, and G. R. Eaton, to be published.

CHAPTER TWO

Introduction to Electron Paramagnetic Resonance Spectroscopy

2.1 Principles of Continuous Wave (CW) EPR

EPR (also called Electron Spin Resonance (ESR)) spectroscopy is the foremost method of analysis in various materials with unpaired electrons. The spectroscopic method is based on the Zeeman splitting of the electron energy in a magnetic field. In the simplest case of one electron, the electron spin states can have the m_s quantum numbers, +1/2 and -1/2. The dependence of the Zeeman splitting on magnetic field is shown in Figure 2.1. The energy difference between the $m_s = \pm 1/2$ levels is linearly proportional to the external magnetic field (B_0) with the relationship $\Delta E = g\beta B_0$, where β is the Bohr magneton and g is the scalar g-value (usually around 2 for organic systems).

The Zeeman splitting is inherently interesting, but what gives EPR spectroscopy its power is the coupling of the electron spin with other spin systems; be it other electrons or other nuclei. Figure 2.2 shows the simplest interaction of an unpaired electron coupling with a nucleus with I= ½. The electron-nuclear couplings are referred to as hyperfine coupling and the coupling constant is a_n. These couplings can provide insight into the environment of the unpaired electron. The electron-nuclear interactions are of great interest in the electron spin relaxation studies reported in this dissertation. Detailed discussions of CW EPR can be found in several references (*1,2,3*).

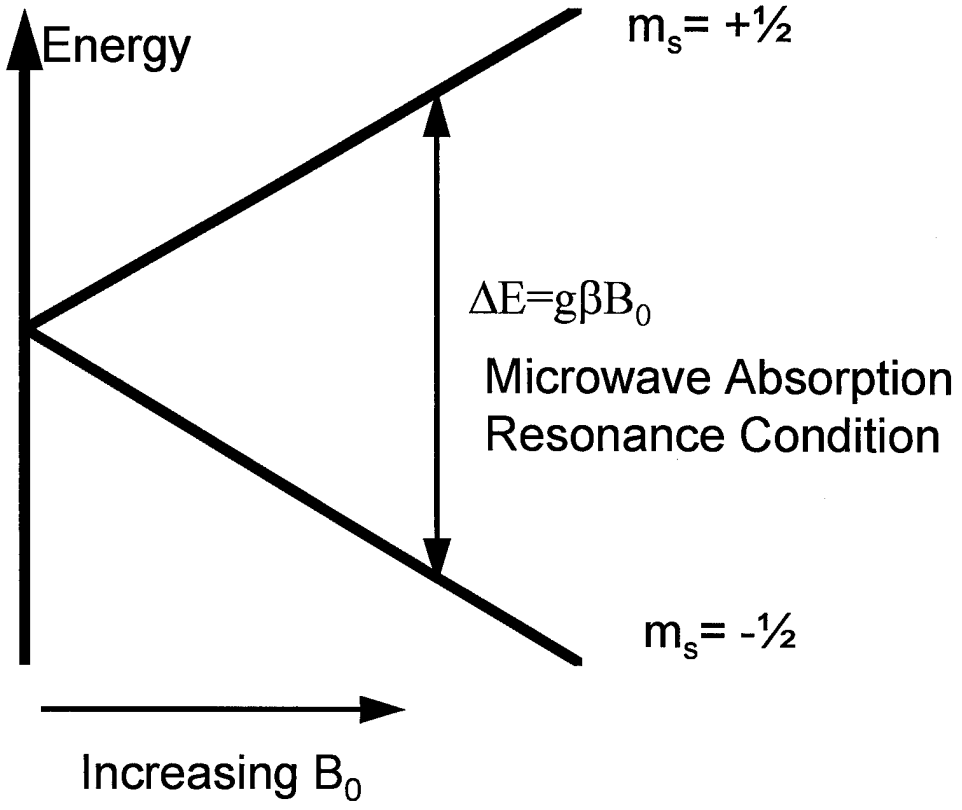

Figure 2.1. Zeeman splitting of the energy levels for one unpaired electron. The CW signal is usually detected as the first derivative of the absorption spectrum because magnetic field modulation (typically 100 KHz), with phase-sensitive detection is used to improve the signal to noise ratio.

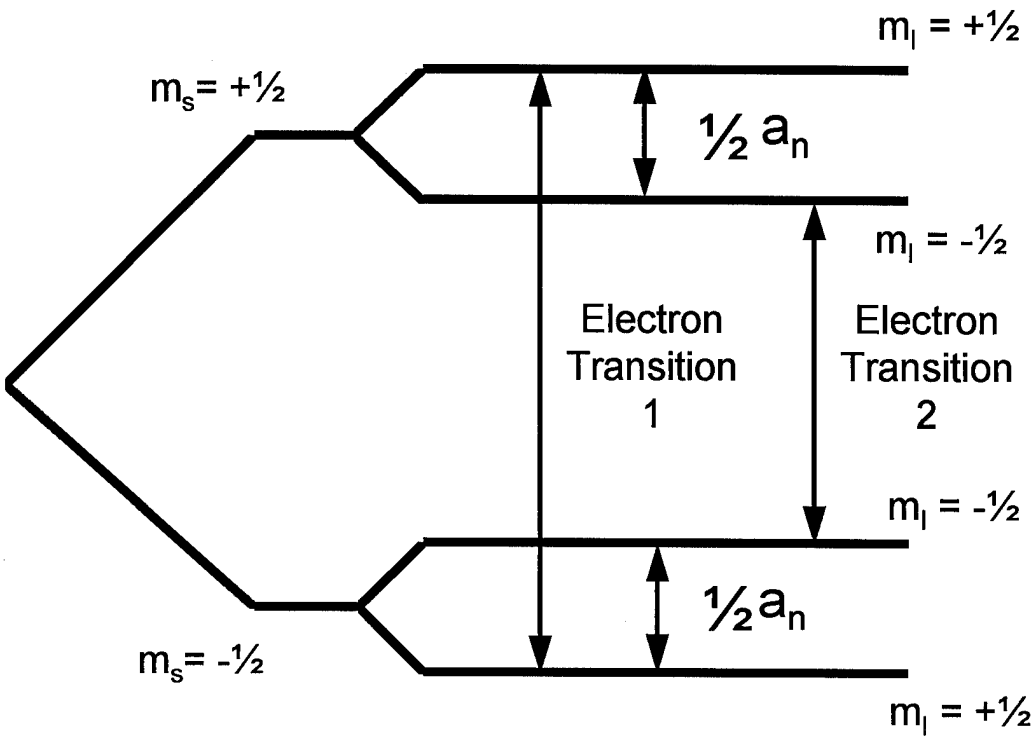

Figure 2.2. Energy level diagram for an unpaired electron coupling to a single nucleus with I = ½. The EPR transitions shown are the allowed transitions that obey the selection rule, $\Delta m_I = 0$, $\Delta m_s = \pm 1$. Allowed NMR transitions obey the selection rule, $\Delta m_s = 0$, $\Delta m_I = \pm 1$.

2.2 Time Domain Electron Spin Echo Experiments

Time domain electron spin echo (ESE) experiments use microwave pulses to alter the population of electron spin energy levels and then to observe the time dependent relaxation of the spin population back to equilibrium. Figure 2.3 shows the formation of a spin echo using a two-pulse spin-echo sequence. The pulse sequence is a 90° ($\pi/2$) microwave pulse, followed time τ_1 later, by a 180° (π) microwave pulse. The representation in Figure 2.3, called the rotating coordinate system, eliminates the time dependence of the microwave magnetic component that is perpendicular to the z-axis. The electron spin resonance frequency is $\omega_0 = \gamma B_0 = 2\pi\nu$ where ω_0 is the angular frequency, γ the gyromagnetic ratio, and ν the microwave frequency. The axes are rotating at frequency ω_0 and only the difference between ω for an individual spin packet and ω_0 is displayed. With reference to this resonance condition, a variety of time domain experiments can be explained more easily. In Figure 2.3a, the net magnetization, M is in equilibrium when the 90° microwave pulse is applied. The application of the 90° magnetic pulse rotates the M vector 90° perpendicular to the application axis of the B_1 vector and the spin vector ends up on the y-axis shown in Figure 2.3b. After time τ_1, due to the inhomogeneity of the spin packet frequencies, some of the spins have started to precess slower and some faster compared to the main body of spins, this is represented as the many vectors comprising M beginning to fan out as shown in Figure 2.3c. After time τ_1, the 180° microwave pulse shown in Figure 2.3d is applied. The 180° microwave pulse moves the spins to the negative y-axis (Figure 2.3e) and the vectors representing the spins begin to come back together forming the spin echo in Figure 2.3f.

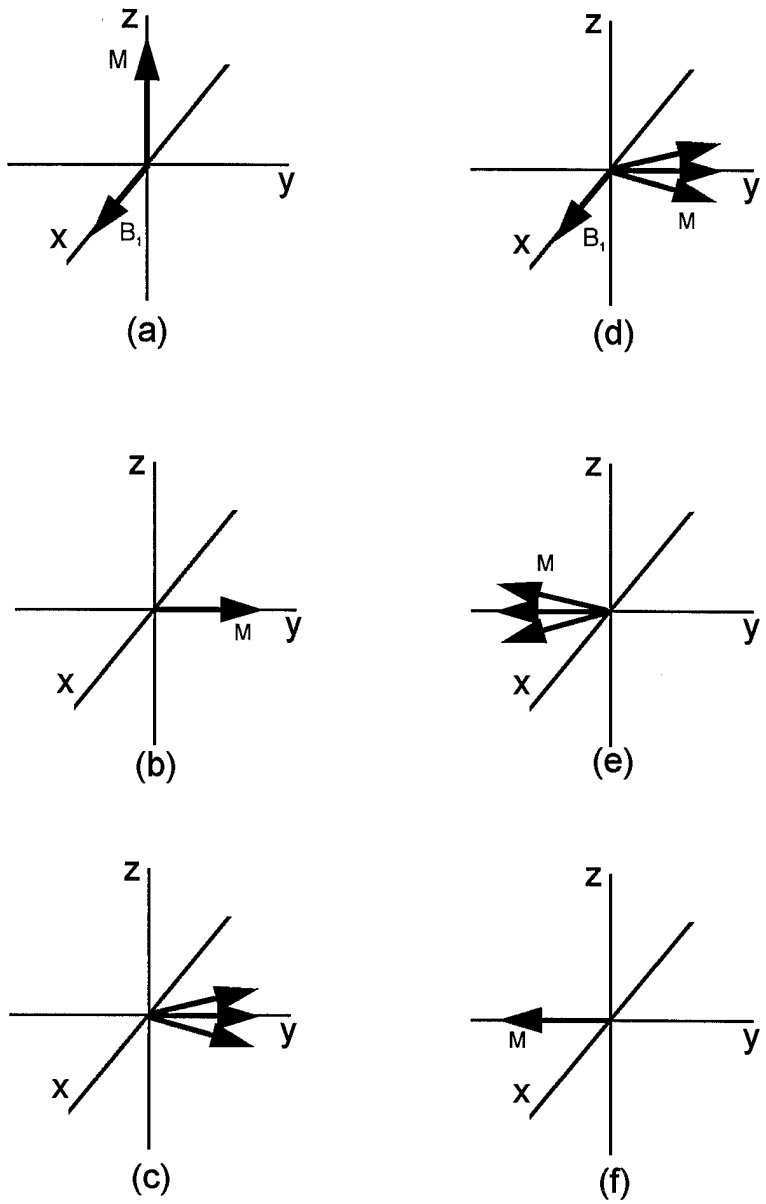

Figure 2.3. Rotating coordinate system showing the formation of a spin-echo. At equilibrium the net magnetization, M, is non-zero due to the difference in Boltzmann populations of the $m_s = \pm$ ½ levels. B_1 is the microwave magnetic field. Electron spins in differing environments exhibit different resonant frequencies that are shown as arrows that fan out. The dynamics of each step in the pulse sequence are discussed in the text.

2.2.1 Definitions

2.2.1.1 Spin-lattice Relaxation Time, T_1

In EPR the spin-lattice relaxation time, T_1, is the time for conversion of the energy absorbed by the spin system to thermal energy in the sample. The time constant is also known as the longitudinal relaxtion time because whenever the z-component is perturbed, in the absence of external influences it will return to the equilibrium value exponentially with the time constant T_1. Spin-lattice relaxation is of critical importance to EPR because without the relaxation process, signals could saturate within the time of the measurement and only transient measurements would be possible. By studying the spin-lattice relaxation characteristics, the interaction between the electron spin and the motions of the lattice can be explored. Also, knowledge of spin-lattice relaxation times can help insure the proper design and execution of EPR experiments.

2.2.1.2 Spin-spin Relaxation Time, T_2

The spin-spin relaxation time, T_2, is the time constant for the loss of net magnetization in the x-y plane. If the net magnetization is rotated to the x-y plane of the rotating frame as in the first pulse of the two-pulse spin-echo sequence shown in 2.3b, the magnetization will decay. The process does not change the energy of the sample, as no transitions are occuring between the levels, but the order of the system is changing. The enthalpy remains constant, but the entropy increases.

2.2.1.3 Cross-relaxation and Spectral Diffusion

Cross-relaxation transitions are electron spin transitions that also involve a nuclear spin transition. In a simple four-level system (consisting of one unpaired electron (S=1/2) coupled with one nucleus (I=1/2)), there are two cross-relaxation transitions, X_1 and X_2, as shown in Figure 2.4.

Spectral diffusion is the transfer of Zeeman energy (spin polarization) from one location in a specrum to another location in the spectrum. When a line is inhomogeneously broadened, it is possible to have transitions that result in a change in electron Zeeman energy with the small difference in energy being taken from or given up to the thermal energy of the system (i.e., translations, vibrations, rotations, and phonons). These transitions can be of many kinds including: almost-allowed electron spin-flips between spins that are slightly different in the net magnetic field of the lattice protons; electron spin-flips between spins that have slightly different zero-field splitting (ZFS) or spin-orbit coupling (SOC) due to local distortions in the lattice. The distinction between cross-relaxation and spectral diffusion is hazy, but in essence, if you know what spin is involved, so that the actual quantum numbers can be used, it is appropriate to call it cross-relaxation. Everything not so specifically defined is called spectral diffusion.

2.2.2 The Time-Domain Experiments

2.2.2.1 2-Pulse spin echo phase-memory time, T_m, measurement

In the 2-pulse spin-echo experiment detailed in Figure 2.3, as the spins precess in the x-y plane shown in Figure 2.3c, there are losses of net magnetization in the x-y plane. These losses of magnetization are called phase-memory relaxation. The time dependence of these losses is measured by monitoring the

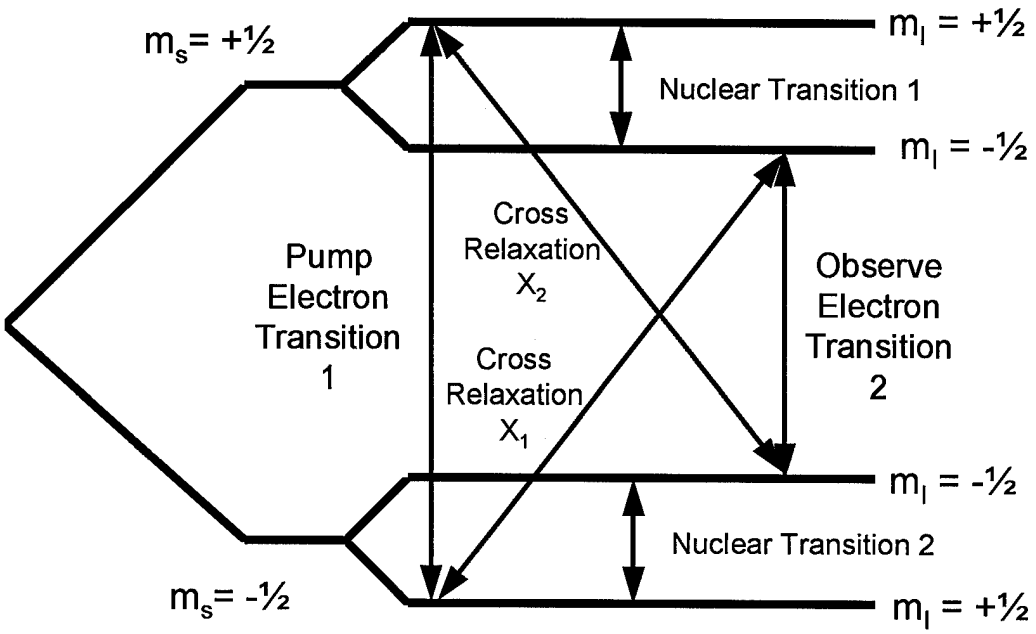

Figure 2.4. Energy level diagram for an unpaired electron coupling to a single nucleus with I =1/2. The cross-relaxation transitions X_1 and X_2 are sometimes referred to as forbidden transitions because they do not obey the selection rule, $\Delta m_I = 0$.

decay of the spin-echo amplitude as a function of time between the first (90°) and second (180°) microwave pulses (τ_1). The timing diagram of the 2-pulse experiment is shown in Figure 2.5. In the solid state, local magnetic fields due to varying environments in the materials make the phase-memory time very fast compared to the spin-lattice relaxation time, T_1.

2.2.2.2 Field swept 2-pulse spin-echo-detected EPR spectrum

This experiment is similar to the 2-pulse spin-echo experiment to measure T_m except that the time τ_1 is kept constant in the experiment and B_0, the magnetic field, is varied. Under certain conditions, this experiment provides the EPR absorption spectrum of the sample being investigated.

2.2.2.3 3-pulse inversion-recovery spin-echo sequence

The inversion-recovery pulse sequence shown in Figure 2.6, involves the addition of an inverting pulse prior to a two-pulse spin-echo sequence described previously. The initial z-axis magnetization vector representing the spins is subjected to a 180° microwave pulse (Fig. 2.7a), and the magnetization is inverted into the negative z axis (Fig. 2.7b). The magnetization is allowed to recover for the time period τ_1 before the second 90° microwave pulse is applied (Fig. 2.7c). When τ_1 is small compared to the recovery time along the z axis (i.e. if the magnetization is still on the negative z-axis as shown in Fig. 2.7c), then the spins are transferred to the -y axis by the 90° microwave pulse (Fig 2.7d). During time τ_2, the spins again start to fan out in the x-y plane (fig. 2.7e). After time τ_2, the 180° microwave pulse is applied (Fig. 2.7f), and the magnetization is transferred to the +y axis (Fig. 2.7g). After time τ_2 following the 180° microwave pulse, the

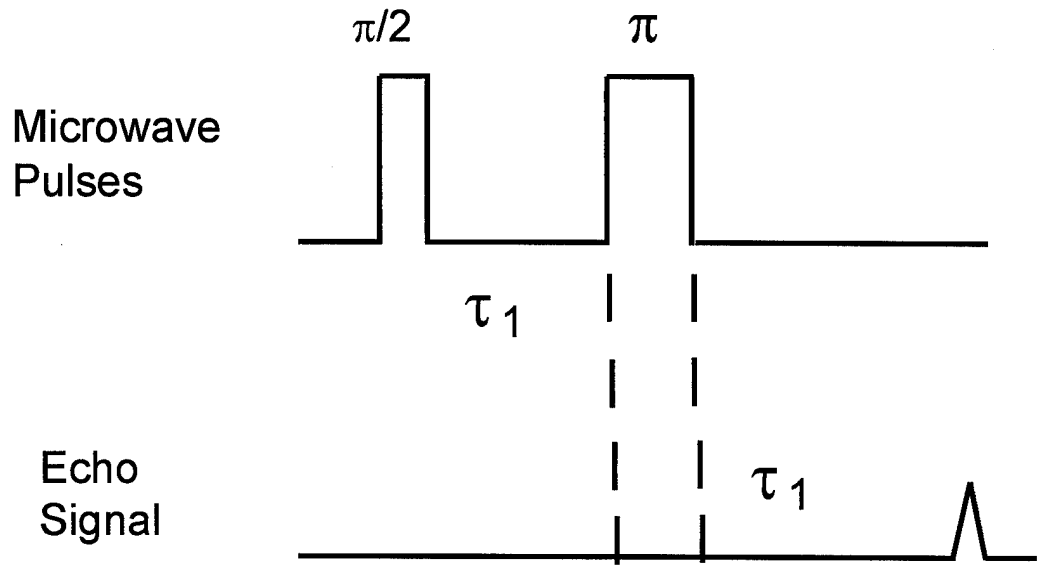

Figure 2.5. Timing diagram for a 2-pulse spin-echo experiment to measure the phase memory time, T_m.

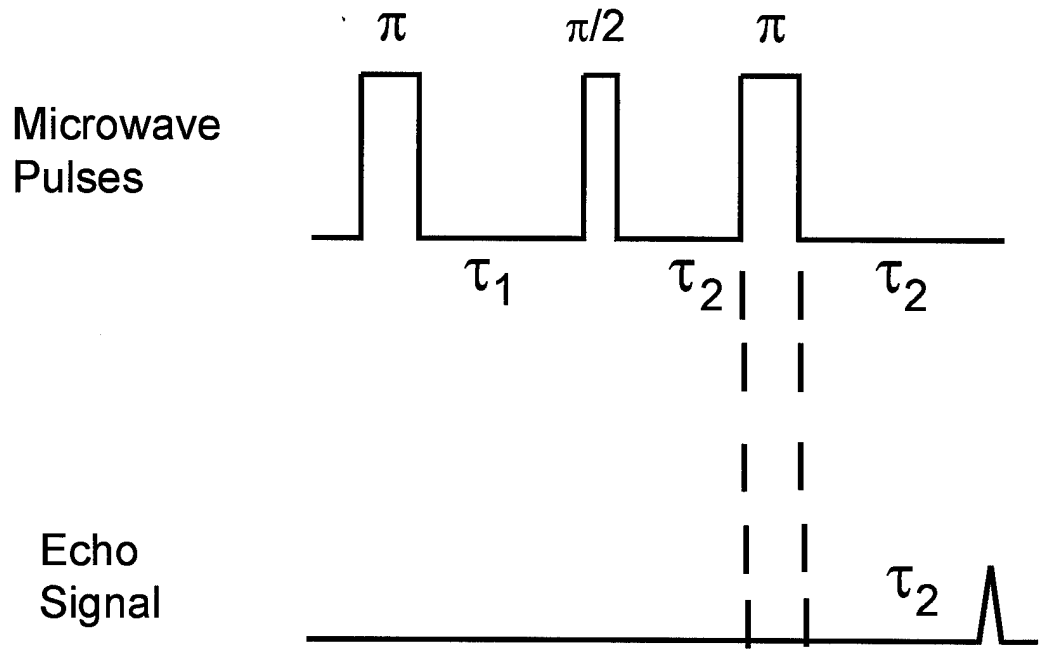

Figure 2.6. Timing diagram for 3- pulse inversion-recovery. The time τ_2 is kept constant throughout the experiment and the amplitude of the spin-echo signal is recorded as a function of the time τ_1.

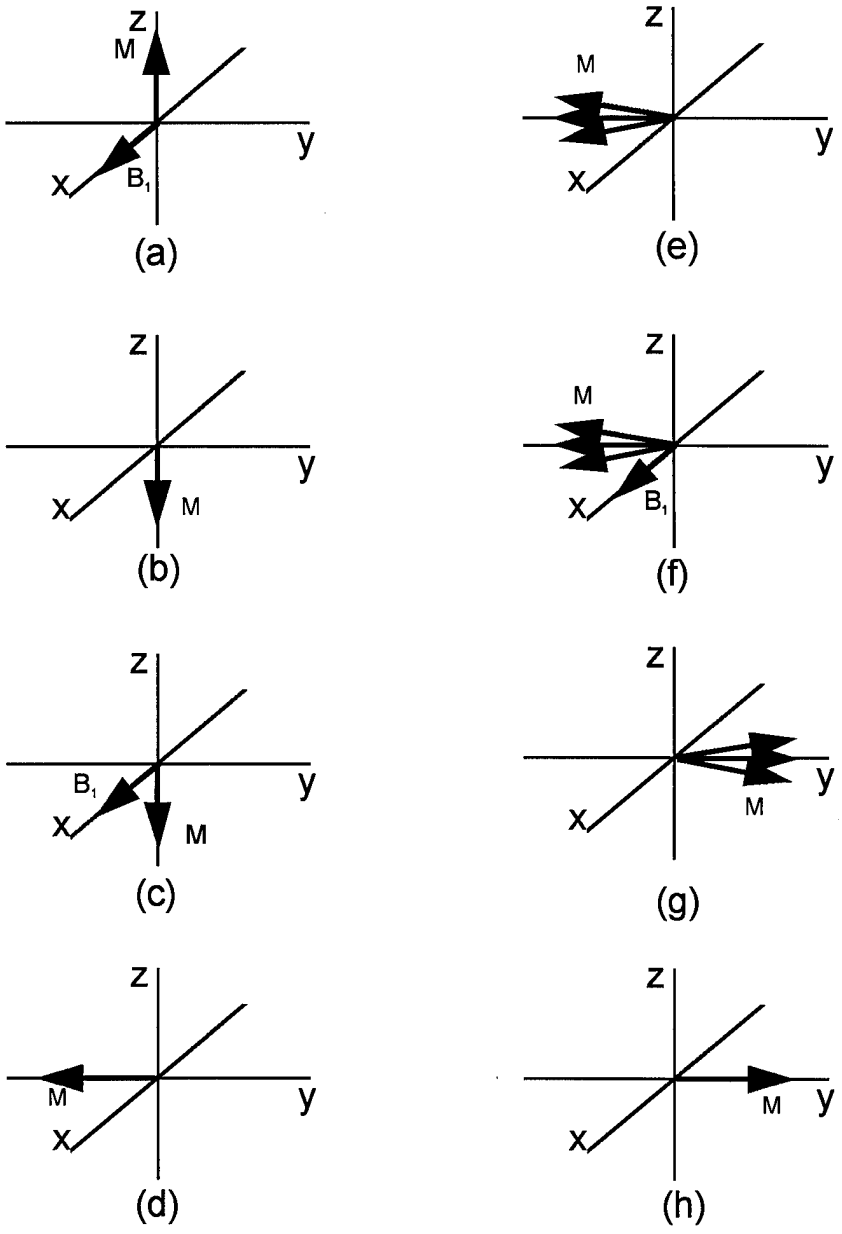

Figure 2.7. 3-pulse Inversion Recovery sequence. As time τ_1 increases, the magnetization shown in (c) recovers from the negative z-axis to the positive z-axis. The recorded signal shows the recovery of the magnetization along the z-axis following the inverting 180° microwave pulse.

spins come together and form the spin echo (Fig. 2.7h). If the time τ_1 is long compared to the recovery time in the z-direction, the spin-echo process follows the same pattern shown in Figure 2.3. The recovery of the z-component magnetization is called the longitudinal spin-lattice relaxation time, T_1. The 3-pulse inversion-recovery sequence is used to measure T_1, but the recovery signal is subject to spectral diffusion and other processes so the time constant may not reflect the true T_1 of the system.

2.2.2.4 3-Pulse spin-echo to measure electron spin-echo envelope modulation

A three pulse spin-echo technique with 90° pulses is used to measure the electron spin-echo envelope modulation (ESEEM) to determine weak nuclear coupling to the unpaired electron (*4*). The sequence shown in Figure 2.8.

2.2.2.5 long pulse saturation with spin-echo detection of the recovery

Frequently, pulsed EPR experiments are a combination of approximately 90° and 180° microwave pulses. In developing the two-frequency pulsed ELDOR system, the spin-echo sequence shown in Figure 2.9 was tried (*5*). The sequence gave recovery times that were identical to the long-pulse saturation recovery.

2.2.2.6 Long-pulse saturation recovery experiments

A long (with respect to T_1) saturating microwave pulse is used to saturate the EPR transition, the pulse is then turned off, and the recovery of CW signal using a low non-saturating microwave power is observed. This CW detection does not use magnetic field modulation. If spectral diffusion is fully saturated, the

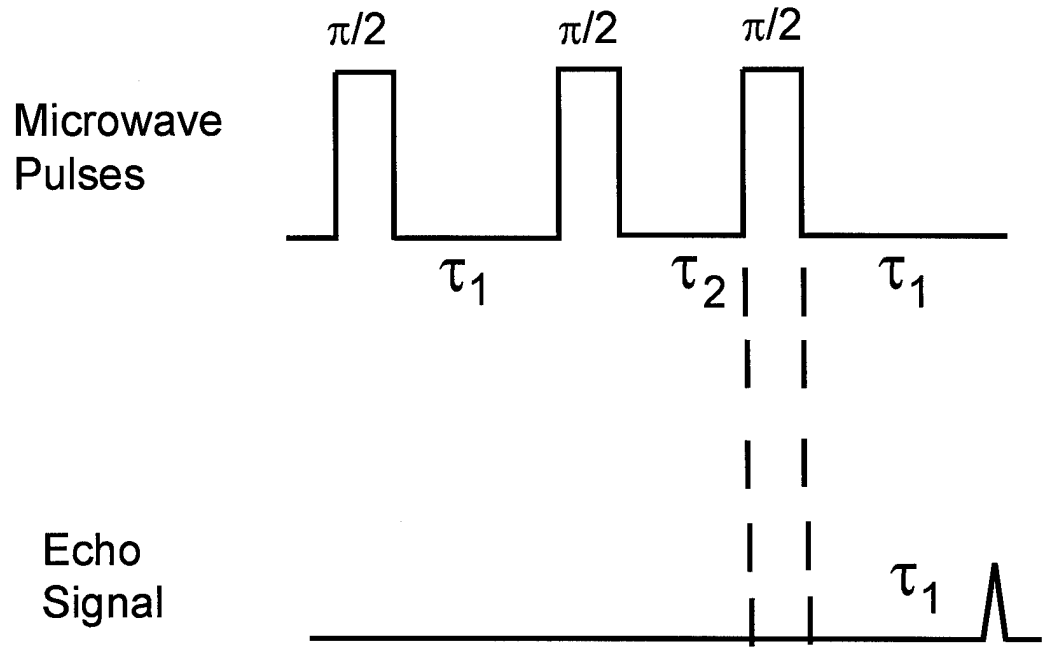

Figure 2.8. 3-pulse spin-echo timing diagram to measure electron spin-echo envelope modulation. The time τ_1 is kept constant in this experiment and the time τ_2 is varied. The spin-echo of interest forms τ_1 after the third 90° microwave pulse, and the echo amplitude is plotted as a function of time τ_2. The decay of the electron spin-echo amplitude is modulated by weak electron-nuclear couplings.

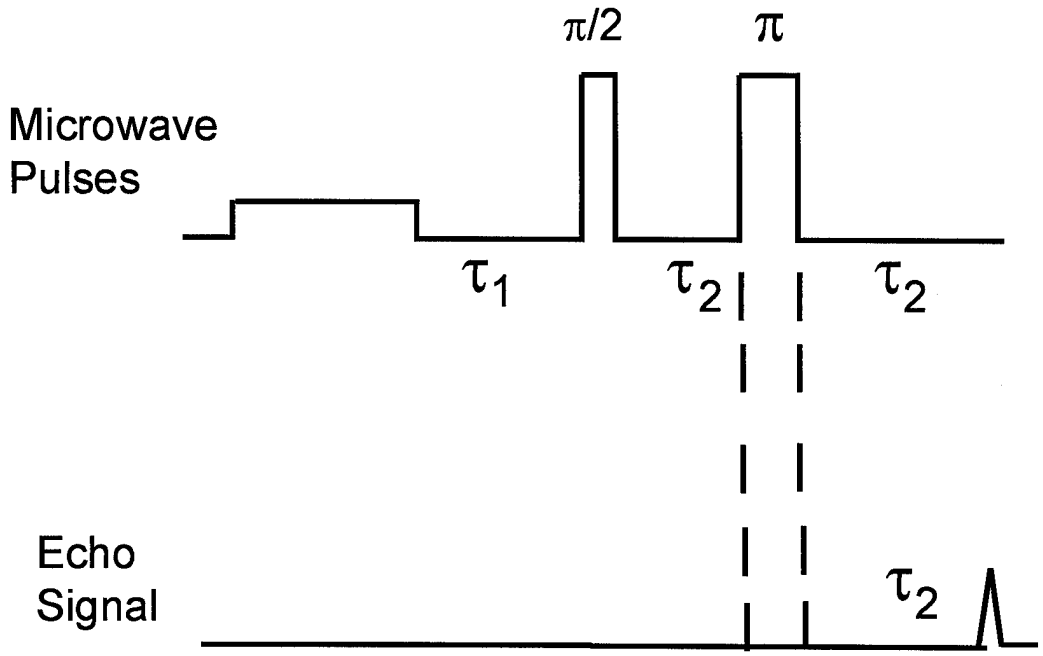

Figure 2.9. Timing diagram for long-pulse saturation with spin-echo detection of the recovery. A lower power long first pulse replaces the first π pulse of an inversion-recovery spin-echo sequence. This sequence was developed to reduce the effects of spectral diffusion on the z-magnetization recovery.

signal recovers with the time constant of T_1 of the spin system. The technique and theory are discussed in detail in the book by Kevan and Schwartz (*4*).

REFERENCES

1. J. E. Wertz, J. R. Bolton, and J. E. Wertz, "Electron Spin Resonance", Wiley-Interscience, New York, 1994.

2. C. P. Slichter, "Principles of Magnetic Resonance", 3rd. edition, Springer-Verlag, Berlin, 1992.

3. C. P. Poole Jr., "Electron Spin Resonance: A Comprehensive Treatise on Experimental Techniques", Wiley-Interscience, 1967, 2nd. edition, Wiley, New York, 1983.

4. L. Kevan and R. N. Schwartz, "Time Domain Electron Spin Resonance", Wiley-Interscience, New York, 1979.

5. A. Schweiger, *Angew. Chemie. Int. Ed. Engl.*, **30**, 265 (1991).

CHAPTER THREE

Design and Fabrication of Copper Film Loop Gap Resonators

3.1 Introduction

Lumped circuit resonators, especially the style of loop-gap-resonators (LGR) described by Hyde and Froncisz, have established a new paradigm for EPR (*1-3*). LGRs are flexible structures, which allows one to design the resonator to fit the experiment, rather than adapt an experiment to a fixed sized or shaped resonator. LGRs can be made much smaller than a cavity resonator for the same frequency, because an LGR's resonant frequency is not based on standing wave geometry as are resonant cavities. The ability to build resonators smaller than the conventional cavity resonator make LGRs attractive for lower frequency EPR, such as L-Band (1-2 GHz) and S-band (2-4 GHz), where resonant cavities can be restrictively large. In this spirit a variety of LGRs and related designs have been reported, including slotted tube resonator (*4*), bridged loop-gap resonator (*5*), copper tape resonator (*6*), folded half-wave resonator (*7*), and re-entrant resonator (*8*). In this chapter we report a versatile LGR design that has a high filling factor and allows high penetration of magnetic field modulation and rapid steps in magnetic field.

3.2 Design and Production

In designing an LGR for CW experiments, minimizing eddy currents and providing maximum penetration of the high frequency field modulation (usually 100 KHz) is paramount. Metal-plated ceramic or quartz LGRs, or solid metal

LGRs with sufficient slots cut into the sample area provide adequate magnetic field modulation penetration for normal CW EPR. With the goal of designing a resonator optimized for pulsed field-jump experiments, we sought to make the conductor using thinner copper than was conventionally made by machining solid copper, and to avoid plating either ceramic or quartz. Since etching copper is a well-established technique, copper film was investigated as a possible material to make LGRs. CuFlon®, manufactured by the Crane company (New Rochelle, NY) consists of copper metal clad to both sides of thin PTFE sheet. It is available in many combinations of copper and dielectric thicknesses. The copper film LGRs, unless otherwise specified, were made from 1 mil (1/1000th inch) thick Teflon coated on both sides with a cladding of 1/8 oz copper per square foot (about 0.167 mil thick copper coating).

The production of the copper film resonator is simple and sufficiently inexpensive to consider the resonator "disposable." The LGR is designed using a computer program based on equations [4] and [5] from reference (*9*) and equation [1]. Within the accuracy of the program, calculations based on equation [1] and calculations based on equation [12] in reference (*9*) gave equivalent results. The inductance L is defined as:

$$L = ((0.2 \times \frac{2r}{z} - 0.45) \times \frac{2r}{z} + 1) \times \mu_0 \times \pi \times r^2 / z \qquad [1]$$

where r is the radius and z the length of the LGR. The program was coded in Basic and is listed in the appendix. Inputs to the calculation are: the radius of the resonator, the length of the resonator, the thickness of the dielectric material, the dielectric constant of the material in the gap, the resonant frequency, and the

scaling factor for drawing the pattern. The program calculates the LGR dimensions for the desired resonant frequency.

Based on the calculated dimensions, the LGR design was laid out using the computer-aided design program AutoCad (Autodesk Inc., Sausalito, CA). Using the Pline feature of the AutoCad program, the front and back side of the photo etch pattern were drawn. Since we were using a reverse process for photoeching, we produced an outline where the conductor (which was to stay on the PTFE substrate) was drawn as clear and the area that was to be etched was drawn in black. The drawing was scaled 4 times larger so when the drawing was photoreduced, the negative would have good resolution. Evenly-spaced black lines were drawn into the pattern to provide slots to pass 100 KHz modulation. The patterns were photoreduced at Cocks-Clark Engraving Co. (2200 Arapahoe, Denver, (303) 292-6242). The process used was negative line work with 4 to 1 reduction produced with emulsion down. The resultant negatives for the two sides of the CuFlon were mounted on 1/10th inch glass frames that positioned the patterns with respect to the CuFlon.

3.2.1 Photoeching

Photoetching used the Shipley negative process. The film negative was dark where the metal was to remain on the copper film. The foremost consideration in the etching process was how well the photoresist adhered to the copper film. The copper film must be clean in order to prevent photoresist failure. Wearing latex gloves throughout the cleaning process of the substrate prevented body oils from being transferred to the copper film. The best method of cleaning was to use BON AMI® (Faultless Starch/Bon Ami Co., Kansas City, MO: a

cleanser containing feldspar and calcite abrasives) with a lint free cloth (Sears® diaper). The surface of the copper must be scrubbed thoroughly until when rinsed with deionized water, the deionized water formed an even layer all over the copper. There should be no dry spots that indicated areas contaminated with oils. After rinsing the cleaned substrate with deionized water, the substrate was placed into a sonicator filled with deionized water with a drop of MICRO® detergent and sonicated for 15 minutes. This assured the BON AMI® cleanser was thoroughly removed from the copper film. The copper film was then rinsed in deionized water and then rinsed with methanol. The methanol was then removed by placing the copper film in a dry stream of air or N_2.

The photoresist used was Microposit PhotoResist S1400-27. **Exposure to white light will degrade the photoresist and all photoresist processes must be done under yellow light conditions.** The photoresist was diluted 1:1 with butyl acetate. The viscosity was reduced so that the copper film could be dipped into the mixture and the excess allowed to run off. A surgical clamp was used to hold the copper film throughout the dipping process. The best method to coat the photoresist was to immerse the whole substrate in the photoresist solution and swirl for 10 seconds. This ensured full contact of the photoresist with the substrate. Then slowly (1 inch per minute), the copper film was pulled out of the photoresist solution. Often, there was a slight beading of the photoresist on the edges of the substrate. As long as there was no beading on the area that was be etched, this was not a problem. Blotting the lowest corner on a Kimwipe® helped maintain the even consistency of the photoresist on the surface. The copper film was allowed to air dry for at least 5 minutes while waiting for the excess to blot away from the corner.

After an even layer of photoresist was placed on the copper film, the copper film was baked in an oven at 80-90 °C for 30 minutes. The copper film was allowed to cool and then taped on to the glass frame to which the negatives were attached and exposed 4 1/2 minutes in the Hamilton vacuum printer, model 55C51. The Hamilton printer has 6 Sylvania F20T12-BL black lights to expose the photoresist sandwiched between the negatives and glass frame. The glass frame was then flipped and exposed again for 4 1/2 minutes. The reverse side of the glass frame was blacked out to prevent exposing the back side. After the exposure, the copper film was developed for 1 minute by swirling in a full strength solution of Microposit Developer MF-319. The developer removed any photoresist exposed to the near-UV light. The copper film was then rinsed in deionized water for 5 minutes to remove the developer. The pattern of the resonator was plainly visible as the darker photoresist unexposed to near-UV light was still on the copper. After the developing, the substrate could be exposed to room light with no degradation. Yellow light conditions no longer are needed after developing the substrate. After developing the substrate, the substrate was placed in an oven at 100-120 °C and baked for 30 minutes. The material was then ready for etching.

The etching process was always faster with the etchant, $FeCl_3$, at a warm temperature. Placing the Archer® etchant (catalog no. 276-1535) in a hot tap water bath expedited the etching process. It took up to 10 minutes of dipping the substrate into the warm etchant before the exposed copper was etched away. The substrate had to be agitated by a continual up and down dipping motion to expedite the copper removal process. After etching, the copper film was rinsed under running water for 1 minute and then rinsed with acetone to remove the

remaining photoresist. After drying, the resonator was ready for assembly. Figure 3.1 shows the regions of copper, after etching, for an S-band copper film resonator. Once patterns had been developed, the predictable and controllable production of LGRs was fast and simple.

3.2.2 Design Considerations

Because a copper film LGR has little structural integrity of its own, it is designed to wrap around a stable structure such as a sample tube (Figure 3.2). It can be fastened by Teflon tape or Teflon shrink tubing. The overlap of the two edges of the copper-clad Teflon creates a "gap". The length of this gap and thus the capacitance of this gap depends on the diameter of the sample tube, and how tightly the copper film is wrapped around the tube. To minimize the effects on capacitance of sample tube variations, most of the LGRs were designed with at least two gaps. The second and subsequent gaps are created by overlapping copper regions on the two surfaces of the Teflon. The dimensions of these gaps are more precisely controlled than the dimensions of the gap formed by wrapping the resonator around the tube. Since series capacitances C_1 and C_2 add in the form $C_{12} = C_1C_2/(C_1+C_2)$, multiple gaps provided more consistent results for resonant frequency and reduced the effects of the variability of sample tubes. At low frequencies, multiple gaps may not be possible in LGRs with small diameters because the lengths of the gaps required would exceed the available circumference of the LGR. For 4 mm diameter 10 mm long copper film LGRs, the experimental resonant frequency of the copper film resonators usually was within $\pm 10\%$ of the predicted (designed) frequency. The greatest deviations were observed at the lowest L-band frequencies and were up to 20%. Errors in frequency up to 40%

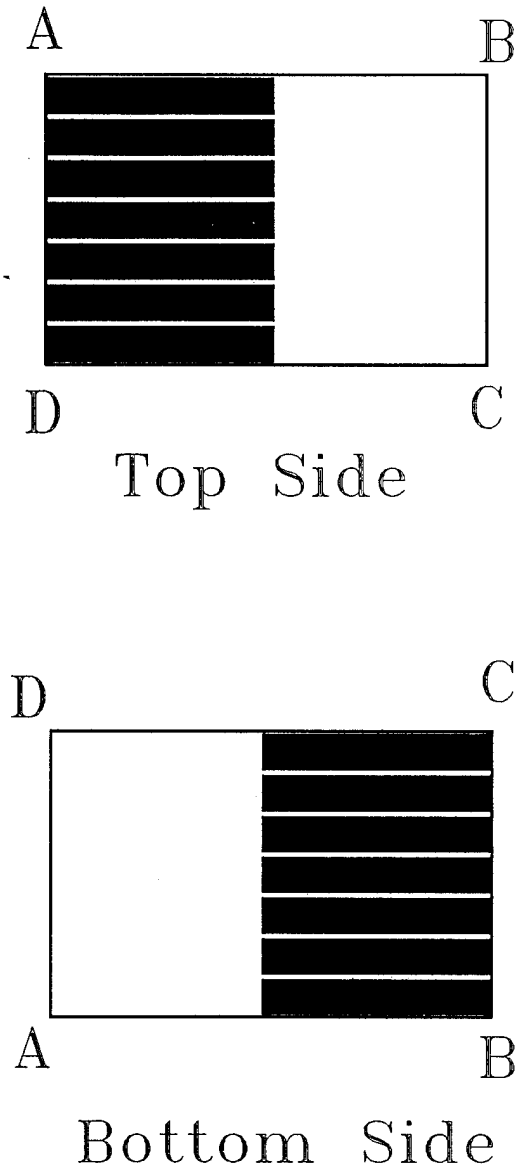

FIG. 3.1. Top and bottom sides of the CuFlon after etching to make an S-band (3.0 GHz) one loop, two-gap copper film LGR. The final resonator was 4 mm diameter by 10 mm long. Points A, B, C, and D are labeled on both parts of the figures. The solid black regions denote the copper on the Teflon substrate. The light lines outline the Teflon regions from which the copper has been etched away.

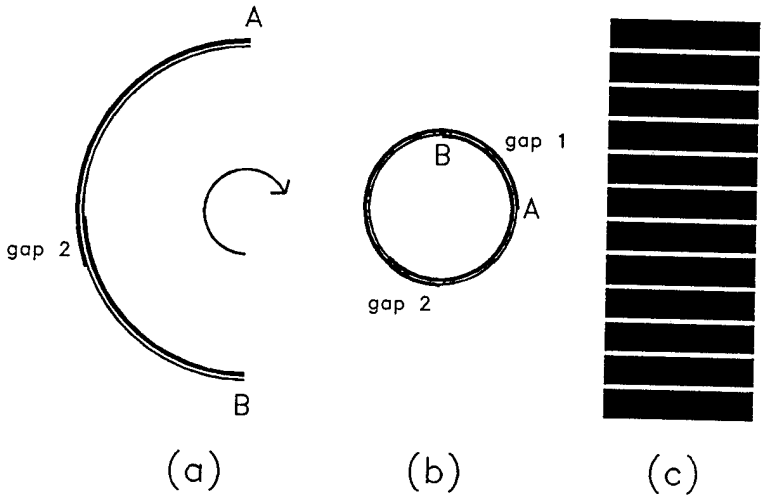

FIG. 3.2. One loop, two-gap, L-band 5.65 mm copper-film LGR. The etched copper film LGR (a) produced as in Fig. 3.1, is wrapped around a sample tube (b). Gap 1 is twice as thick as gap 2 because two layers of Teflon dielectric separate the conductive copper layers in the overlap region. To create the same capacitance in gaps 1 and 2, gap 1 is twice as long as gap 2. (c) is a side view of the assembled resonator showing the etched lines that allow passage of the rapidly changing magnetic field (e. g. 100 KHz magnetic field modulation or magnetic field jump). Labeled points A and B on parts (a) and (b) are the same as in Fig. 3.1. The surface labeled top in Fig. 3.1 becomes the outside of the resonator.

occurred in designing L-band 10 mm diameter, 10 mm long LGRs possibly because equation [12] from reference (*9*) and equation [1] may not properly account for the fringe H field for such a large diameter-to-length ratio.

The sample tube holder assembly is shown in Figure 3.3. The shield was machined from a polymer and painted with silver conductive paint to contain the RF field while allowing penetration of the 100 KHz modulation. The resonators were inductively coupled by a small loop.

Determination of the filling factor requires a full calculation of the field distribution inside the resonator and shield. An approximate calculation was performed, which indicated the filling factor for a sample that completely filled a 4 mm diameter, 10 mm long LGR and extended 10 mm above and below the LGR, was about 0.8. Since most samples are introduced into LGRs in sample tubes, an approximate filling factor calculation for a 3 mm diameter sample size was performed and the filling factor was found to be about 0.4.

3.3 Performance

Copper film LGRs were tested at several frequencies. The characteristics of the LGRs tested are in Table 3.1. The quality factor, Q, was measured using a frequency sweeper, an HP 8410A network analyzer, and associated reflection test units. Q was determined by finding the microwave frequency at the points in the polar display where there was a 3 dB drop in the reflected power, $Q = \frac{\upsilon}{\Delta\upsilon}$. For comparison with experiment, Q was calculated using equation [2], [3], and [5] from reference (*9*). R was calculated by multiplying the sheet resistivity of the copper film by the surface area of the LGR. The experimental values of Q were about 50 percent of the calculated values, possibly due to shield, radiation,

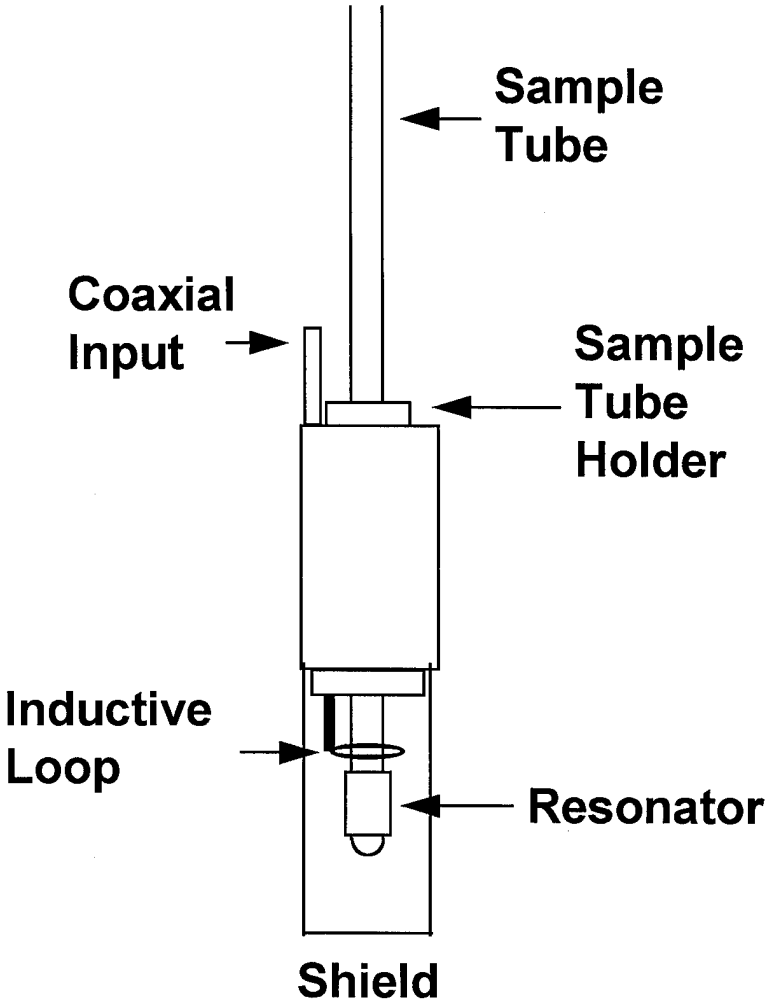

FIG. 3.3. Copper film LGR sample tube holder assembly. The coupling was adjusted by moving the tube up and down and by rotating the tube. For pulsed EPR, the coupling loop was positioned near the middle of the LGR to overcouple the resonator.

Table 3.1: LGR Characteristics

Frequency (GHz)	**Critical Q(loaded)**	**diameter (mm)**	**length (mm)**	**etched gap[a] overlap (mm)**	**number of gaps**
1.10	350	5.7	14	2.0	2
1.73	226	4.0	10	1.2[b]	1
1.88	235	10.0	19	0.2	2
2.10	186	10.0	10	0.4	2
2.66	107	4.0	10	1.04	3
3.05	276	4.0	10	0.51	2
3.25[c]	382	4.0	10	0.46	2
3.27	314	4.0	10	0.46	3
3.66	370	4.0	10	0.53	3
3.79	417	4.0	10	0.33	2
3.80	376	4.0	10	0.53	3
4.39	279	4.0	10	0.18	2
4.90	545	4.0	10	0.13	2
9.40	600	5.7	10	0.2	15

a. gap 2 in Fig. 3.2.

b. For this resonator, there was only one gap, which was created by the overlapping copper film when the LGR was wrapped around the sample tube (gap 1 in Fig 3.2).

c. For this resonator, copper thickness was 1/3 oz per square foot; in all other cases it was 1/8 oz per square foot.

dielectric, and other losses. The experimental values of Q were about 45% of the calculated values of Q using equation [5] from reference (*10*).

Penetration of a rapidly-changing magnetic field through a copper-film resonator was studied. The penetration of the 100 KHz modulation was measured with a 2 mm diameter, 50-turn search coil mounted inside a 4 mm sample tube. There was less than 2 percent attenuation of the 100 KHz modulation in the copper film LGRs. Since one of the design goals was to create a resonator useful in pulsed magnetic field jump studies, tests also were conducted with very rapid field jump. For example a 2.5 mT field jump could be achieved with 36 ns 10-90% rise time with the copper-film resonator. Part of this rise time is due to the impedance of the magnetic field coil assembly. Results from the copper film resonator used in S-band pulsed stepped-field electron-electron double resonance experiments on irradiated L-alanine will be reported separately in chapter 6.

The resonators were tested in continuous wave (CW), electron spin echo (ESE), and saturation recovery (SR) experiments. The performance of the resonators is illustrated with the irradiated vitreous silica standard sample for time domain EPR available from Wilmad Glass (Buena, NJ) (*11*). Copper film LGRs were used in the L-band portion of a multifrequency study of the relaxation times for the E' center in the irradiated vitreous silica sample reported in chapter 4.

In CW mode, the copper film LGR performed well for relatively strong signals. Figure 3.4 shows a C-band CW spectrum of the irradiated vitreous silica standard sample. At L-band, CW signal to noise tests were attempted for a standard weak pitch sample inside a copper film, 5.7 mm diameter, 14 mm long, resonator. The test revealed a background signal near g = 2 that obscured the

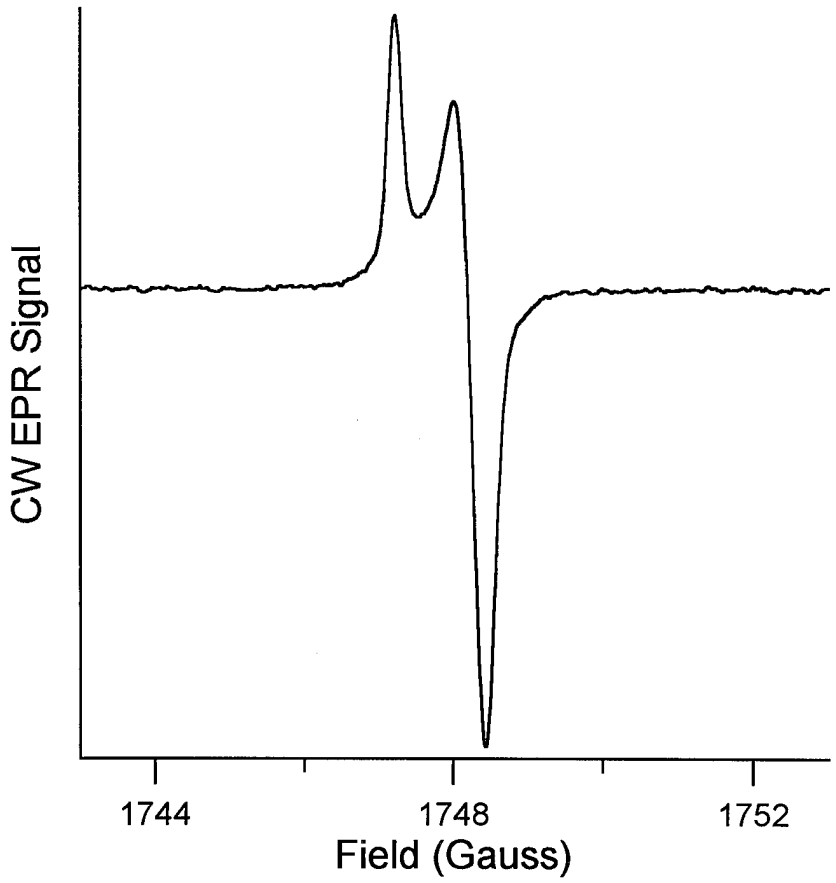

FIG. 3.4. C-band (4.9 GHz) CW spectrum of irradiated standard vitreous silica sample using 4 mm diameter 10 mm long 2-gap copper film LGR. The critically-coupled loaded Q of the resonator was 545. Experimental parameters: power: 90 nW; 100 KHz modulation amplitude, 0.1 gauss; sweep time, 60 s; time constant, 0.128 s.

weak pitch signal. This background signal, which is attributed to impurities in the copper, limits the utility of these resonators for samples with weak signals.

In ESE mode, the copper film LGRs performed very well. The LGRs are easy to overcouple. For example, a 5.65 mm diameter LGR with Q_L= 350 which was designed to hold three of the standard irradiated vitreous silica samples, could be overcoupled to Q = 60. Overcoupling reduces the ring-down time of the resonator, which decreases the dead time. S/N = 200 was obtained at L-band for the echo from a single pulse for 3 irradiated vitreous silica standard samples (Fig. 3.5).

SR was the most difficult test for the CuFlon LGRs. Because of their small thermal mass, the resonant frequency of the copper film LGR had a tendency to drift due to the heating by the microwave power. The frequency drift resulted in a baseline shift that caused errors in the exponential fit of the recovery signal. Allowing the resonator assembly and the bridge to thermally equilibrate solved the drift problem. Figure 3.6 shows L-band SR data using the same assembly as described for the ESE experiments.

3.4 Advantages and Disadvantages

Copper film LGRs are relatively simple and economical to build. The materials are commercially available and the manufacturing process is relatively simple compared to building metal-coated ceramic or quartz resonators. Like most LGRs, the resonators have a high filling factor. The thin copper film and circumferential slots provide high magnetic field modulation penetration. With a small budget, one can quickly develop a large arsenal of resonators for a range of

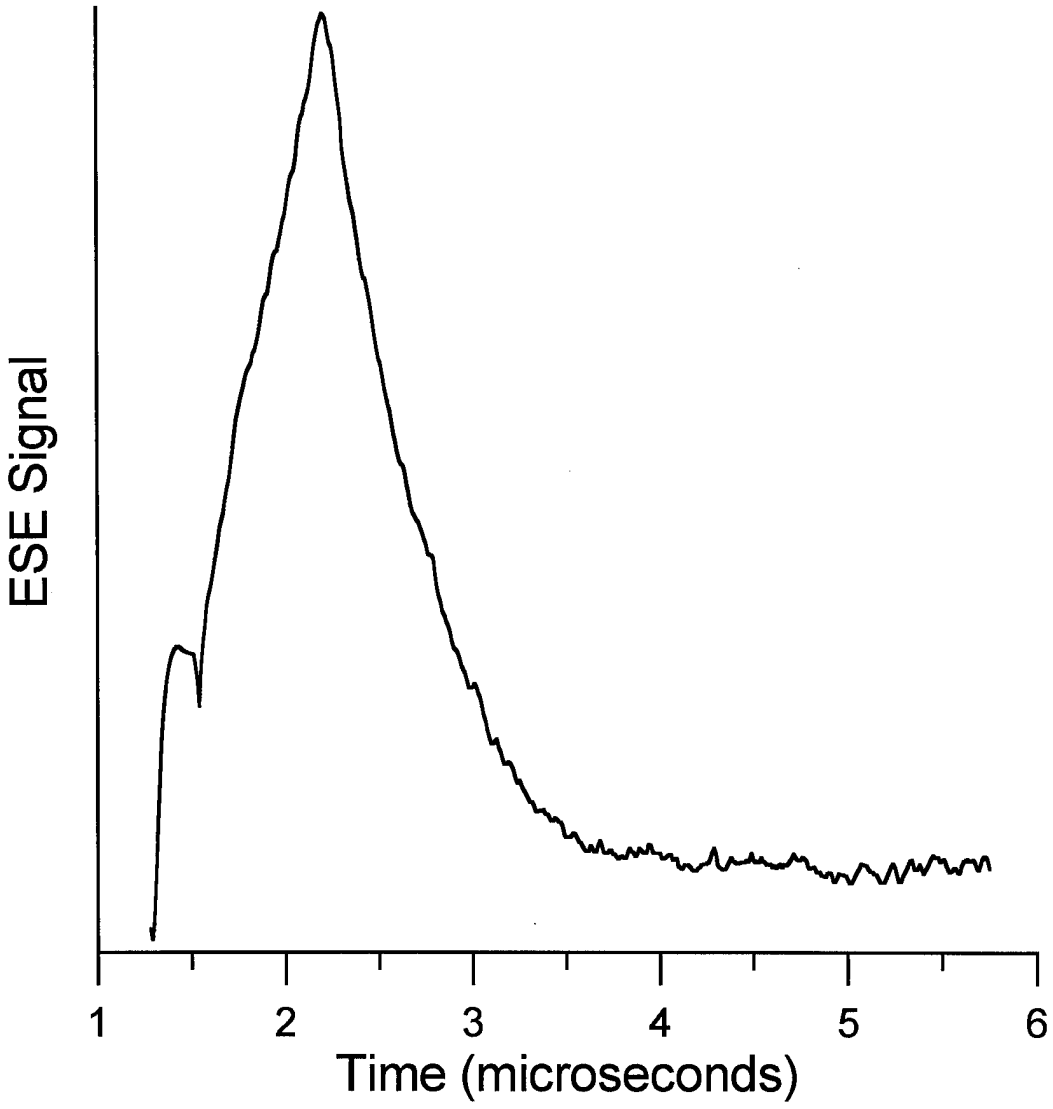

FIG. 3.5. L-band (1.1 GHz) 2-pulse spin echo of three irradiated vitreous silica standard samples using 5.65 mm diameter, 14 mm long 2-gap copper film LGR. Resonator was overcoupled to a loaded Q of 75. A single pulse was digitized with a LeCroy 9310 300 MHz digital oscilloscope. Experimental parameters: pulse lengths, 30-60 ns ($\pi/2$, π sequence); signal height, 0.5 volts.

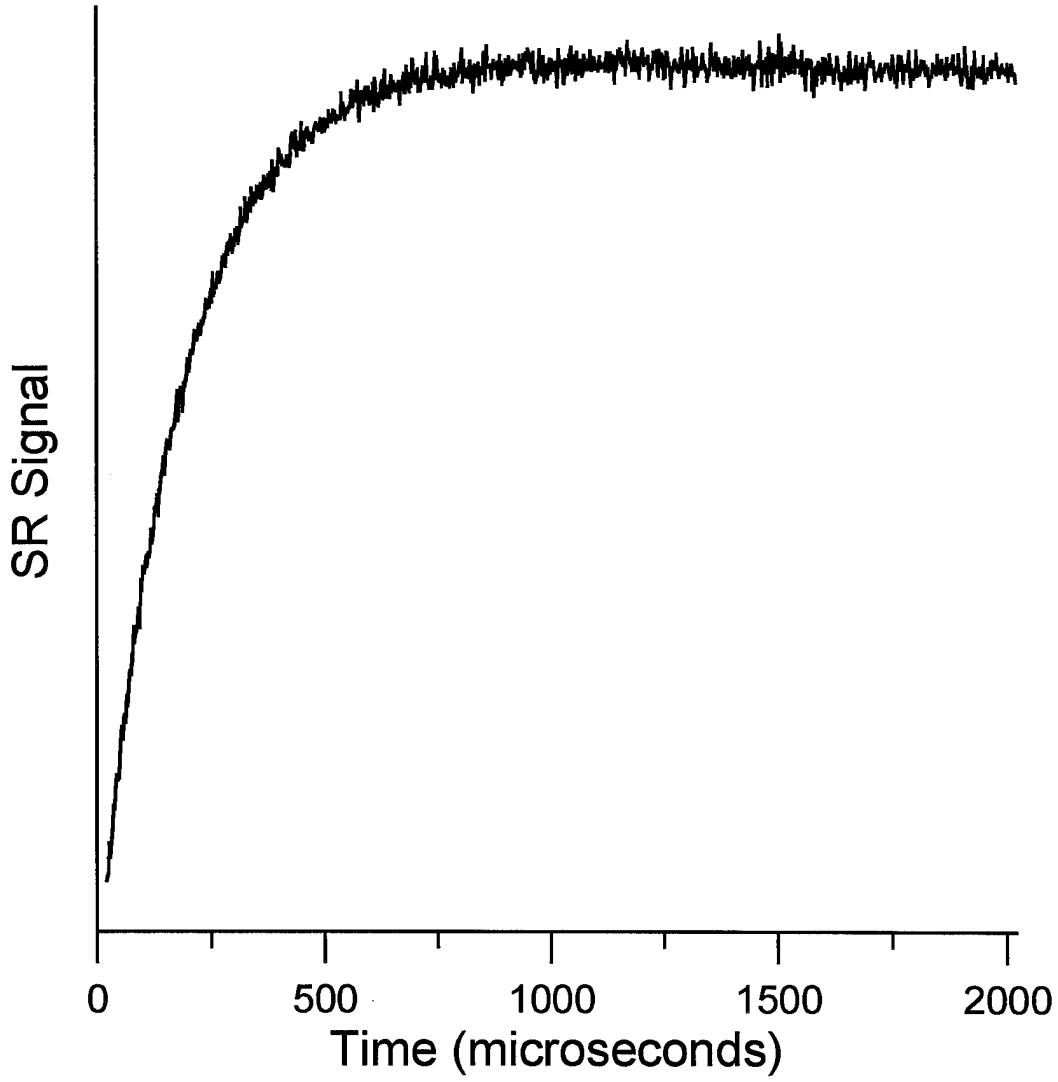

FIG. 3.6. L-band (1.1 GHz) SR data for three irradiated vitreous silica standard samples in 5.65 mm diameter, 14 mm long 2-gap copper film LGR. Experimental parameters: pump power, 10 mW; pump time, 4 μs; observe power, 50 nW; repetition period, 3 ms; number of scans, 10,000; S/N ratio = 112.

microwave frequencies. The copper film resonator can be made to fit the individual experiment and provide a great deal of flexibility.

There are disadvantages to copper film LGRs. The copper film LGRs are temperature sensitive due to the different coefficients of expansion of the quartz tube, the Teflon, and the copper. A five percent change (approximate) in resonant frequency was observed when an L-band resonator was cooled from room temperature to liquid N_2 temperature. Also, passing cooled N_2 over the resonator assembly introduced noise due to the motion of the assembly. The copper introduced a background signal near $g = 2$ making the resonator difficult to use for very sensitive measurements near $g = 2$. Moving a copper-film LGR from one sample tube to another is relatively difficult. Once a resonator was placed on a sample tube, it was best to change samples by cleaning and reusing the same sample tube without disturbing the copper film resonator.

ACKNOWLEDGMENTS

Subsequent to completion of this work, we learned that Dr. Wojciech Froncisz has also used similar materials to construct LGRs.

REFERENCES

1. W. Froncisz and J. S. Hyde, *J. Magn. Reson.*, **47**, 515 (1982).

2. J. S. Hyde and W. Froncisz, *Specialist Periodical Reports on Electron Spin Resonance*, **10**, 175 (1986).

3. J.S. Hyde and W. Froncisz, in "Advanced EPR: Applications in Biology and Biochemistry" (A. J. Hoff, Ed.), Elsevier, Amsterdam, 277 (1989).

4. M. Mehring and F. Freysoldt, *J. Phys. E.* **13**, 894 (1980).

5. S. Pfenninger, J. Forrer, A. Schweiger, and Th. Weiland, *Rev. Sci. Instrum.* **59**, 752 (1988).

6. R. LoBrutto, G. W. Smithers, G. H. Reed, W. H. Orme-Johnson, S. L. Tan, and J. J. S. Leigh, Jr., *Biochem.* **25**, 5654 (1986).

7. C. L. Lin, M. K. Bowman, and J. R. Norris, *J. Magn Reson.* **65**, 369 (1985).

8. F. Momo and A. Sotgiu, *J. Phys. E.* **17**, 556 (1984).

9. G. A. Rinard, R.W. Quine, S. S. Eaton, and G. R. Eaton, *J. Magn. Reson.*, A, **105**, 137 (1993).

10. W. Froncisz and J. S. Hyde, *J. Magn. Reson.* **46**, 515 (1982), (note that equation 5 in this paper refers to unloaded Q and not loaded Q).

11. S. S. Eaton and G. R. Eaton, *J. Magn. Reson.*, A, **102**, 354 (1993).

CHAPTER FOUR

Magnetic Field and Frequency Dependence of Electron Spin Relaxation Times of the E' Center in Irradiated Vitreous Silica

4.1 Introduction

Some electron spin relaxation mechanisms depend on the applied (Zeeman) magnetic field strength, B_o, (*1, 2*) and some are dependent not on magnetic field per se but on the position in the EPR line (*3-5*). Early theory and experiment provided a picture of electron spin-lattice relaxation in ionic solids that encompassed three relaxation processes. The direct process, applicable at very low temperatures (usually below about 5 K), results in a relaxation rate ($1/T_1$) that is proportional to B_o^2 (non-Kramers species) or to B_o^4 (Kramers species) in the limit that $kT >> h\nu$ (*1*). One type of Raman process depends on B_o^2 (*6*), but the more common type does not depend on the magnetic field strength. The Orbach-Aminov process is independent of magnetic field, unless the field modifies the energy splitting between the ground state and the excited state involved in the relaxation. Relaxation via modulation of tunneling modes in glassy matrices is predicted to depend on B_o^2 (7). Localized lattice modes can contribute to electron spin-lattice relaxation (*8-11*) and may dominate for covalent lattices or molecular solids. In fluid solution, T_2 values of nitroxyl radicals have been shown to depend on the position in the spectrum (*5*). In "rigid" media, a dependence of T_m on position in the line for nitroxyl radicals has been attributed to molecular motion (*12*). Recent results from our research group demonstrate that for molecular species in frozen solution dependence of T_1 and T_m on position in the spectrum is

a general phenomenon (*13-16*). There are also special cases of apparent magnetic field dependence that involve resonant cross relaxation for two species with different g and nuclear hyperfine values (*17*).

Recently, irradiated vitreous silica (fused quartz) was proposed as a standard for time-domain EPR (*18*). Samples are now available commercially (Wilmad Glass Co., Buena, New Jersey, USA). These samples reveal many relaxation phenomena, including dependence of T_1 on position in the spectrum (*18, 19*). To understand the mechanism of electron spin relaxation in irradiated vitreous silica and to determine the utility of this type of sample at frequencies other than X-band (ca. 9 GHz), we have measured T_1 and T_2 at several microwave frequencies.

4.2 Experimental

Identical samples of vitreous silica, irradiated simultaneously to 24 Mrad with ^{60}Co γ-rays, were studied by electron spin echo (ESE) and saturation recovery (SR) at several microwave frequencies (and proportionate magnetic fields). The concentration of spins in the samples is about 6×10^{17} spins/cm^3 (*18*). Relaxation times at frequencies below 10 GHz were measured in Denver, at 19.4 GHz were measured in Milwaukee, and at 95 GHz were measured in Berlin (*20*). The lower frequency spectrometers incorporate CW, SR, and ESE in the same microwave bridge and have octave bandwidth (1-2, 2-4, and 4-8 GHz) (*21, 22*). At 9.1 GHz SR and ESE measurements were made on separate spectrometers (*23,24*). The 19.4 GHz saturation recovery spectrometer is a modern implementation of the three-arm bridge concept previously described at X-band

(*25*), incorporating a low-noise varactor-tuned Gunn oscillator (*26*) and a Gordon coupler-tuned loop-gap resonator (LGR) (*27*).

The standard samples (*18*) are 2 mm o.d. by 10 mm long cylinders. At 1.1 GHz three samples were placed in a 5.65 mm diameter copper-film LGR (described in chapter 3) to achieve a stronger signal than could be obtained with a single sample. At 3.3 and 5.9 GHz, a single sample was used in a machined copper 4-mm re-entrant LGR described in Figure 4.1 (*28,29*). At 9.2 GHz, a single sample was used in a standard TE_{102} cavity resonator. To fit the smaller LGR at 19.4 GHz, fragments of one of these cylinders was used. At 95 GHz, the fragment examined had dimensions of ca. 0.3 mm. The irregularly shaped fragments used at 19.4 and 95 GHz gave poor filling factors, so the S/N was not as good as the spectrometers could achieve with a higher filling factor, which resulted in less certain results, especially at 95 GHz. At the higher microwave frequencies the lossiness of the irradiated SiO_2 also requires the use of small samples.

The experimental parameters used in the saturation recovery measurements at each of the microwave frequencies are shown in Table 4.1. The pump power available at each microwave frequency differed due to bridge design. Data were recorded at low microwave observe power to minimize distortion of the measured T_1. The impact of spectral diffusion on the saturation recovery data was tested with measurements as a function of the length of the pump pulse. The saturation recovery time constant was found to be independent of the length of the pump pulse, within experimental uncertainty for the range of pump pulse lengths shown in Table 4.1. These results indicate that spectral diffusion is a relatively minor contribution to the relaxation process under these conditions. At S-band, when a low-power (0.2 mW) 180° pulse was used as the saturating pulse, the observed

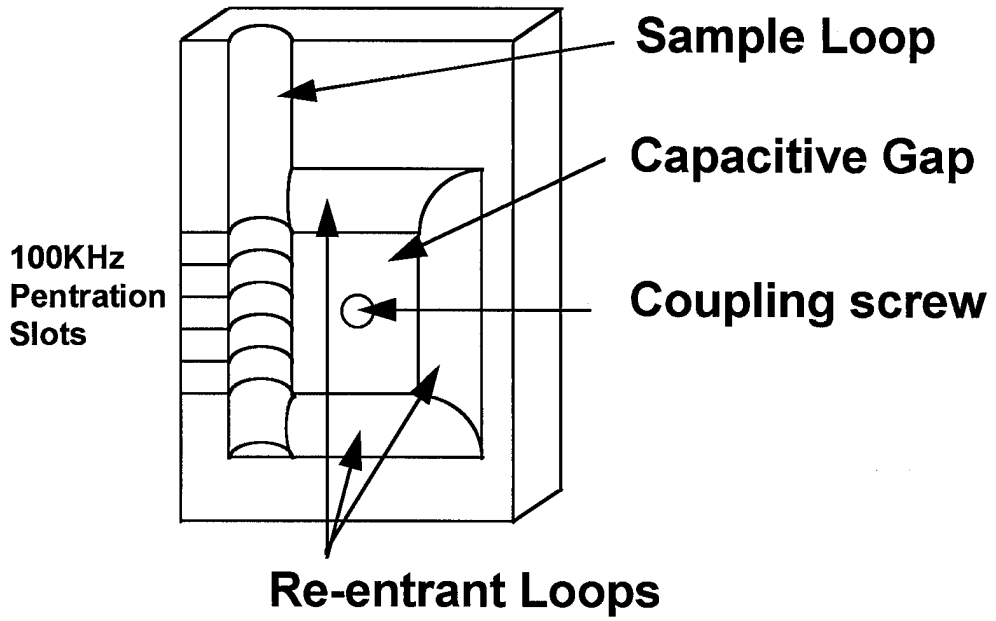

Figure 4.1. One-half view of a copper re-entrant LGR. The LGR is milled from blocks of copper metal. The S-band and C-band LGRs have sample loop diameters of 4.2 mm. The S-band LGR has a re-entrant loop diameter of 4.2 mm while the C-band LGR has a re-entrant loop diameter of 6.3 mm. The center area has been milled down to provide a capacitive gap when the two halves are placed together. Evenly spaced horizontal gaps 6 mils (1mil = 1/1000th of an inch) thick were cut into the sample area to allow for 100 KHz modulation penetration. The S-band and C-band LGRs have B_1 (mT) equal to 0.21 (watt)$^{1/2}$, and 0.16 (watt)$^{1/2}$ respectively. The LGRs are capacitively coupled, and turning the coupling screw changes the capacitance and coupling.

Table 4.1

Experimental Parameters for T_1 Measurements

microwave frequency (GHz)	observe power (nW)	pump power (mW)	pump pulse width (μs)	pulse widths (μs) checked for constant T_1
1.1	50	10	5	
2.9	70	47	5	4 to 200
5.9	26	6.3	4	4 to 255
9.1	130	480	20	1 to 400
19.4	190	100	120	10 to 400

recovery time was shorter by about 15% than when a longer high-power saturating pulse was applied, which presumably is due to spin diffusion.

T_m was determined by fitting a two-pulse echo decay to a single exponential of the form $Y(\tau) = Y(0)e^{-\frac{2\tau}{T_m}}$. Since the defect concentration in the samples was high enough to result in instantaneous diffusion, the values of T_m reported in Table 4.2 at frequencies below 10 GHz were obtained by extrapolation to infinitely small B_1 in the pulse (*18*).

4.3 Results

CW spectra of the irradiated vitreous silica samples at 1.1 and 19.4 GHz (Figure 4.2) exemplify the increasing spectral dispersion achieved with increasing microwave frequency. The values of T_1 and T_m are presented in Table 4.2. Fits of the SR data to the sum of two exponentials were tested for the S-band and X-band data. For the data sets with higher signal-to-noise (S/N) ratios, the fit to two exponentials was significantly better than for a single exponential. At X-band, the fit to two exponentials showed about 80% with a decay constant that was about 10% longer than the single exponential fit value and about 20% with a decay constant that was about 60% of the single exponential fit value. At S-band, the fit to two exponentials showed about 90% with a decay constant that was about 5% longer than the single exponential fit value and about 10% with a decay constant that was about 20% of the single exponential fit value. Since the S/N for some data sets was not high enough to obtain a statistically significant difference between one- and two-exponential fits, and since the use of two exponentials caused only a small increase in the T_1 for the major component, the values in Table 4.2 and Figure 4.3 are the "effective" T_1 values obtained by analysis of the

Table 4.2

Electron Spin Relaxation Times for E' Center

Band	Frequency (GHz)	T_1 (μs)*	T_m (μs)@
L	1.1	223-175	25
S	2.9	216-167	
	3.3		25
C	4.9	246-169	
	5.9		23
X	9.16	230 - 165	24
K	19.4	346 - 208	
W	95	480 - 240#	26#

* The range given for T_1 is from the lowest magnetic field position in the spectrum to the highest-field position measured at each microwave frequency.

@ T_m values determined by extrapolation to infinitely small B_1, except for value at 95 GHz.

The 95 GHz data are very preliminary (*38*)

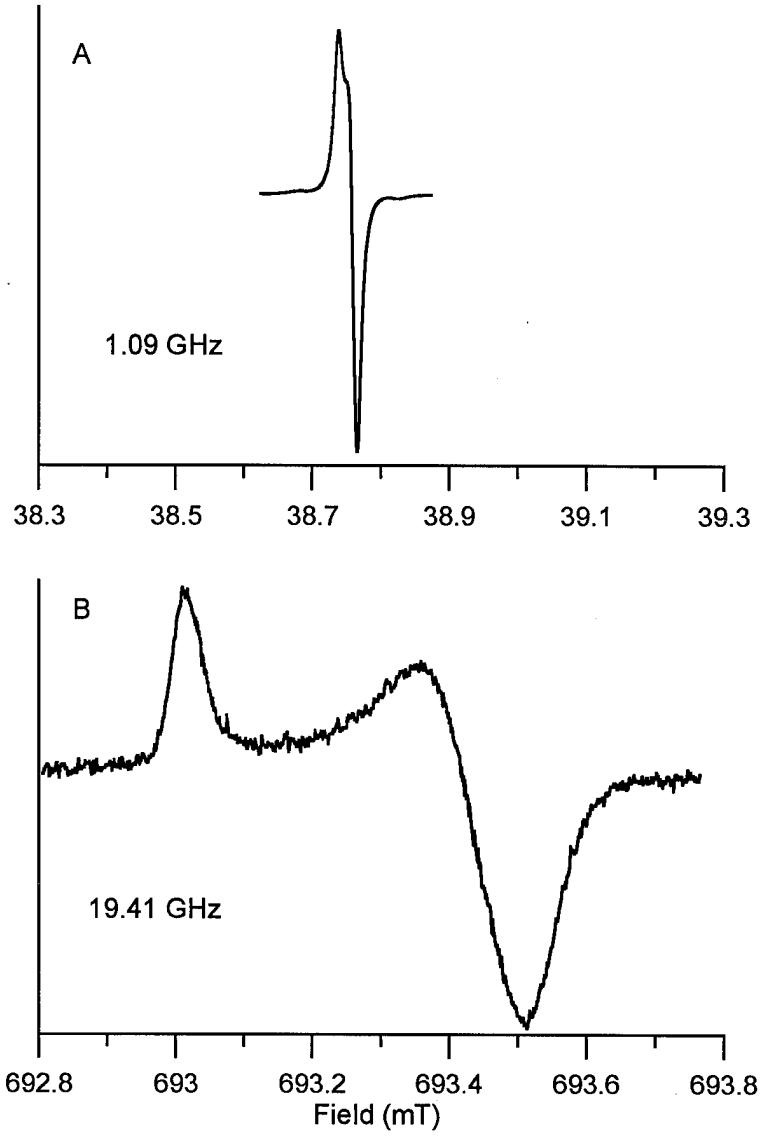

Figure 4.2. CW EPR spectra at 1.09 (A) and 19.4 (B) GHz of the irradiated vitreous silica sample used in this study demonstrate the increase in spectral dispersion with increasing microwave frequency. The spectra are approximately axial. Spectrometer settings used to record the spectra were A) 50 nW microwave power, 0.25 mT scan width, 0.05 G modulation amplitude at 100 kHz and B) 300 nW microwave power, 1.0 mT scan width, and 0.1 G modulation amplitude at 100 kHz. The 19.4 GHz spectrum was obtained by Susanne Pfenninger at the Medical College of Wisconsin.

recovery data as a single exponential. Between 1.1 and 9.1 GHz there is little change in T_1 (Figure 4.3). The values of T_1 at 19.4 GHz are systematically longer than at the lower frequency. Overall, the value of T_1 increases by about a factor of 1.5 for a factor of ca. 20 increase in microwave frequency (Figure 4.3) from L- to K-band. Preliminary data at 94 GHz indicates further increase in T_1.

At each microwave frequency T_1 is dependent upon position in the spectrum (Figure 4.3). Due to the much lower spectral dispersion at lower frequency it is more difficult to define the dependence of T_1 on g value at lower frequency than at higher frequency. This limitation is particularly severe at L band where the small spectral dispersion (Figure 4.2) limits the range of magnetic fields over which data could be measured to 0.35 G. The L-band (1.1 GHz) resonator had $Q_L = 330$ which corresponds to a bandwidth of 1.2 G. However, the limiting bandwidth in the L-band experiment was the Fourier transform of the pulse length, $1/(5\ \mu s) = 0.2$ MHz or approximately 0.07 G. Although there is greater uncertainty in the decay constants for the smaller second component (with shorter T_1) that was observed in the fit to the sum of two exponentials, the decay constant for that component appears to be independent of magnetic field (data not shown).

The value of T_m extrapolated to small B_1 appears to be independent of microwave frequency, within experimental uncertainty, over the range of frequencies investigated. In the following sections we discuss these observations in terms of a physical model of the local environment of the electron spins.

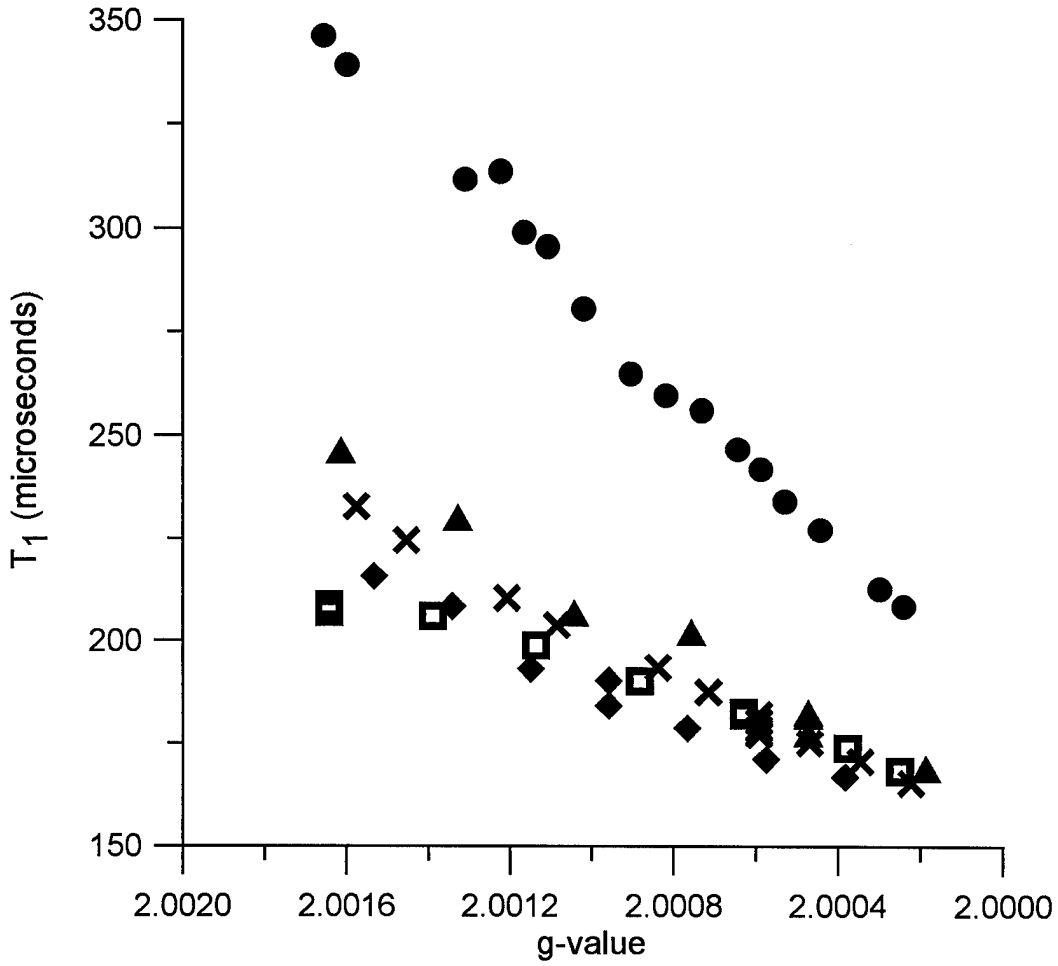

Figure 4.3. T_1 for irradiated vitreous silica as a function of g-value at five microwave frequencies (•), 19.4 GHz; (x), 9.1 GHz; (▲), 5.9 GHz; (♦), 3.3 GHz; and (□), 1.1 GHz. As shown in Figure 4.1, the same range of g-values corresponds to an increasing range in magnetic field with increasing microwave frequency.

4.4 Discussion

4.4.1 Composition of sample

Vitreous silica is largely SiO_2. There is a small amount of H present, probably in OH groups, and commonly called "water content." Irradiation with ^{60}Co γ rays creates several defect centers. The dominant defect that persists at room temperature is called the E' center. The consensus in the literature is that the E' center is an oxygen vacancy site. The unpaired electron is associated with a Si bound to three O, which thus has one "dangling" bond. The asymmetry of this bonding environment results in the g anisotropy observed in the CW EPR spectrum (Figure 4.2). Weeks and Nelson observed $g_1 = 2.0003$, $g_2 = 2.0006$, and $g_3 = 2.0018$ for the E' centers in a single crystal of quartz (*30*). They also reported line widths as narrow as 0.06 G for single-crystal samples. For convenience, since the spectroscopy on fused silica samples does not resolve three g-values, we will treat the spin system as axial, and call the observed features parallel and perpendicular.

Various amounts of Al are seen in vitreous silica samples. In the samples used for this study, a spectrum with six hyperfine lines due to interaction with Al (100% ^{27}Al, I = 5/2) was observed at high microwave powers, superimposed on the stronger E' signal. The low intensity of these lines suggests that they do not interfere with the characterization of the E' center. Due to poor S/N for these lines they were not investigated in detail. Other than the trace H and Al content, the only nuclear spins are ^{29}Si, I = 1/2, 4.7% abundance and ^{17}O, I = 5/2, 3.7×10^{-2}% abundance. At low microwave frequency the electron spin echo envelope modulation due to ^{29}Si can be observed (Figure 4.4). Buckmaster and coworkers have examined this modulation in detail (*31*).

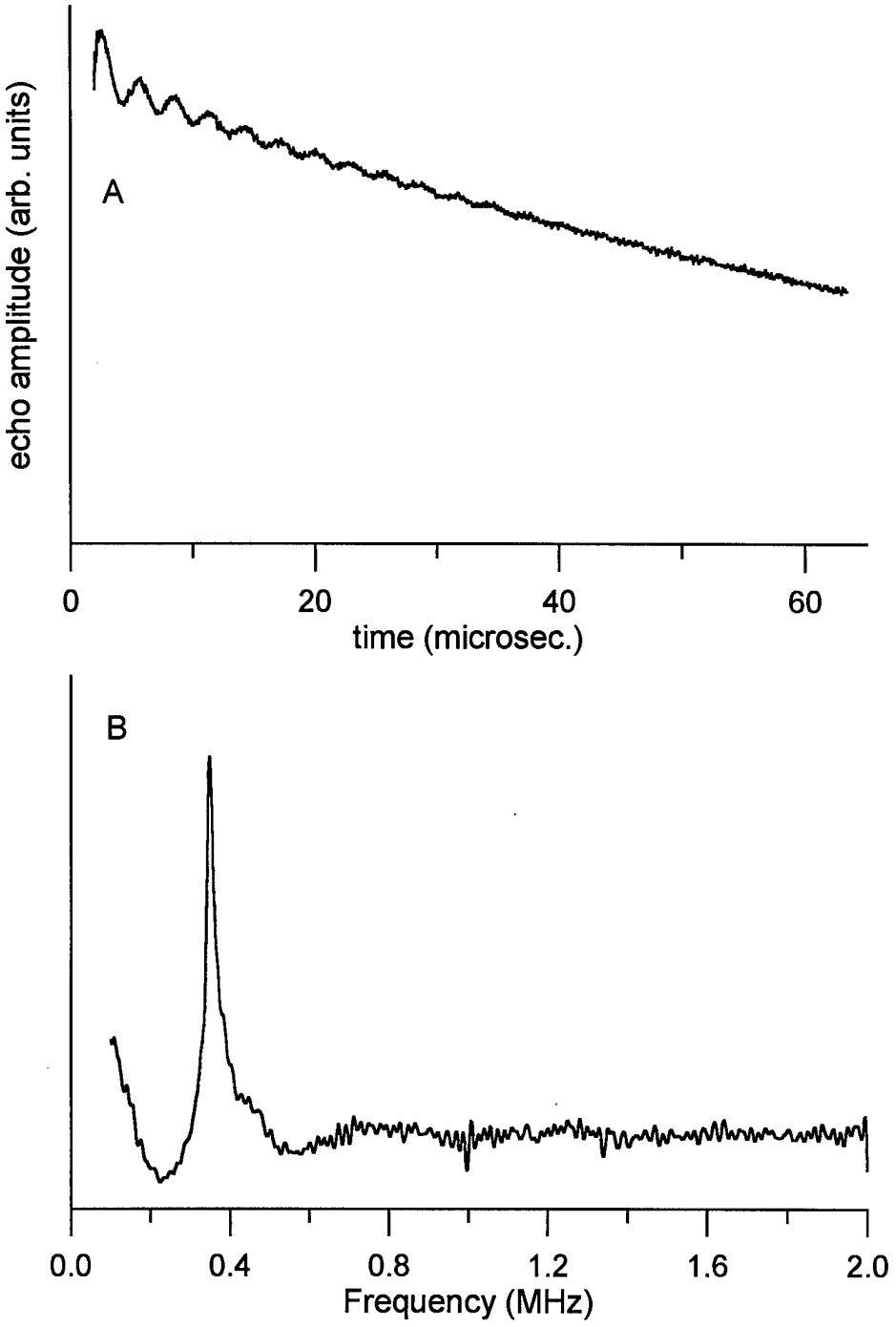

Figure 4.4. L-band (1.09 GHz) 3-pulse ESEEM data for the irradiated vitreous silica sample used in this study. Part (A) shows the time-domain response, and part (B) is the cosine Fourier transform, revealing that the dominant modulation frequency is 0.34 MHz, which is characteristic of ^{29}Si at this magnetic field.

4.4.2 Spin Lattice Relaxation

4.4.3 Local modes model

Relaxation of electron spin energy requires its conversion to thermal energy of the lattice. The familiar pictures of direct, Raman, and Orbach-Aminov processes usually are expressed in terms of lattice vibrations in solids. As has been discussed by Klemens and Castle and coworkers, there can be coupling of the electron spin energy with local vibrational modes of a solid (*8-11*). Contribution of local modes to T_1 relaxation of defects in quartz also was proposed by Scavuzzo (*39*). The temperature dependence of T_1 measured by Castle, et. al., fit to a formula for Raman processes involving local motions. In their model there exist local damped harmonic motions localized on or near the unpaired electron center with characteristic frequencies well below the Debye cutoff. This is essentially an Orbach-Aminov process involving specific local vibrational modes of the solid, although it is called a Raman process in the original papers. For the specific systems they studied they found characteristic temperatures of 14±3 K and 140 K in one case (*10*), 20±2 K and 290 K in another (*32*), and 3 K and 45 K in a third case (*9*). These energies are consistent with the presence in infrared and Raman spectra for quartz and vitreous silica of bands at 200 cm^{-1} (290 K) and lower energies (*33,34*). Castle and Feldman pointed out that anomalies in the heat capacity of vitreous silica could be quantitatively explained by low-frequency modes similar to those required to explain the electron spin lattice relaxation data. For example, a peak at 13±4 K involves 10^{-4} of the total number of lattice modes (*10*). Coupling to local modes also is important in electronic energy level relaxation (*35*).

4.4.4 Dependence of T_1 on position in spectrum

Qualitatively, it would seem that there would be more opportunities for mixing of vibrational energy with Zeeman energy in the plane perpendicular to the pseudo-threefold axis, than along it. A simple symmetry argument can be presented, treating the local modes of the SiO_3 unit by analogy with the point-group symmetry of discrete C_{3v} AB_3 species (*36*). The two A_1 type vibrations involve "axial" motions. The four vibrations of E type involve stretching and bending of bonds in the "perpendicular" direction. Each vibration changes the instantaneous structure of the molecule, and hence the mixing of orbital angular momenta in the wave functions. These changes in angular momenta mix with the spin-orbit angular momenta of the electron spin providing means for relaxation. In this symmetry argument, there are twice as many modes for perpendicular relaxation as for axial (parallel) relaxation. This model predicts that electron spin relaxation will be more facile in the perpendicular than in the axial direction (consistent with our observations). Even the factor of two is roughly consistent with our observations. We re-emphasize that this is a local vibrational mode model, not a lattice phonon model. This model does not predict a dependence on the applied magnetic field, except for the position in the line. Consistent with this model, the experimental data exhibit dependence on position in the line at all microwave frequencies, but the relaxation times are only weakly dependent on microwave frequencies.

Castle found no dependence of the rate of disappearance of a hole burned in the E' center signal on orientation of a single crystal of SiO_2 at 2.1 and 80 K (*9*). Our results were not obtained at the same temperature. However, Castle and coworkers found orientation dependence at some temperatures and centers and not

others. They attributed at least part of their observations to relative contributions of cross relaxation to the measured recovery times.

4.4.5 Dependence of T_1 on microwave frequency

There is no apparent dependence of T_1 on microwave frequency up to X-band. Even though the data is less precise at 94 GHz, there is a definite trend to longer relaxation times at 19 and 94 GHz.

The spin concentration in the irradiated samples is high enough that one might expect some spin diffusion and faster relaxation via local clusters of spins. Local clusters might also be the cause of the faster T_1 component that was detected in the fit of selected data to the sum of two exponentials. Increasing spectral dispersion at higher microwave frequencies would decrease the effective concentration of spins. Some refinement of this idea is needed to account for the bandwidth and B_1 used in each experiment. The small increase in T_1 with increasing microwave frequency is consistent with this picture. However, the lack of dependence of the effective T_1 on the length of the pump pulse suggests that spin diffusion is not dominant.

The weak dependence of T_1 on microwave frequency can be understood in the local modes model. In light of the results obtained by Castle, et. al., (*8-11*) and discussed above, we point out that the microwave quantum at 94 GHz is ca. 3 cm^{-1}, or ca. 4.3 K. Thus, the vibrational modes inferred from temperature-dependence studies are of the order of the EPR quantum at higher frequencies, and the assumption that the energies are much larger than the EPR quantum is no longer well-satisfied for these modes. Hence, the relaxation becomes slower.

4.4.6 Phase Memory Relaxation Time

If there were no nuclear spins coupled to the electron spins, the phase memory time, T_m, would be determined by the interactions among the electron spins. Following (*37*), T_2 for the electron spins is of the order of

$$T_2 = \frac{hr^3}{2\pi\mu^2}. \qquad [1]$$

where h = Planck's constant, r = distance between unpaired spins, and μ = electron magnetic moment. Using the spin concentration of ca. $6x10^{17}$ spins per cm^3 measured by ESE (*18*),

$$T_2 = \frac{\left(6.626x10^{-27}\,\text{erg sec}\right)\left(118x10^{-8}\,\text{cm}\right)^3}{2(3.1416)\left(9.28x10^{-21}\,\text{erg G}^{-1}\right)^2}$$

$$T_2 = 2x10^{-5}\ \text{sec}\ (= 20\ \mu\text{s}) \qquad [2]$$

This approximate calculation is in close agreement with the measured value of ca. 25 μs. The low-frequency ESEEM data show that the electron spins are coupled to the ^{29}Si nuclear spins. However, for any reasonable structural model, the electron-nuclear coupling contribution to T_2 calculated by a formula analogous to eq [1] will be less than the electron-electron coupling, because the abundance of ^{29}Si is so low. These considerations suggest that the T_m measured at low microwave B_1 approximates a true T_2 for these electron spins.

References

1. K. J. Standley and R. A. Vaughan, "Electron Spin Relaxation Phenomena in Solids", Plenum Press, New York, 1969.

2. C. P. Poole, Jr., and H. A. Farach, "Relaxation in Magnetic Resonance", Academic Press, New York, 1971.

3. M. K. Bowman and L. Kevan, Electron Spin-Lattice Relaxation in Nonionic Solids, in "Time Domain Electron Spin Resonance", L. Kevan and R. N. Schwartz, eds., Wiley, New York, 1979.

4. I. M. Brown, Electron Spin-Echo Studies of Relaxation Processes in Molecular Solids, in "Time Domain Electron Spin Resonance", L. Kevan and R. N. Schwartz, eds., Wiley, New York, 1979.

5. J. Gorchester, G. L. Millhausser, and J. H. Freed, Two-Dimensional Electron Spin Resonance, in "Modern Pulsed and Continuous-Wave Electron Spin Resonance", L. Kevan and M. K. Bowman, eds., Wiley, New York, 1990.

6. R. L. Marchand and H. J. Stapleton, *Phys. Rev. B.* **9**, 14 (1974).

7. M. K. Bowman and L. Kevan, *J. Phys. Chem.* **81**, 456 (1977).

8. P. G. Klemens, *Phys. Rev.* **125**, 1795 (1962). See correction in *Phys. Rev.* **138 A**, 1217 (1965).

9. J. G. Castle, Jr., D. W. Feldman, P. G. Klemens, and R. A. Weeks, *Phys. Rev.* **130**, 577 (1963).

10. J. G. Castle, Jr. and D. W. Feldman, *J. Applied Phys.* **36**, 124 (1965).

11. D. W. Feldman, J. G. Castle, Jr., and J. Murphy, *Phys. Rev.* **138 A**, 1208 (1965).

12. S. A. Dzuba, Yu. D. Tsvetkov, and A. G. Maryasov, *Chem. Phys. Lett.* **188**, 217 (1992).

13. J.-L. Du, K. M. More, S. S. Eaton and G. R. Eaton, *Israel J. Chem.* **32**, 351 (1992).

14. R. Konda, J.-L. Du, S. S. Eaton, and G. R. Eaton, *Appl. Magn. Reson.* in press.

15. J.-L. Du, K. M. More, G. R. Eaton, and S. S. Eaton, 15th International EPR Symposium, Denver, 1992, abstract 116.

16. J.-L. Du, G. R. Eaton, and S. S. Eaton, 16th International EPR Symposium, Denver, 1993, abstract 99.

17. G. H. Larson and C. D. Jeffries, *Phys. Rev.* **145**, 311 (1966).

18. S. S. Eaton and G. R. Eaton, *J. Magn. Reson. A* **102**, 354 (1993). Note that in this paper the magnetic field range in Figure 1 is 3263 to 3273 G, not 2869 to 2879 G as published.

19. P. Ludowise, S. S. Eaton and G. R. Eaton, *J. Magn. Reson.* **93**, 410 (1991).

20. M. Rohrer, T. F. Prisner, and K. Möbius, Workshop on High-Frequency EPR and Electron Spin Echo Spectroscopy, Amsterdam, April, 1993.

21. B. T. Ghim, G. A. Rinard, R. W. Quine, and G. R. Eaton, 16th International EPR Symposium, Denver, 1993, abstract 159.

22. R. W. Quine, B. T. Ghim, G. A. Rinard, S. S. Eaton, and G. R. Eaton, to be published.

23. R. W. Quine, G. R. Eaton, and S. S. Eaton, *Rev. Sci. Instrum.* **58**, 1709 (1987).

24. R. W. Quine, G. R. Eaton, and S. S. Eaton, *Rev. Sci. Instrum.* **63**, 4251 (1992).

25. P. W. Percival and J. S. Hyde, *Rev. Sci. Instrum.* **46**, 1522 (1975).

26. P. Lesniewski and J. S. Hyde, *Rev. Sci. Instrum.* **61**, 2248 (1990).

27. T. Oles, J. S. Hyde, and W. Froncisz, *Rev. Sci. Instrum.* **60**, 389 (1989).

28. B. T. Ghim, G. A. Rinard, R. W. Quine, and G. R. Eaton, 16th International EPR Symposium, 35th Rocky Mountain Conference, Denver, Colorado, Abstract 159 (1993).

29. M. Giordano, F. Momo, A. Sotgiu, *J. Phys. E: Sci. Instrum.* **16**, 774 (1983).

30. R. A. Weeks and C. M. Nelson, *J. Appl. Phys.* **31**, 1555 (1960).

31. V. V. Kurchev, H. A. Buckmaster, and L. Tykarski, *J. Chem. Phys.* **101**, 10338 (1994).

32. J. G. Castle and D. W. Feldman, *Phys. Rev.* **A137**, 671 (1965).

33. D. W. James and M. J. Nolan, *Prog. Inorg. Chem.* **9**, 195 (1968).

34. A. Wang, J. Han, L. Guo, J. Yu, and P. Zeng, *Appl. Spect.* **8**, 959 (1994).

35. R. Englman, "Non-Radiative Decay of Ions and Molecules in Solids", North-Holland, Amsterdam, 1979.

36. F. A. Cotton, Chemical Applications of Group Theory, 2nd ed., Wiley, New York, 1971, page 320ff.

37. N. Bloembergen, E. M. Purcell, and R. V. Pound, *Phys. Rev.* **73**, 679 (1948).

38. Thomas F. Prisner and Klaus Möbius, personnal communication.

39. R. J. Scavuzzo, "A Study of the Spin-Lattice Relaxation Properties of a Paramagnetic Defect Center in α-Quartz", Ph.D. Dissertation, University of Pittsburgh, 1968.

CHAPTER FIVE

Multi-Frequency CW and Time-Domain EPR of Irradiated L-Alanine

5.1 Introduction

Dosimetry of ionizing radiation is of medical and commercial importance, and increasingly is a matter of concern in monitoring international trade. Hence, the adoption of scientifically-based, reliable, and verifiable measurement of radiation dose is becoming important. Quantitative measurement of the EPR signal of the radical generated by radiation of crystalline L-alanine is emerging as a method of choice for such dosimetry (*1, 2, 3*). The X-band (ca. 9 GHz) CW EPR spectrum of irradiated alanine is familiar to the users of alanine dosimetry. However, there are questions concerning the assignments of the peaks in this deceptively simple spectrum including the importance of spin-flip transition satellite lines and proposed explanations for the line shape changes when the spectrum is power-saturated (*4*). These issues have stimulated efforts to understand the EPR of irradiated alanine well enough to provide confident underpinning for international legal acceptance of alanine dosimetry. CW spectra also have been reported at 35 GHz (*4*). Time domain studies include electron spin echo (ESE) and saturation recovery (SR) at X-band (*5-7*). Due to rapid spectral diffusion in the irradiated alanine samples at room temperature, estimates of relaxation times are strongly dependent upon the measurement technique (*7*). In this chapter, we present multifrequency EPR studies to provide an enhanced picture of the alanine radical spin system.

5.2 Experimental

Commercial crystalline L-alanine was irradiated at room temperature with ^{60}Co γ–rays in a large commercial sterilization facility (Cobe Laboratories, Lakewood, Colorado). The dose for the two samples used in these experiments was 73 or 100 kGy, determined by radiochromic film, traceable to NIST. The irradiated samples were placed in standard 4 mm o.d. quartz sample tubes.

EPR measurements at 19.4 GHz were made in Milwaukee on a modern implementation of the three-arm bridge concept previously described (*8*). X-band CW measurements were done on a Bruker ESP 380E. X-band ESE and SR data were obtained on locally-constructed spectrometers (*9,10*). Spectra at lower frequencies were obtained on locally-constructed spectrometers in the style of the X-band systems, except that CW, ESE, and SR capabilities are included in a single bridge. The bridges cover 1 - 2, 2 - 4, and 4 - 8 GHz and use copper single-loop re-entrant loop gap resonators described in chapter 4 (*11*). T_m measurements were made with a 90-τ_1-180-τ_1-echo sequence. T_1 measurements were: inversion recovery (IR) with a 180-τ_1-90-τ_2-180-τ_2 echo sequence, stimulated echo (SE) with a 90-τ_1-90-τ_2-90-τ_1 echo sequence, and long-pulse saturation recovery (SR). The values of T_1 obtained by SR increased with increasing length of the pump pulse up to about 60 μs, so data was collected with pump pulse lengths greater than 100 μs. The observe power in the SR experiments was reduced until no further change in T_1 was observed. The instrument parameters for the SR experiments are summarized in Table 5.1.

Table 5.1

Experimental Parameters for SR Measurements

Band	Frequency	Pump Pulse (μs)	Pump Power (mW)	Observe Power (μW)[a]	Pulse Widths Checked for constant T_1 (μs)
L	1.8	300	40	5	1 to 500
S	3.2	200	50	0.7	1 to 500
C	4.9	100	40	1	1 to 300
X	9.1	800	480	22	4 to 800
K	19.4	120	100	0.3	2 to 200

[a] A cavity was used at X-band and loop gap resonators were used at the other frequencies.

5.3 Results and Discussion

5.3.1 CW spectra

In the X-band CW spectrum of irradiated L-alanine the relative intensities of the lines marked A and B in Figure 5.1 are substantially greater at high microwave power than at low microwave power. These are the lines that have been assigned to "spin-flip" transitions (*4, 12*). Similar pairs of satellite lines occur for each of the major lines in the spectrum. A plot of peak-to-peak signal intensity as a function of microwave B_1 at X-band (Figure 5.2) demonstrates that 0.416 mW ($B_1 = 2.4x10^{-3}$ mT) does not saturate the spectrum significantly and that 105 mW results in severe power saturation.

The CW spectra of irradiated L-alanine at 1.8, 3.2, and 4.9 GHz are shown in Figure 5.3. The spectra are strikingly similar to the unsaturated X-band spectrum (Figure 5.1, 0.416 mW) which confirms that at these microwave frequencies the spectral extent is determined primarily by electron-nuclear hyperfine splitting with little contribution from g-anisotropy. When the microwave power at L-band is increased from 50 μW to 10 mW, the changes in the CW spectra are much smaller (Figure 5.3) than were observed at X-band (Figure 5.1). A power saturation curve for the allowed transitions in the center of the L-alanine spectrum at 1.8 GHz (Figure 5.2) indicates that powers below about 0.10 mW ($B_1 = 3x10^{-3}$ mT) are non-saturating and that 10 mW results in substantial saturation. The small line shape changes between the unsaturated and saturated spectra are consistent with the broadening expected as a signal is saturated.

Both the intensities of the spin-flip lines and the separation between a spin-flip line and the central line are frequency dependent (*12*). First, the intensities of

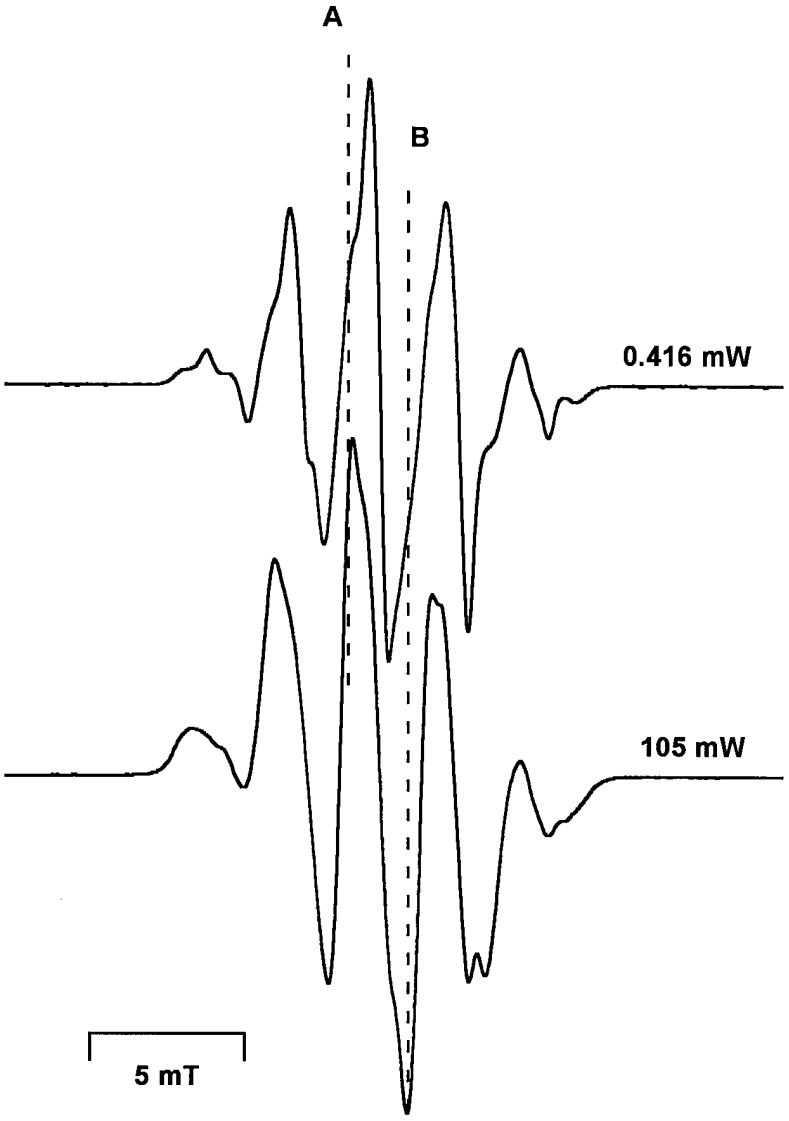

Figure 5.1. X-band CW spectra of irradiated L-alanine obtained with 0.01 mT modulation amplitude at 100 kHz, 0.0819 s time constant, and 84 s. scan time: unsaturated spectrum obtained with 0.416 mW microwave power (upper trace) and saturated spectrum obtained with 105 mW microwave power (lower trace). The dashed lines marked A and B denote the positions of two of the satellite lines that are assigned as spin-flip transitions.

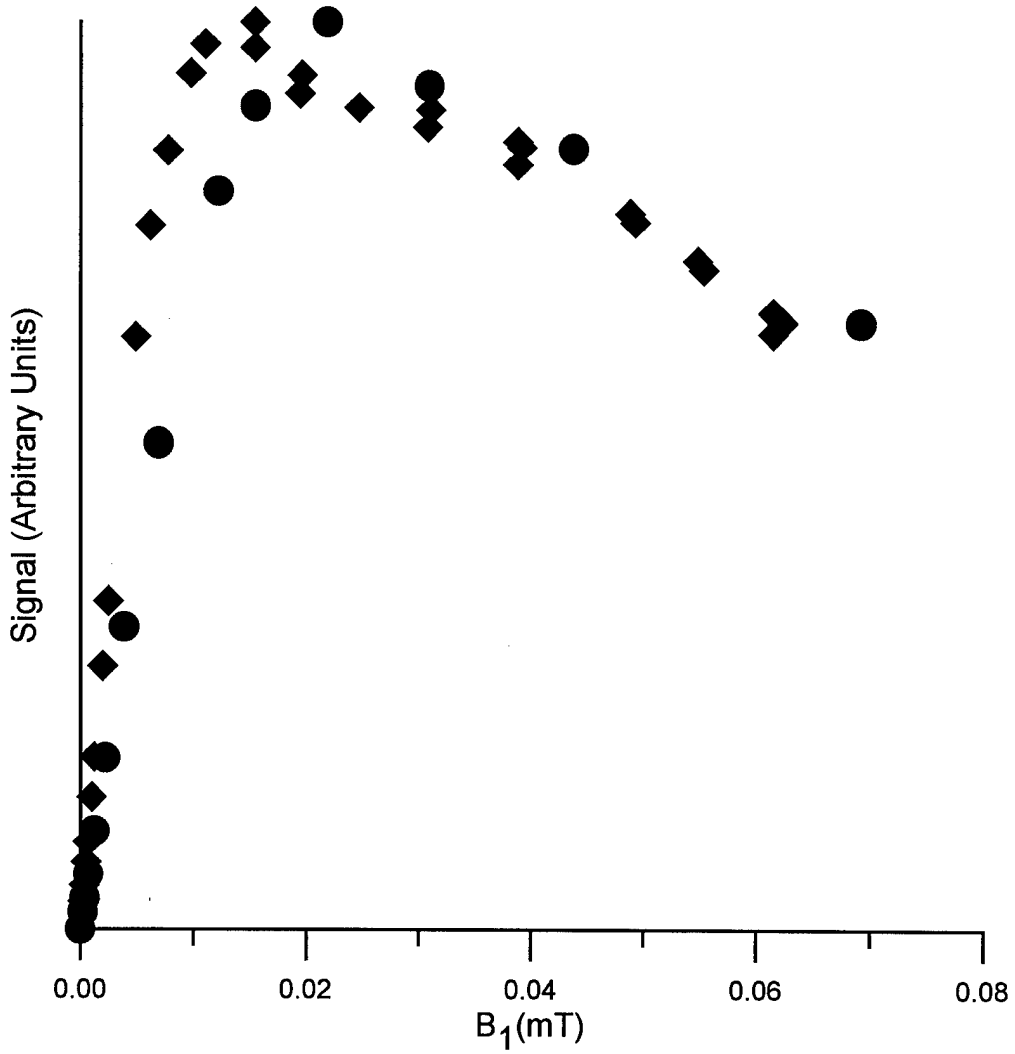

Figure 5.2. Power saturation curves for the allowed transitions at the middle of the central peak in the spectrum at 1.8 GHz (•) and 9.4 GHz (♦) for irradiated L-alanine signal. The peak-to-peak amplitude of the signal in arbitrary units, corrected to constant gain, is plotted as a function of microwave B_1. B_1 (mT) = $a\sqrt{P}$ with P in watts, a = 0.30 at L-band and 0.12 at X-band.

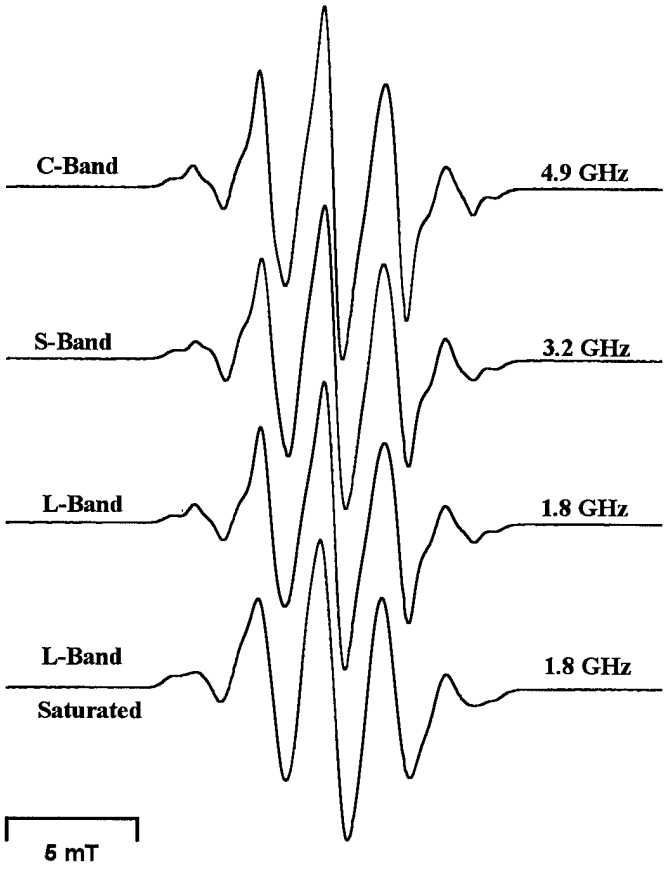

Figure 5.3. CW spectra of irradiated L-alanine at three microwave frequencies. Spectra were taken with 0.05 mT modulation amplitude at 100 kHz, 0.128 s time constant, and 120 s scan time . The microwave powers used for data collection were: C-band, 3.5μW; S-band, 70μW; L-band, 50μW; and L-band saturated spectrum, 10mW.

the transitions are inversely proportional to frequency squared so these transitions make increasingly intense contributions to the spectra at lower frequency. For example, decreasing the frequency from 9.4 to 1.8 GHz increases the relative intensity of the spin-flip transitions by about a factor of 27. Second, the separation between the central line and the spin-flip lines is linearly proportional to the external magnetic field, B_0 (*12*). At X-band (9.5 GHz, B_0=340 mT) that separation is 0.51 mT. The linear dependence on field predicts the following separations at lower frequencies: 0.26 mT at 4.9 GHz, 0.17 mT at 3.2 GHz, and 0.10 mT at 1.8 GHz. These values are small relative to the line widths of the irradiated alanine spectra. The more conspicuous contributions of the spin-flip lines to the CW spectra at X-band than at either higher or lower frequencies can therefore be rationalized. At higher frequencies, the decreased intensity of the spin-flip transitions makes their contributions smaller (*4*). At lower frequencies, the smaller splittings cause the spin-flip transitions to be unresolved although the underlying contributions from these transitions increase.

The power saturation curves at L-band and X-band (Figure 5.2) show that a higher B_1 is required to saturate the signal at L-band than at X-band. This trend is consistent with the shorter relaxation times measured by time-domain techniques at lower frequencies as discussed in the following paragraphs. In addition, the forbidden transitions have lower transition probabilities so higher power is required to cause saturation. At lower frequency, the increased relative intensity of the spin-flip transitions and the higher B_1 required to saturate those transitions contributes to less saturation at the same power for the composite spectrum.

Table 5.2

Frequency Dependence of Phase Memory Relaxation Time

Band	Frequency	Radiation Dosage (kGy)	T_m [a] (ns)
S	3.2	100	87 ± 1
C	4.9	100	93 ± 3
C	4.9	73	101 ±1
X	9.4	100	135 ± 4

[a] Uncertainty in T_m is the 95% confidence level calculated from the linear regression.

5.3.2 Phase Memory Times

The phase memory times, T_m, for the irradiated alanine signal were measured by two-pulse electron spin echo at 3.2, 4.9, and 9.5 GHz (Table 5.2). Values of T_m were measured as a function of microwave B_1. Under conditions where a 30 ns pulse corresponds to a 90° turning angle and excites a bandwidth of 0.3 mT, varying B_1 by a factor of 4.5 caused about a 10% change in T_m, which indicates that instantaneous diffusion makes a relatively small contribution in these samples. Values of T_m were measured as a function of position in the spectrum, but little variation was observed. The echo envelope modulation is deeper at lower frequency, which may be a source of systematic error for these short values of T_m that is not reflected in the uncertainty calculated from the regression analysis (Table 5.2). Reliable data were not obtained at 1.8 GHz because of a combination of short T_m, deep echo envelope modulation, and longer cavity ring-down for the same value of Q than at higher frequency. The phase memory times, T_m, (Table 5.2) increased with increasing microwave frequency. One possible explanation is that the decreased relative intensities of the spin-flip lines at higher frequency contributes to the increase in T_m. Because of the deeper modulation at lower frequencies a fit to the sum of two contributions did not seem warranted. T_m for irradiated L-alanine has previously been shown to increase with decreasing radiation dose and approaches a limiting value of ~200 ns at low dose (*5, 6*). The X-band values obtained in this study for 100 kGy dose are consistent with previous results (*5, 6*). Values of T_2 about 700 ns were obtained by a Carr-Purcell-Meiboom-Gill pulse sequence (*5, 7*). The longer value of T_2 than of T_m at low dose suggests that spectral diffusion makes a significant contribution to the T_m values.

5.3.3 Spin-Lattice Relaxation Times

At each microwave frequency, the recovery curves for the long-pump SR experiments indicated the presence of at least two time constants, which is consistent with previous X-band experiments (*6, 7*). Data were obtained as a function of position in the spectrum, but little variation was observed. Data were fitted to the sum of two exponentials although the possibility of a larger number of contributions cannot be ruled out. The time constants for those two components are identified in Table 5.3 and Figure 5.4 as the short and long T_1. The weightings of the short and long components (extrapolated to time = 0) were 5:1 at 1.8 GHz, 1.5:1 at 3.2 and 4.9 GHz, 1:1 at 9.5 GHz, and 0.5:1 at 19.4 GHz. Thus, the contribution from the component with the shorter T_1 (faster relaxing component) decreases with increasing microwave frequency.

An X-band pulsed ELDOR study of irradiated malonic acid found that T_1 for the spin-flip transitions was about a factor of 7 longer than for the allowed transitions (*14*). By analogy, a longer T_1 for the spin-flip transitions than for the allowed transitions is probable for irradiated alanine, but further experiments are required to test possible assignments. In addition to the changing weightings of the two components, the values of T_1 for both components increased with increasing microwave frequency (Figure 5.4, Table 5.3). This trend is similar to what was observed previously for T_1 of the E' defect in irradiated amorphous SiO_2 (*15*).

Estimates of T_1 also were obtained by inversion recovery (IR) and 3-pulse spin echo (SE) (Table 5.3). The pulse width and microwave power were adjusted to excite a 0.3 mT bandwidth. The microwave power was the same for each of the three pulses. The data also indicated the presence of at least two exponential

Table 5.3

Values of T_1 Determined by Three Techniques

Frequency (GHz)	Radiation Dose (kGy)	Method	T_1[a] Long (μs)	T_1[a] Short (μs)	Time Window(μs)
1.8	100	SR[b]	22	6	200
3.2	100	SR	23	6	206
4.9	100	SR	29	6	500
4.9	73	SR	30	7	206
9.1	73	SR	48	7	500
19.4	73	SR	73	19	1000
3.1	100	IR[c]	8.3	1.1	64
4.6	100	IR	7.7	0.9	32
4.6	73	IR	8.1	0.8	32
9.4	100	IR	7.2	1.1	30
3.1	100	SE[d]	0.57	0.11	6
4.6	100	SE	1.7	0.27	6
4.6	73	SE	2.2	0.36	10
9.4	100	SE	1.3	0.33	5

[a] Long and short refer to the time constants for the two components in the fit of the data to the sum of two exponentials, [b] long pulse saturation recovery, [c]inversion recovery, [d] electron spin echo.

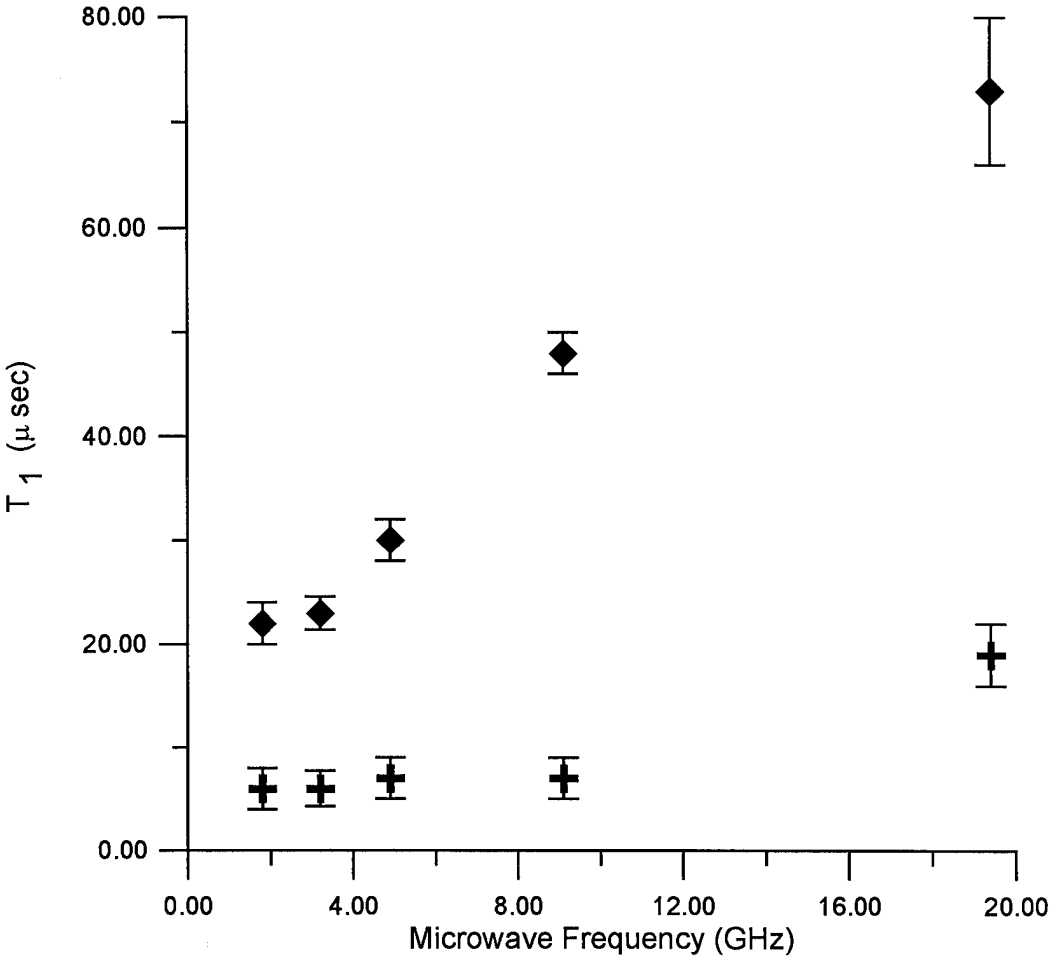

Figure 5.4. Frequency dependence of T_1 obtained by fitting the SR data to the sum of two exponentials: (+) faster relaxing component, (♦) slower relaxing component. The relative weightings of the two components also change with microwave frequency (see text).

components, although the time constants were substantially shorter than in the SR experiment. In the long-pump SR experiment, the faster the spectral diffusion, then the wider the hole that is burned in the spectrum. By increasing the length of the pump pulse until no further increase in time constant for the recovery curve is observed, one aims to measure T_1 with minimum interference from spectral diffusion. In contrast, in the IR and SE experiments, spectral diffusion can be a major contribution to the apparent decay. The much shorter estimates of T_1 obtained by the latter two methods is consistent with rapid spectral diffusion in the L-alanine sample at room temperature, and agree with literature results at X-band (*5, 7, 16, 17*). To account for the multiple processes that may contribute to the recovery curves, the experiments described in chapters six and seven are required.

5.4 Conclusions

The CW spectra as a function of microwave frequency are consistent with assignment of the satellite lines in the X-band spectra to spin-flip lines. The spin-lattice relaxation time and phase memory time increase with increasing microwave frequency. The shorter relaxation times obtained by inversion recovery or spin echo than by long-pulse saturation recovery indicate fast spectral diffusion.

REFERENCES

1. D. F. Regulla and U. Deffner, *Int. J. Appl. Radiat. Isot.* **33**, 1101 (1982) and references cited therein.

2. *Applied Radiation and Isotopes* **40** (10-12) (1989). Papers from the 2nd International Symposium on ESR Dosimetry and Applications, Munich, October, 1988.

3. *Applied Radiation and Isotopes* **44** (1-2) (1993). Papers from the 3rd International Symposium on ESR Dosimetry and Applications, Gaithersburg, MD, October, 1991.

4. J. M. Arber, P. H. G. Sharpe, H. A. Joly, J. R. Morton, and K. F. Preston, *Appl. Radiat. Isot.* **42**, 665 (1991).

5. P. Höfer, K. Holczer, and D. Schmalbein, *Appl. Radiat. Isot.* **40**, 1233 (1989).

6. K. Nakagawa, S. S. Eaton, and G. R. Eaton, *Appl. Radiat. Isot.* **44**, 73 (1993).

7. M. Brustolon and U. Segre, *Appl. Magn. Reson.* 7, 405 (1994).

8. P. W. Percival and J. S. Hyde, *Rev. Sci. Instrum.* **46**, 1522 (1975).

9. R. W. Quine, G. R. Eaton, and S. S. Eaton, *Rev. Sci. Instrum.* **53**, 1709 (1987).

10. R. W. Quine, G. R. Eaton, and S. S. Eaton, *Rev. Sci. Instrum.* **63**, 4251 (1992).

11. B. T. Ghim, G. A. Rinard, R. W. Quine, and G. R. Eaton, 16th International EPR Symposium, 35th Rocky Mountain Conference, Denver, Colorado, Abstract 159 (1993).

12. G. T. Trammell, H. Zeldes, and R. Livingston, *Phys. Rev.* **110**, 630 (1958).

13. S. S. Eaton and G. R. Eaton, *J. Magn. Reson.* **A 102**, 354 (1993).

14. M. Nechtschein and J. S. Hyde, *Phys. Rev. Lett.* **24**, 672 (1970).

15. B. T. Ghim, S. S. Eaton, G. R. Eaton, R. W. Quine, G. A. Rinard, and S. Pfenninger, *J. Magn. Reson.* A **115**, 230 (1995)

16. I. Miyagawa and K. Itoh, *J. Chem. Phys.* **36**, 2157 (1962).

17. M. Brustolon, T. Cassol, L. Micheletti, and U. Segre, *Mol. Phys.* **57**, 1005 (1986).

CHAPTER SIX

S-Band Pulsed Stepped-Field Electron-Electron Double Resonance Spectroscopy

6.1 Introduction

Electron-electron double resonance (ELDOR) spectroscopy is a technique to measure energy transfer between EPR transitions (*1-4*). In field-swept CW ELDOR, two microwave frequencies are applied, a pump and an observe frequency, while the magnetic field is swept (*2*). Less common ELDOR techniques also have been reported. (i) In time-resolved ELDOR, two different microwave frequencies are used as in CW-ELDOR, but the pump frequency is pulsed (*5*). (ii) Pulsed FT ELDOR is a variant of the NMR two-dimensional correlation spectroscopy (COSY) method. Three $\pi/2$ microwave pulses are applied. The FID after the third microwave pulse is Fourier transformed and plotted as a function of the time between the first and second microwave pulses (*6*). (iii) Stepped-field ELDOR [STELDOR; we adopt the nomenclature of Freed (*7*)], uses one microwave frequency, and two different magnetic fields to pump and observe the spin transfer (*7-10*). There are few reports of pulsed magnetic field EPR experiments (*7-22*). In this chapter, we describe a resonator and magnetic-field coil system that can be implemented as an inexpensive accessory to an EPR spectrometer, yielding up to 2.6 mT (10,000 G = 1 T) field jumps in its present configuration.

The central goal of this instrument development was the capability to measure the rate of transfer of spectral information from one field/frequency position in the spectrum to another field/frequency position in the spectrum. The

relaxation processes involved are variously called spin diffusion, spectral diffusion, and cross-relaxation in the literature. Consistent with the general resonance equation ($h\nu = g\beta B$), two or more regions of the spectrum can be measured either by varying ν or B. To measure rates of communication between the regions, one needs pulsed, time-domain measurements. There is extensive literature relating to the use of pulsed magnetic fields in NMR, which is not cited here. Many of the EPR experiments were stimulated by analogous experiments originally done in NMR (*23,24*). This chapter describes measurements made after a pulsed change in magnetic field and the next chapter (chapter 7) describes experiments in which microwave pulses at two frequencies are used. The results of these time-domain perturbations are interpreted in terms of the fundamental contributions to electron spin relaxation in chapter 8.

6.2 Experimental

A pulsed stepped-field was applied in conjunction with the first pulse of a 180-τ_1-90-τ_2-180-τ_2-observe inversion-recovery spin-echo sequence. The timing of the various pulses is shown in Figure 6.1. At the start of the experiment, the field was stepped rapidly from B_0 to $B_0+\Delta B$. The first 180° microwave pulse was applied to invert the magnetization at field $B_0+\Delta B$. The field was then rapidly stepped back to B_0 and a two-pulse 90-τ_2-180 spin-echo sequence was applied to produce a spin echo. In this experiment τ_1 is varied, while τ_2 is fixed. The spin echo as a function of τ_1 was detected with a double balanced mixer and averaged in a boxcar integrator. To achieve the best signal to noise ratio, the boxcar aperture was set to integrate the peak of the echo.

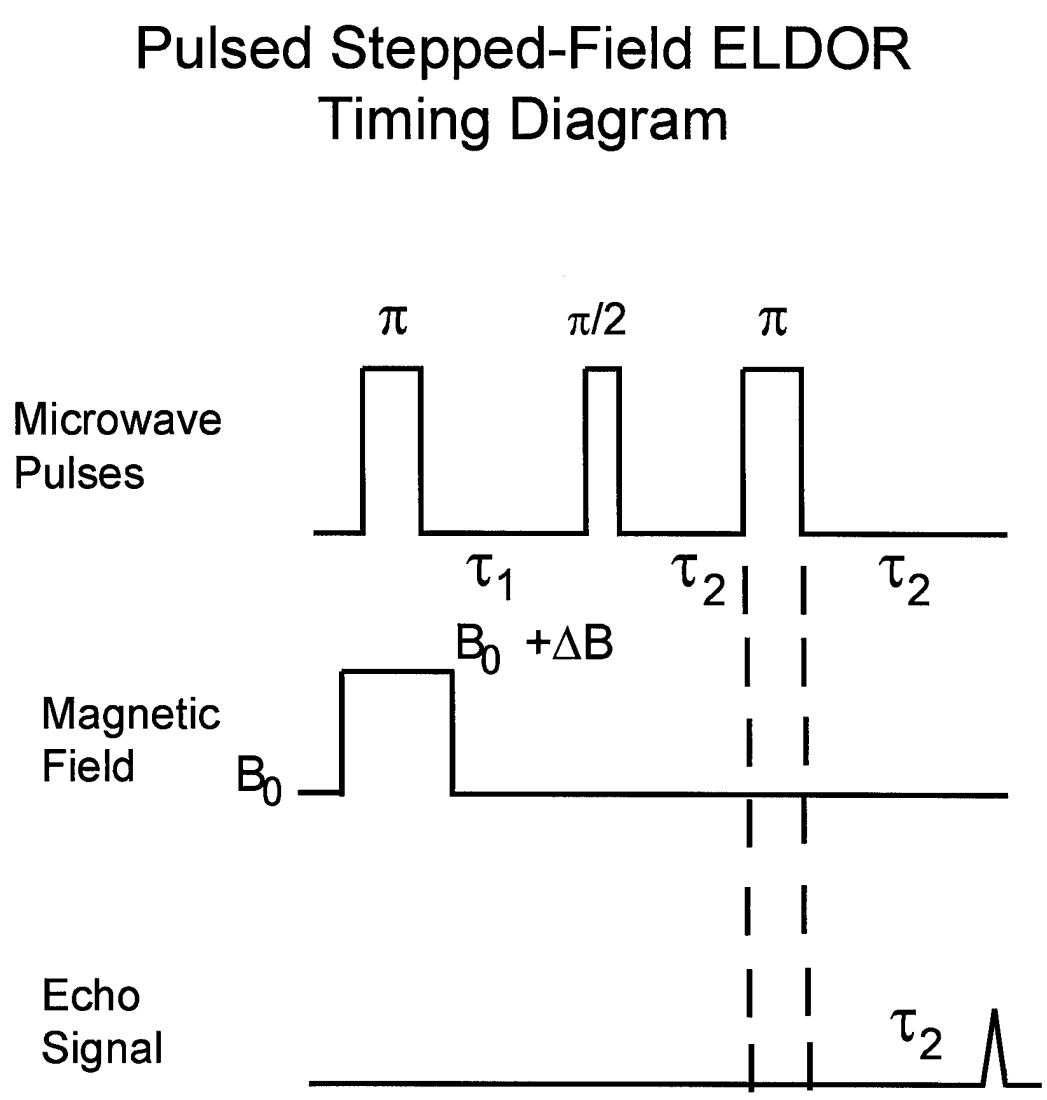

Figure 6.1. Pulsed STELDOR timing diagram.

The pulsed S-band spectrometer combines SR and ESE capabilities implemented previously at X-band (*25,26*). Figure 6.2 shows a block diagram of the hardware for the pulsed STELDOR experiment. The pulsed stepped-field was generated by passing up to 70 A of current through two single-turn 1 cm square coils located close to the copper film resonator (resonator described in chapter three). The single-turn coils were selected to minimize inductance. The current pulse was controlled using a Behlke HTS-21-14 high voltage switch. Figure 6.3 is the switch-driver circuit diagram. A snubber circuit (resistor R6 in conjunction with capacitor C2) eliminated most of the switching transient when the current was shut off. The values for R6 and C2 were determined by simulating the circuit parameters on MICRO-CAP III (Spectrum Software, Sunnyvale, CA), an electronic circuit analysis computer program. The switching transients at switchoff increased as more power was switched by the system, and the spin-echo was attenuated severely when the two-pulse sequence was started before the field was fully stable at B_0. The system as currently configured allowed a maximum pulsed stepped-field of approximately 2.6 mT. At full current (70 A), data collection could commence 400 ns after the stepped-field was switched off. The voltage signal and integrated signal resulting from a pulsed stepped-field measured with a 3 mm single-loop search coil inside the STELDOR resonator is shown in Figure 6.4. The rise or decay time of the field pulse inside the resonator was approximately 40 ns. The system performance was limited by how quickly the field could be returned to the original static magnetic field B_0. The pulsed stepped-field was calibrated by observing the FID response from a small single crystal of α,γ-bisdiphenylene-β-phenylallyl complexed with benzene (BDPA) (Aldrich Chemical) when excited with a single stepped-field-encompassed microwave pulse. The

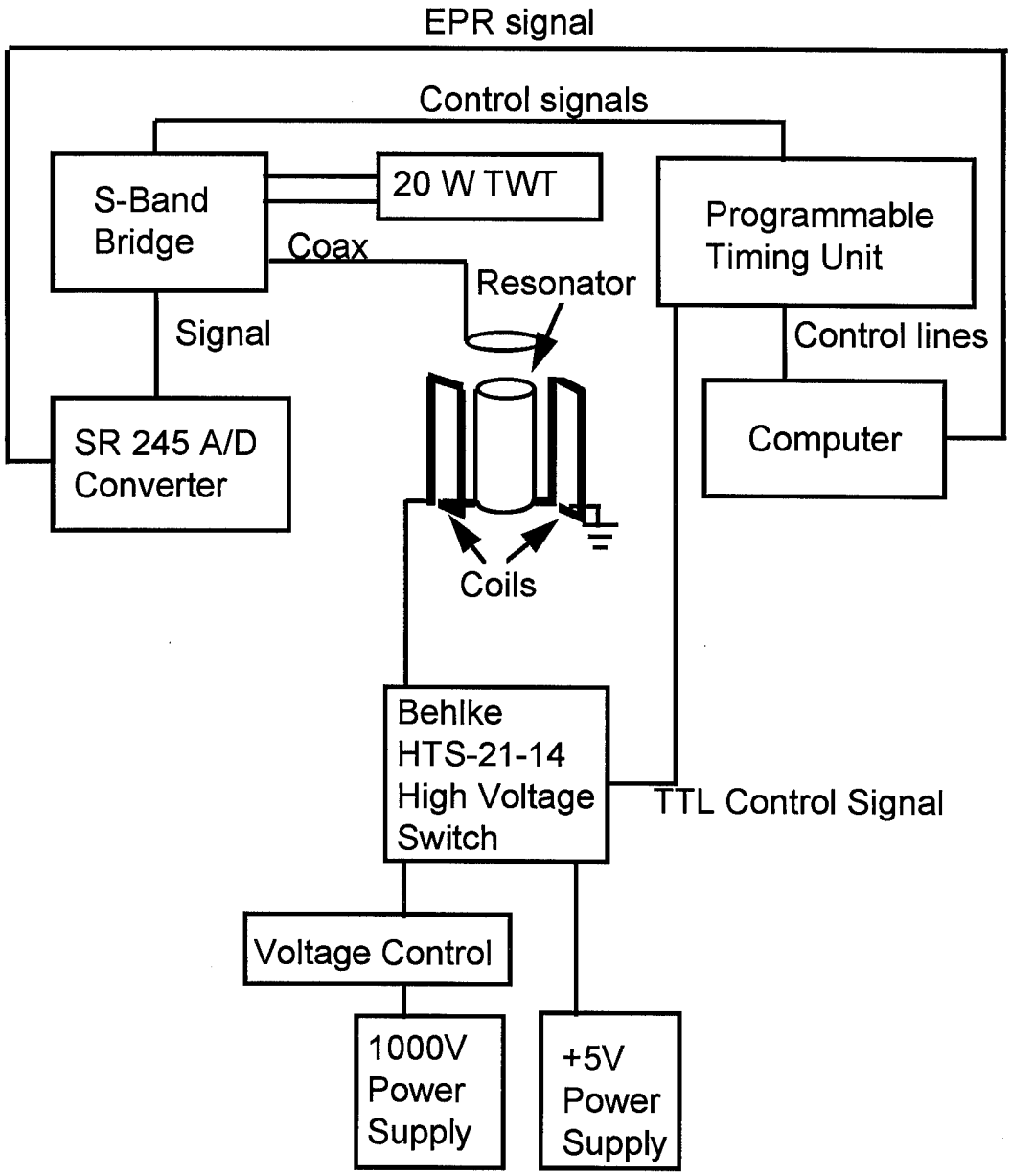

Figure 6.2. Pulsed Stepped-Field ELDOR system block diagram

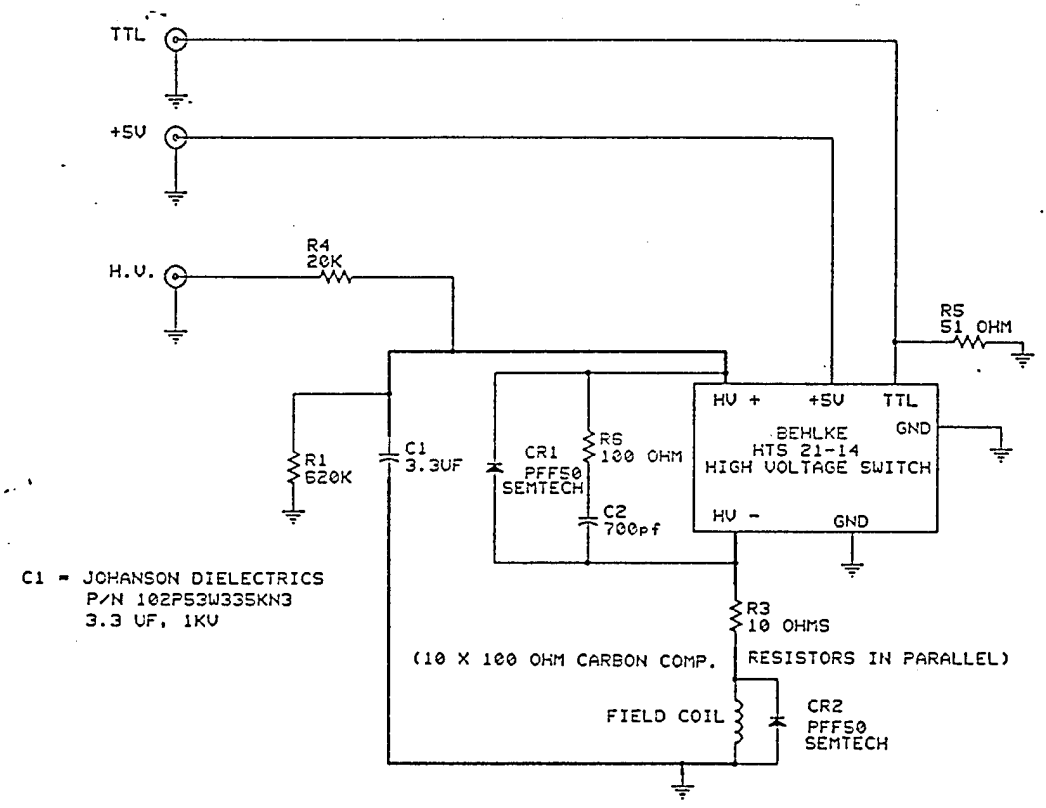

Figure 6.3. Circuit diagram for STELDOR field jump trigger. This circuit was designed by Richard W. Quine and George A. Rinard.

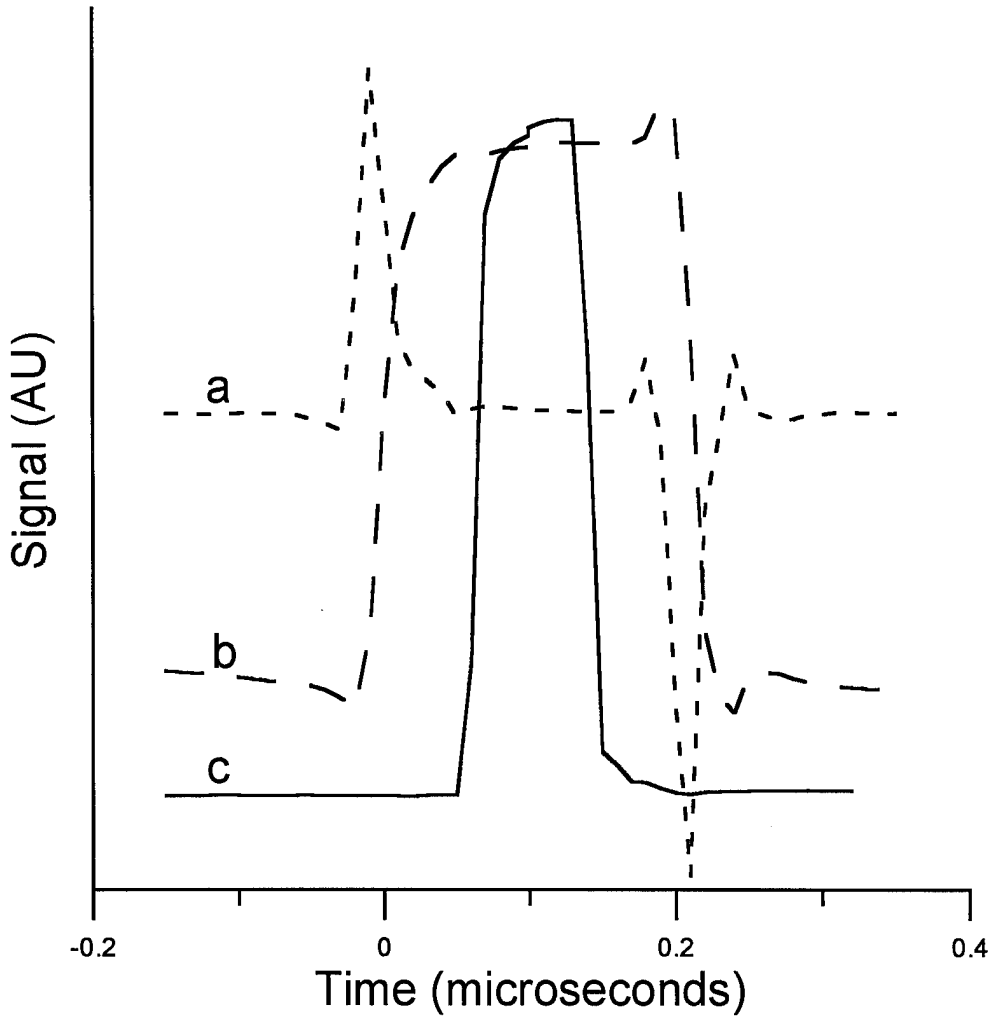

Figure 6.4. Pulsed stepped-field. The voltage induced in a loop by the pulsed stepped-field was recorded (a) and integrated (b) with a LeCroy 9310 300 MHz digital oscilloscope. The pulsed stepped-field is timed to fully encompass the first π microwave pulse (c), which was monitored with a crystal detector and also recorded with the digital oscilloscope.

pulsed stepped-field response is linear with control voltage. The timing of the experiment was computer-controlled by our locally-constructed programmable timing unit (PTU) (*27*). The timing of the pulsed stepped-field was slaved to the PTU signal that controlled the first 180 microwave pulse. The repetition rate for the experiments was 100 Hz., limited by the rate constant of the charging resistor (R4 in Fig. 6.3). David Sloop has constructed a fast field-jump system using an analogous approach, but without the constraints imposed by the quantity of metal (resonator, shield, magnet, etc.) near the sample in our spectrometer (*28*).

The important requirements for the resonator assembly were that the resonator had to pass the rapidly-changing magnetic fields, and the field jump coils had to be mounted close to the resonator, but outside the resonator assembly shield to reduce eddy currents. Brown and Sloop developed the first cavity for a very rapid large change in the magnetic field (*29*). Bridged LGRs have been used successfully with high frequency radiation (*30*) and readily passed a magnetic field jump, but the bridged LGR resonator assembly would not accommodate the requirement that the field jump coils be mounted close to the resonator, yet outside the shield. CuFlon copper film LGRs (described in chapter 3) also passed the rapidly changing magnetic fields required in this experiment (*31*), so we designed and built the pulsed STELDOR resonator from this versatile material. The resonator assembly is shown in Figure 6.5.

The resonator was an omega-shaped 1-loop, 1-gap re-entrant LGR with 4.2 mm diameter and 10 mm length sample loop. The resonator was etched from the CuFlon by the process described in chapter three. One whole side of the copper coating of the CuFlon was etched off, and the slots for passing the rapidly-changing magnetic field was etched into the copper coating on the other side. The

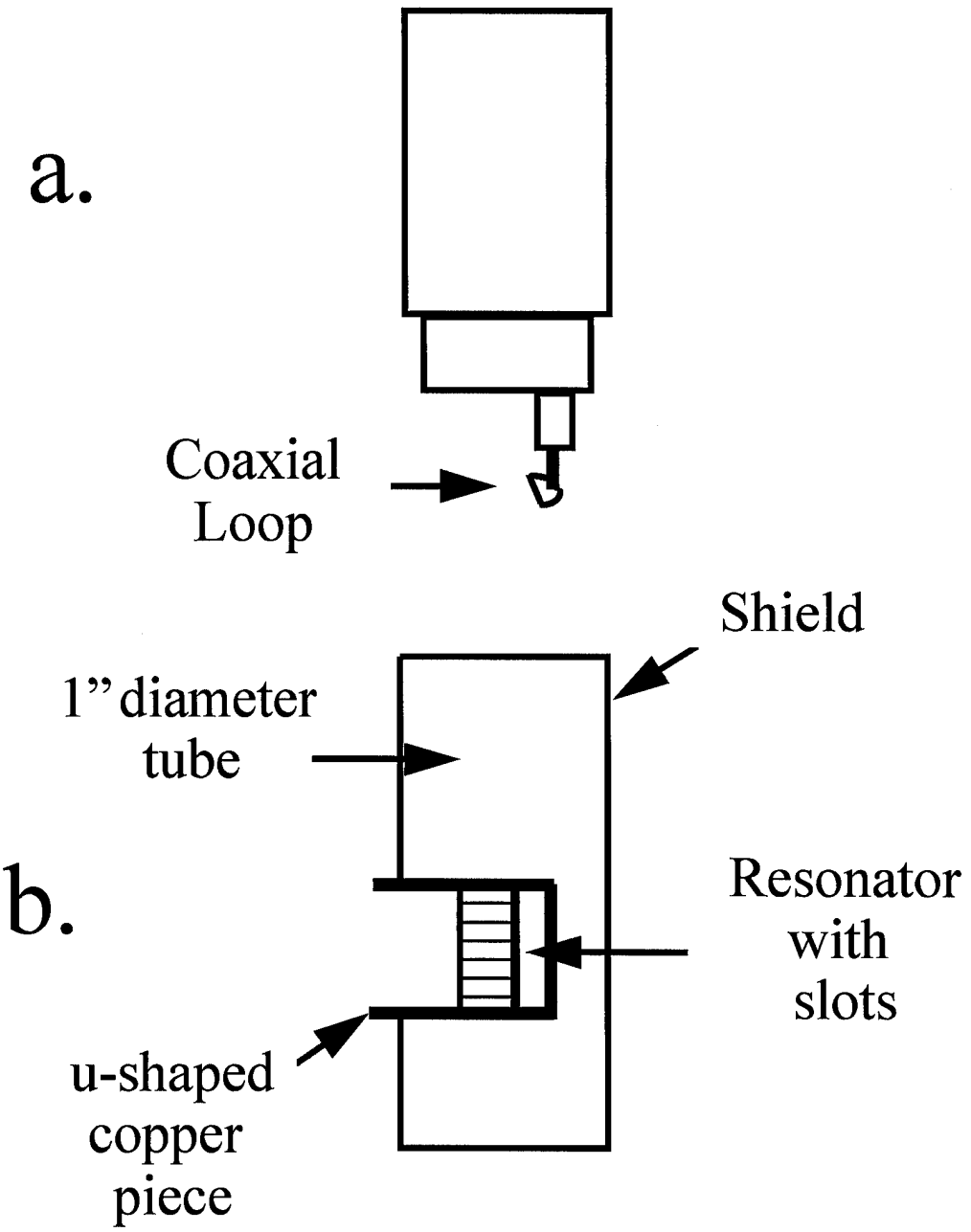

Figure 6.5. Pulsed STELDOR LGR assembly with a one-gap, one-loop LGR (detailed in Figure 6.7). a. Side-view of coupling loop assembly that inserts into the shield. b. Side-view of shield and resonator, not including the Rexolite support.

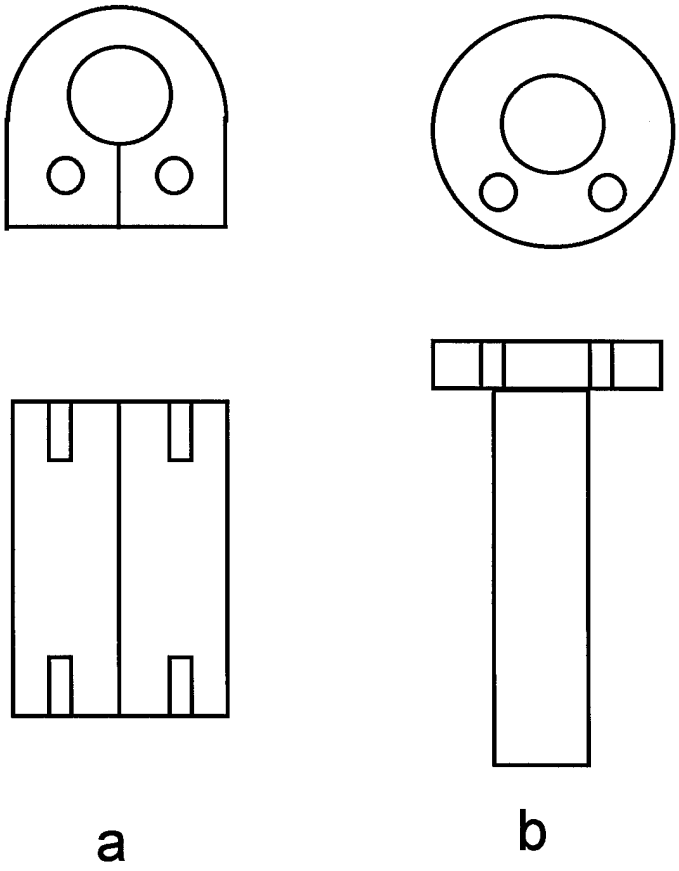

Figure 6.6. Rexolite support and sleeve insert for pulsed STELDOR copper film resonator. (a) top and side views of the Rexolite support. (b) top and side view of the Rexolite sleeve insert and mounting plate. The Rexolite sleeve is 3/1000 th of an inch in thickness and compresses the copper film against the outer Rexolite support.

resonator was supported in Rexolite (Figure 6.6). The etched CuFlon was inserted into the Rexolite support with the copper layer facing out toward the Rexolite support. The capacitive gap (Figure 6.7) was created by clamping the two layers of the Teflon substrate in the slot of the Rexolite. Additional Teflon (5 mil thick square) was placed between the two Teflon layers in the gap to decrease the capacitance and bring the final resonant frequency to 3.4 GHz. The Rexolite was placed into a u-shaped copper piece that forms a part of the shield (Figure 6.5). Holes were drilled in the copper sheet to match the holes in the Rexolite support, the sleeve mounting plate, and the sample tube opening. Slits were cut to match the slots in the Rexolite support that formed the capacitive gap. Lossy substances including adhesives could not be used in the vicinity of the capacitive gap because they destroyed the loaded Q of the resonator, thus the Rexolite support and sleeve were mounted to the u-shaped copper piece with polyethylene screws. The u-shaped copper piece was soldered to a cut-out in a 3 inch segment of 1 inch diameter copper tubing (Figure 6.5) to form the shield. The resonator (Figure 6.7) was connected to the shield by soldering the ends of the copper film resonator to the grounded u-shaped copper piece. Soldering the resonator to the u-shaped copper piece restricted the microwave field to the sample loop and the coupling loop (*32*). Positioning the field jump coils next to the Rexolite support placed the coils close to the sample, but outside the shield and allowed for the smallest field jump coil geometry.

The resonator inductive coupling was adjusted by moving vertically a coaxial loop (Figure 6.5). The coaxial loop was shaped like the re-entrant loop (i.e. half circle) but enough smaller to just fit inside the re-entrant loop (Figure 6.7) to maximize overcoupling capabilities for ESE experiments. The critically-coupled

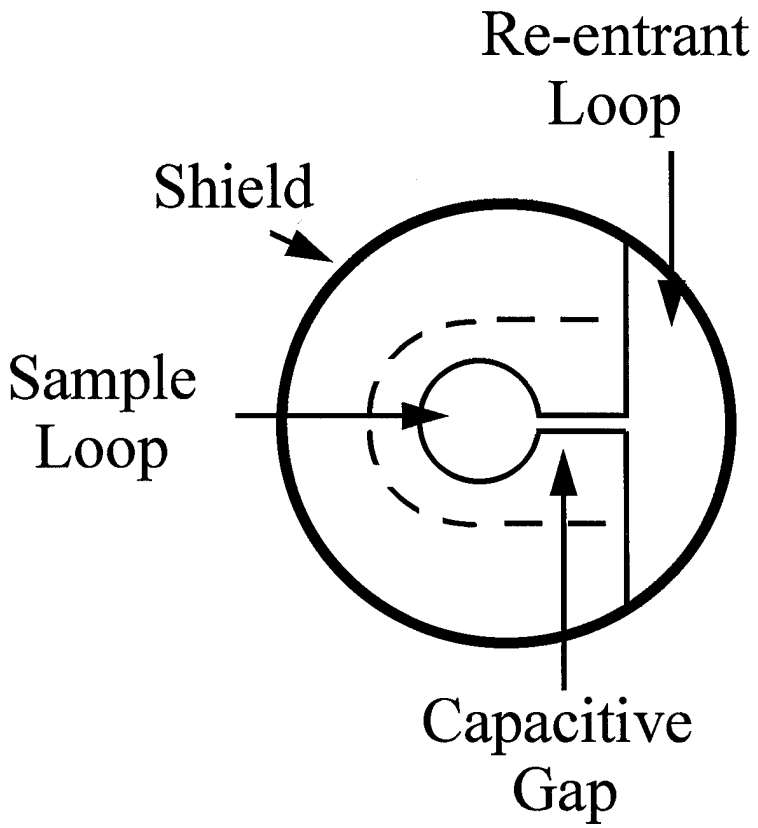

Figure 6.7. Top view of the pulsed STELDOR one-gap, one-loop LGR. The sample loop was 4.2 mm in diameter. The capacitive gap was 3 mm long. The omega-shaped resonator was soldered to the shield as described in the text, and the magnetic flux of the RF is directed through the re-entrant loop by the shields above and below the resonator (Figure 6.5). The dashed line (- - -) outlines the position of the Rexolite support shown in Figure 6.6.

loaded Q of the resonator was approximately 450. The loaded Q was estimated by digitizing the ring-down of a reflected pulse measured with a crystal detector. For the STELDOR experiments, the resonator was overcoupled to a loaded Q of approximately 170.

Each of the 60-30-60 ns microwave pulses (Figure 6.1) excites about 0.3 mT of the spectrum. This was estimated using the relationship $B_1 = \Theta/\gamma t_p$, where Θ is the flip angle in radians, γ is the gyromagnetic ratio, and t_p is the length of the pulse. The bandpass of the overcoupled resonator was about 0.7 mT estimated using the relationship $\Delta\omega = \omega_0/Q$, where $\Delta\omega$ is the bandpass of the resonator, ω_0 is the resonant frequency, and Q is the overcoupled Q of the resonator. The bandwidth of the excitation is the smaller of these two values so the bandwidth of the excitation was determined by the excitation of the microwave pulses. Without the field jump, the first π microwave pulse inverted the same spins that were sampled by the subsequent 2-pulse echo sequence, and produced an inversion-recovery signal. By using a large field-jump (relative to the bandwidth of excitation), the spins excited by the first π microwave pulse were not the same spins as were monitored by the subsequent two-pulse echo sequence. If no relaxation processes coupled the spins excited by the first pulse to the spins sampled by the 90-180 pulse sequence, the amplitude of the echo was independent of τ_1 (i.e. a constant signal when the amplitude of the monitored echo was plotted as a function of τ_1). For cases of partial overlap of the exciting and observing bandwidths, the number of spins inverted by the first microwave pulse and subsequently monitored by the 90-180° microwave pulses determined the initial amplitude of the monitor echo signal. The amplitude of the monitor echo recovers to the equilibrium value with the time constant(s) characteristic of the inversion-

recovery experiment. The starting amplitude of the monitor echo was inversely proportional to the overlap of the bandwidths for the exciting and monitoring pulses.

In the present work, National Bureau of Standards coal #1635, polycrystalline L-alanine γ-irradiated to 100 kGy with ^{60}Co, a single crystal of L-alanine γ-irradiated to 110 kGy, a single crystal of L-alanine γ-irradiated to 224 kGy, polycrystalline L-alanine d_7 (fully deuterated) γ-irradiated to 73 kGy, a single crystal of malonic acid γ-irradiated to 110 kGy, polycrystalline dimethyl malonic acid γ-irradiated to 98 kGy, and polycrystalline α-amino-isobutyric acid γ-irradiated to 98 kGy were studied at room temperature by pulsed STELDOR. The irradiations were performed at room temperature and the samples were stored at room temperature.

6.3 Results

6.3.1 NBS Coal

The two-pulse field-swept echo detected spectra of NBS coal (figure 6.8) showed a single inhomogenously-broadened signal with 0.2 mT width at half height. The line shape of the absorption was closely approximated by a sum of 70% Gaussian and 30% Lorentzian lineshapes with half-widths at half-height of 0.2 mT. An inversion-recovery pulse sequence (0 mT in Fig. 6.9) resulted in a signal with a recovery time constant of approximately 11 microseconds. The number of spins excited by the first microwave pulse and subsequently monitored by the 2-pulse sequence was decreased as the first π pulse was positioned (via the stepped magnetic field) farther from the center (Figure 6.8). When the field was stepped farther than ca. 0.75 mT, the number of spins excited by the first

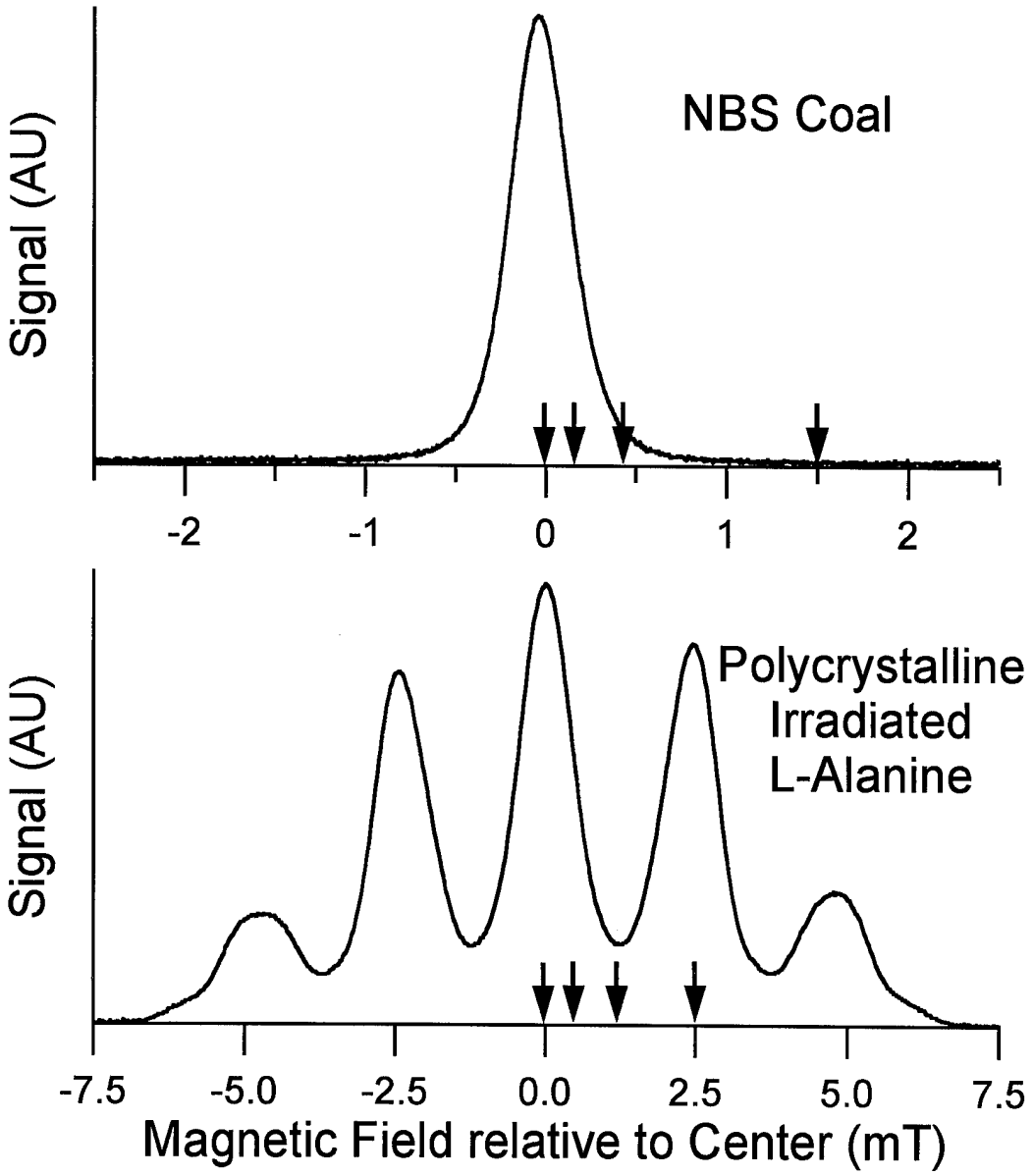

Figure 6.8. Field-swept echo-detected absorption spectra recorded by boxcar integration of the echo following 30-60 ns microwave pulses, using fixed τ = 180 ns. The aperture was positioned such that the boxcar integrated the back half of the echo signal to maximize resolution. The arrows show the position of the first excitation pulses for Fig. 6.9 and Fig. 6.11 pulsed STELDOR signals. The samples are described in the text.

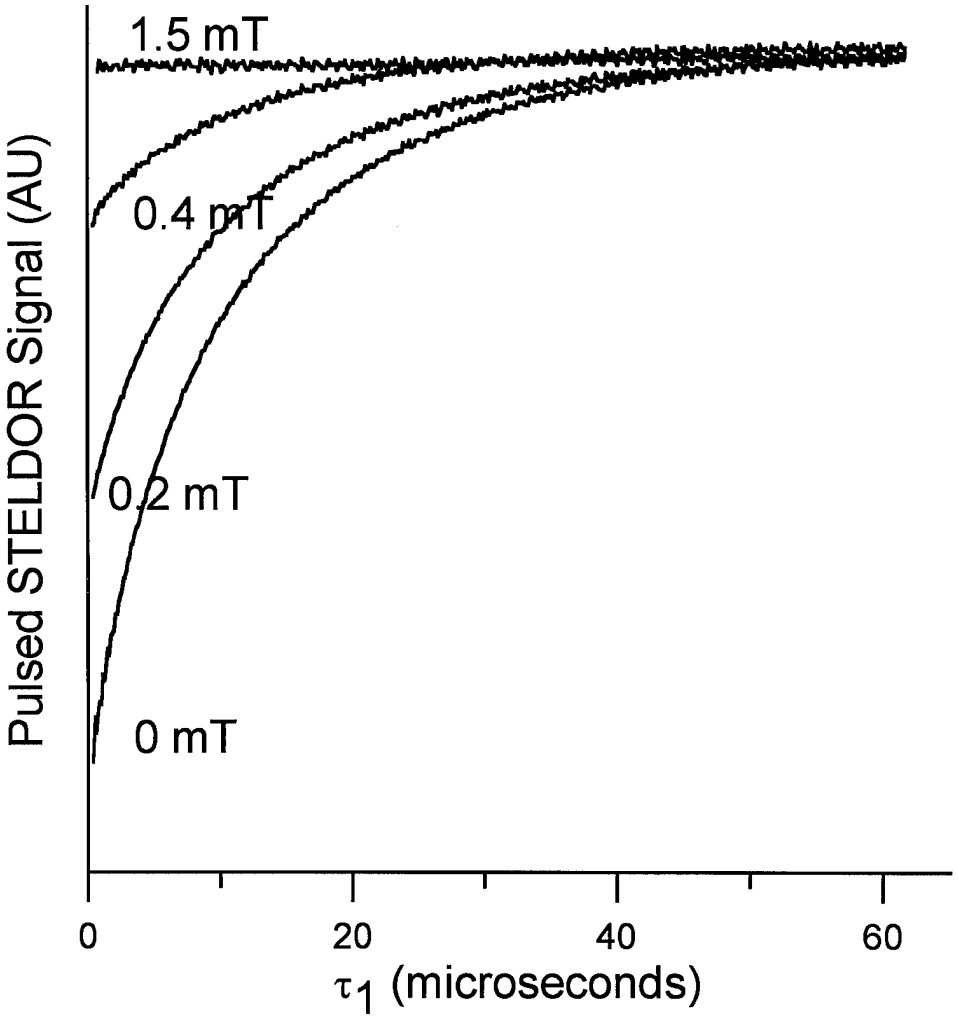

Figure 6.9. Pulsed STELDOR signal of NBS coal # 1635. The curves show the echo amplitude at the center of the EPR spectrum following a 60-τ_1-30-τ_2-60 ns pulse sequence, τ_2=180 ns, for varying magnitudes of the pulsed stepped-field, at which the first microwave pulse was applied.

microwave pulse and then monitored by the subsequent 2-pulse sequence became negligibly small, and the monitor echo height was independent of τ_1.

Pulsed STELDOR experiments for coal were simulated by multiplying the normalized function describing the coal absorption with the Fourier transform Tophat function for a 60 ns microwave pulse (Figure 6.16) (*33*) and the transfer function of a resonator with a loaded Q of 170 at 3.4 GHz. The integration of the resulting function approximated the number of spins excited by a 60 ns microwave pulse. The fraction of spins excited by the first microwave pulse and then monitored by the subsequent 2-pulse sequence was calculated by finding the overlap between the observe (0 mT position) and field-jumped excitation functions. The calculated and experimental overlap fractions are compared in Table 6.1. The measurements and calculations on the coal sample provided a test of the spectrometer performance.

6.3.2 Irradiated L-alanine

The structure for the radical in irradiated L-alanine is

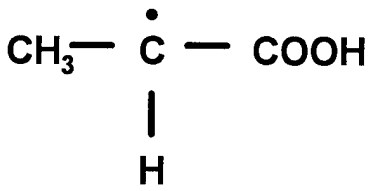

The field swept echo detected absorption spectrum of polycrystalline irradiated L-alanine appears as 5 lines separated by approximately 2.5 mT (Figure 6.8) due to the accidental near-equivalence at room temperature of the coupling to the rapidly-rotating methyl protons and the average coupling to the anisotropic α–proton of

Table 6.1. Calculated and experimental overlap fractions for NBS coal #1635

Field Jump	**Calculated overlap**	**Observed overlap**
0.2 mT	0.7	0.61
0.4 mT	0.28	0.23
0.75 mT	0.01	0.01
1.5 mT	0	0

the trapped radical (Figure 6.8) (*34*). The absorption spectrum was closely approximated by a sum of Gaussian and Lorentzian lineshapes as shown in Figure 6.10. This type of fit gives a semi-quantitative description of the shape. The spectrum is the result of accidental coincidence of values, and there are spin-flip lines and other features that make the spectrum much more complicated than this 5-line description (*34,35*). The parameters for the 5-line simulation are listed in Table 6.2. An inversion-recovery sequence yielded a signal that recovered with either two time constants of approximately 1 and 8 μs and an ambiguous third time constant of approximately 0.3 μs. The effect of the first microwave π pulse on the monitor echo decreased when the first pulse was positioned further from the center of the spectrum, but still within the central inhomogeneously broadened peak of the spectrum (curves for 0, 0.375, and 1.2 mT field jumps in Figure 6.11).

Pulsed STELDOR experiments for polycrystalline irradiated L-alanine were simulated by multiplying the normalized function describing the L-alanine absorption with the Fourier transform Tophat function for a 60 ns microwave pulse and the transfer function of a resonator with a loaded Q of 170 at 3.4 GHz. Table 6.3 shows the calculated and experimental results for irradiated L-alanine.

When the location of the inverting pulse was stepped 2.5 mT, which positioned it in an adjacent hyperfine line, the calculated overlap of the spins excited by the first microwave pulse and the spins monitored by the subsequent 2-pulse sequence is negligibly small, assuming there is no transfer of magnetization. Without transfer of magnetization, the expected pulsed STELDOR response for such a large field step is a flat response as shown for NBS coal in Figure 6.9 (top curve). Instead of the flat response for the 2.5 mT field jump pulsed ELDOR signal of irradiated L-alanine, the amplitude of the monitor echo initially increased,

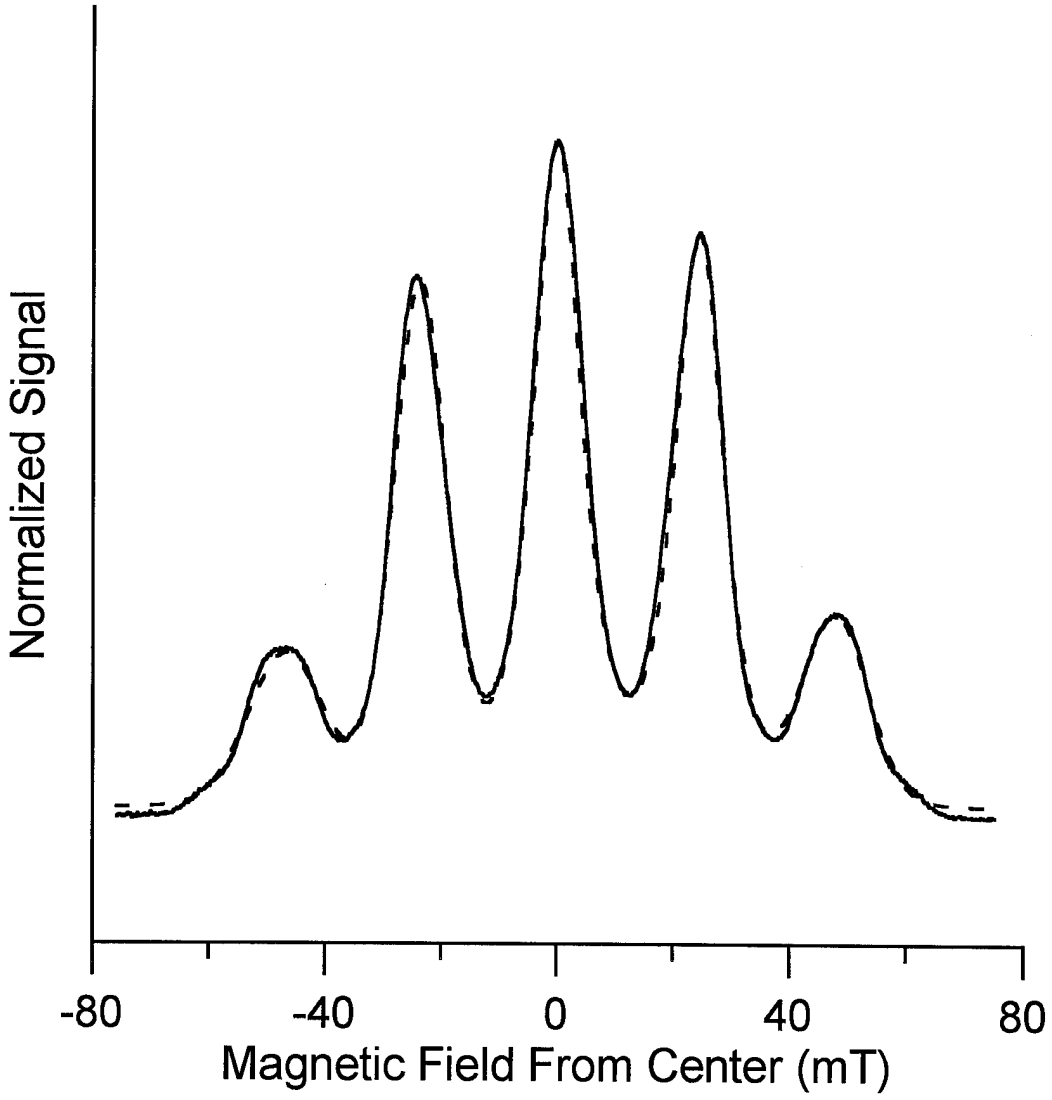

Figure 6.10. Simulation (- - -) of the absorption spectrum (—) of irradiated L-alanine. The parameters of the fit are given in Table 6.2. The simulation was accomplished using Microsoft Excel® as described in the text.

Table 6.2. Simulation parameters for polycrystalline irradiated L-alanine absorption

Line Number	%Gaussian	Normalized Peak Heights	Half-width at Half-height	Position from center (mT)
1	100	0.22	7.5	-47
2	80	0.8	5.4	-23.8
3	30	1	5	0
4	45	0.84	5	24.5
5	100	0.23	6.5	48

Table 6.3. Calculated and experimental overlap fractions for polycrystalline irradiated L-alanine

Field Jump	**Calculated overlap**	**Observed overlap**
0.375 mT	.35	.35
1.2 mT	.02	.02
2.5 mT	.0001	-.07

Table 6.4. Pulsed STELDOR enhancements for irradiated polycrystalline L-alanine

pump field from center (mT)	**observe field from center (mT)**	**enhancement**
7.5	5.0	no
5.0	2.5	yes
2.5	0	yes
0	-2.5	yes
-2.5	-5.0	yes
-2.5	0	yes

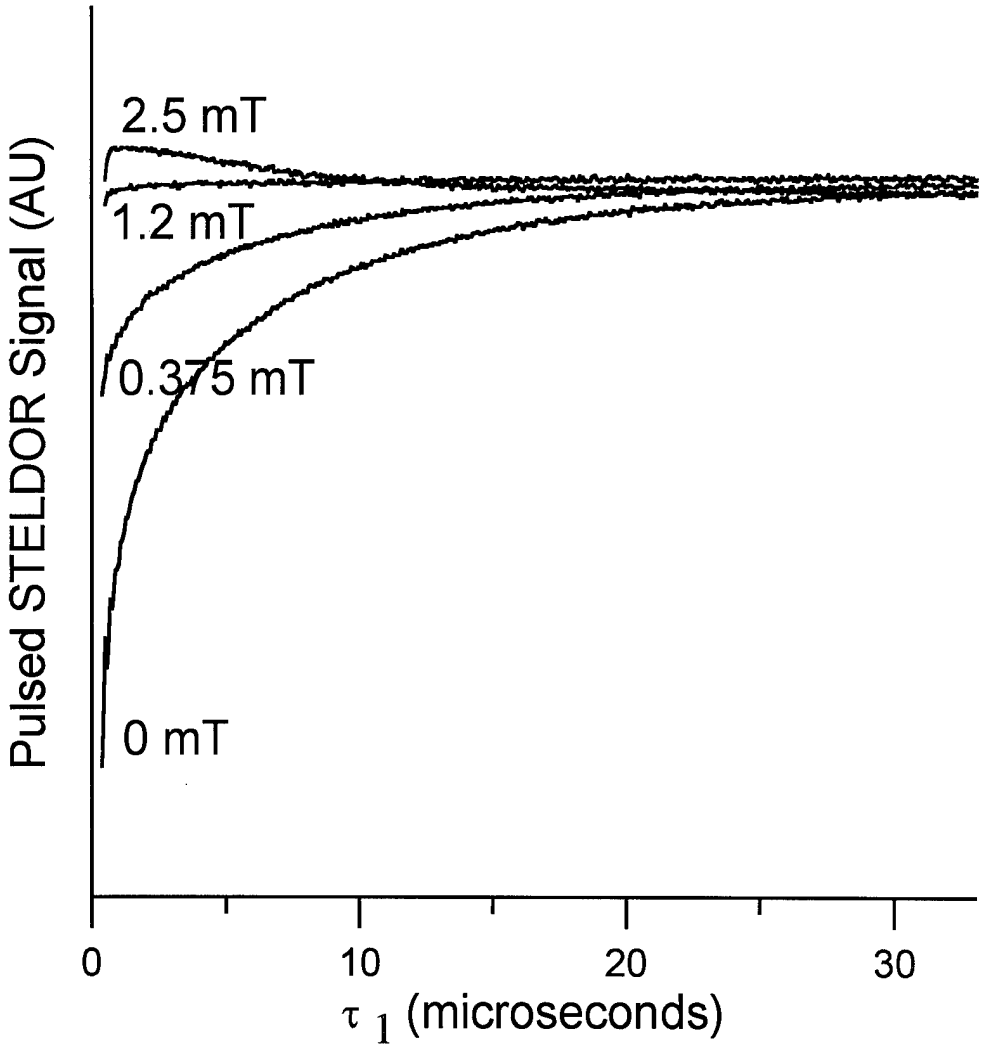

Figure 6.11. Pulsed STELDOR signal of irradiated L-alanine. Echo amplitude at the center of the EPR spectrum following a 60-τ_1-30-τ_2-60 ns pulse sequence, τ_2=180 ns, is plotted as a function of τ_1 for varying magnitudes of the pulsed stepped-field.

and then decayed back down to the equilibrium level (Figure 6.11, top curve). Table 6.4 summarizes several experiments in which the enhancement of echo amplitude was observed whenever the inversion pulse was applied to one "line" of the "5-line" pattern, and the monitor echo was observed at the field position corresponding to an adjacent line. Limitations of the apparatus did not permit 5 mT jumps to study non-adjacent lines.

To investigate the possible role of the anisotropy of the coupling to the α-proton, an irradiated single crystal of L-alanine positioned to either minimize or maximize the effect of the anisotropy of the coupling to the α-proton was studied with pulsed STELDOR. The field-swept echo-detected EPR spectra for the two orientations of the single crystal L-alanine are shown in Figure 6.12. Both orientations produced similar results. The inversion-recovery signal for both had a biexponential recovery with time constants of approximately 0.6 and 6 μs. Both orientations gave approximately the same pulsed STELDOR signal: when the center of the neighboring hyperfine line was excited by the first microwave pulse and the echo monitored by the subsequent 2-pulse sequence, the amplitude of the monitor echo increased initially and then decayed to an equilibrium amplitude. Although many different combinations of what position of the spectrum was excited by the first microwave pulse and what position was observed by the subsequent 2-pulse sequence were examined, the only occurrence of the enhancement signal came when a neighboring hyperfine line was excited with the first microwave pulse and a different hyperfine line was observed. No enhancement signal was seen for any combination of the first microwave pulse and subsequent 2-pulse monitor echo sequence within the same hyperfine line.

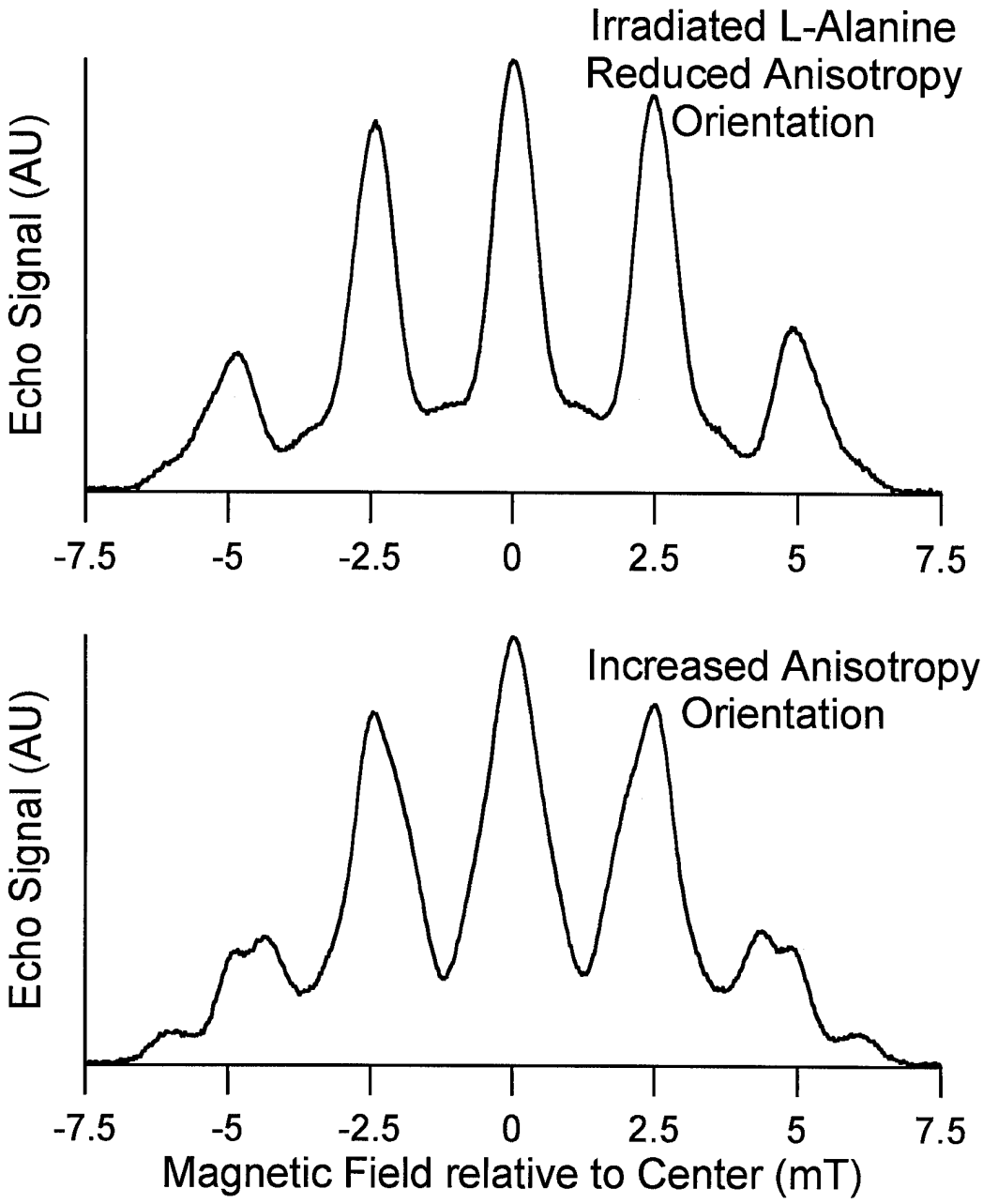

Figure 6.12. Field-swept echo-detected EPR spectra of single-crystal L-alanine recorded by boxcar integration of the echo following 30-60 ns microwave pulses, using fixed τ_1 = 180 ns.

The enhancement signal, when analyzed with a computer nonlinear curve fitting and model development program, MINSQ (Micromath, Salt Lake City, UT), showed two components. The enhanced signal grew with a time constant of approximately 0.6 μs and decayed with approximately a 6 μs time constant. These times agree, within experimental uncertainties, with the inversion recovery time constants of the polycrystalline and single crystal irradiated L-alanine.

To investigate the role of the intermolecular electron-electron interactions (instantaneous diffusion), a single crystal of L-alanine irradiated to a higher irradiation dosage of 224 kGy was studied. If the intermolecular electron-electron interactions are responsible for the enhanced pulsed STELDOR signal, increasing the irradiation dosage should increase the electron-electron intermolecular interactions and an even larger pulsed STELDOR should result. If no additional enhancement occurred in pulsed STELDOR, the enhancement is not likely the direct result of electron-electron intermolecular interactions. Increasing the dosage of radiation did not increase the enhancement signal relative to the total echo amplitude. Both the 100 kGy and 224 kGy samples produced an enhancement of about 5% relative to the equilibrium monitor echo amplitude. Thus, the enhanced pulsed STELDOR signal is not due to intermolecular electron-electron interaction.

6.3.3 Irradiated L-alanine-d_7

To check what effects changing the nuclear moment would have on the pulsed STELDOR signal, irradiated polycrystalline L-alanine-d_7 was studied. The field-swept echo-detected EPR spectrum of irradiated L-alanine-d_7 has 21 overlapping lines that appear as a nine-line absorption spectrum (Fig. 6.13) analogous to the accidental five-line spectrum in irradiated non-deuterated L-

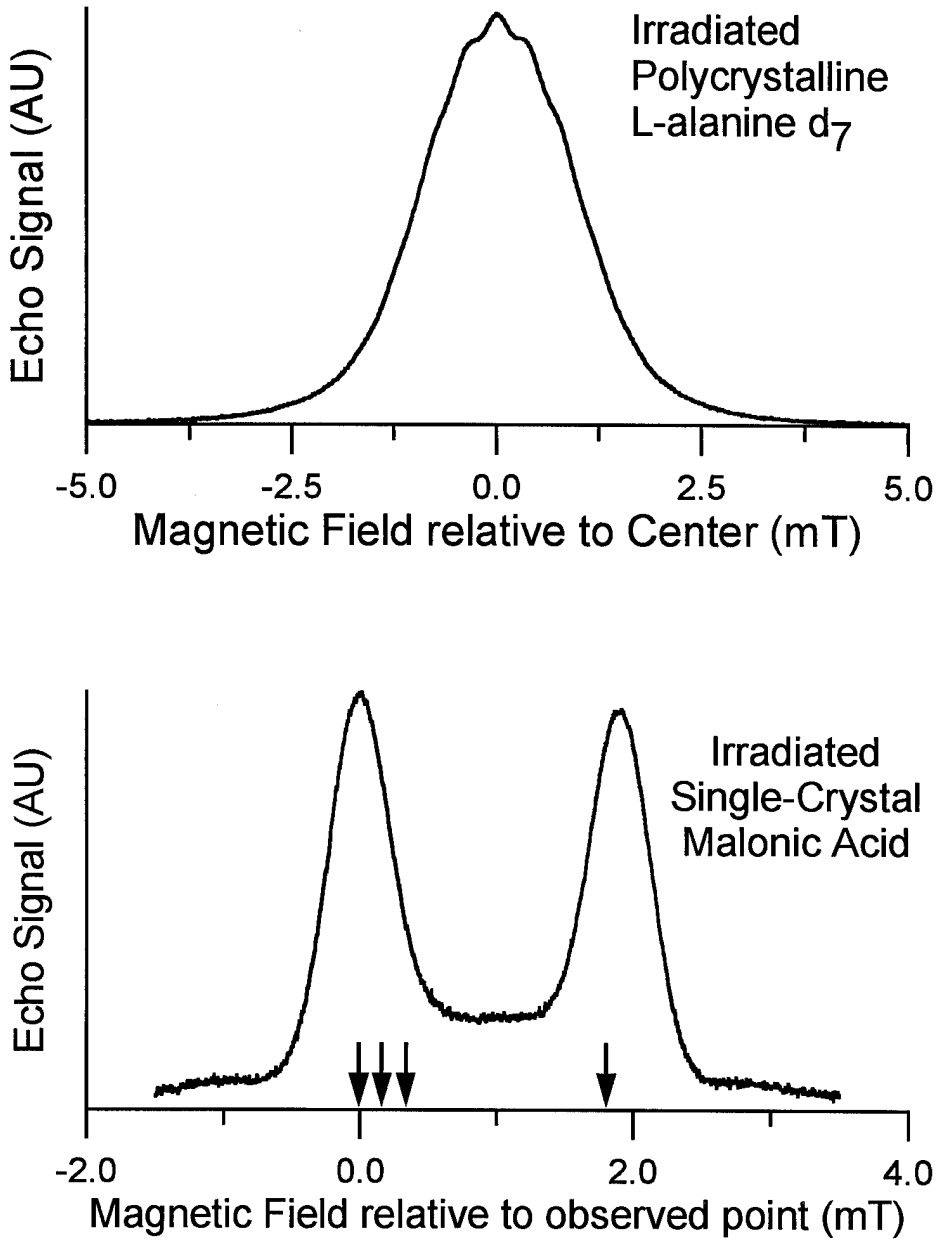

Figure 6.13. Field-swept echo-detected EPR spectra recorded by boxcar integration of the echo following 30-60 ns microwave pulses, using fixed τ_1 = 180 ns. The arrows show the position of the first excitation pulses for Fig. 6.15 pulsed STELDOR signals.

alanine (*38*). X-band long-pulse SR results showed that the deuteration produced resultant T_1 times that were longer than without deuteration by about the ratio of the nuclear moments between the proton and deuteron (ca. 5.9 vs. 6.5).

The pulsed STELDOR results for this sample showed no enhanced signal. The results were similar to NBS coal. The effects of the first π microwave pulse on the amplitude of the monitor echo decreased as the field step for the first π microwave pulse was increased. This was true whether the monitor echo was observed at the center of the line, or on the side of the line. For example, in one experiment the echo was observed at the position 1 mT downfield from the center of the spectrum, and the field was stepped 2 mT upfield from the observed position to 1 mT upfield from the center of the spectrum to apply the first π microwave pulse. In contrast to the protonated sample, the deuterated sample did not exhibit enhancement of the echo under any condition studied. The inversion-recovery measurement on the deuterated sample yielded an echo that recovered with two time constants of approximately 1.7 and 6.5 microseconds. The time window for the pulsed STELDOR signal was 5 times the longest inversion-recovery time component (35 microseconds). Thus, deuterating the L-alanine eliminated the enhanced pulsed STELDOR signal.

6.3.4 Irradiated malonic acid

The field-swept echo-detected EPR spectrum of irradiated single-crystal malonic acid has two lines (Fig. 6.13) (*39*). Irradiated malonic acid was studied because it lacks a methyl group and because Nechtschein and Hyde have previously investigated this radical species with pulsed ELDOR (*40*). We postulated that the rotating methyl groups have a large role in the enhanced pulsed

STELDOR signal and explored irradiated malonic acid to test this hypothesis. Indeed, the irradiated malonic acid sample did not produce an enhanced pulsed STELDOR signal. The pulsed STELDOR results for this sample were again very similar to those for NBS coal (Fig. 6.14). An inversion recovery sequence yielded a signal with two time constants of approximately 10 and 30 microseconds. The effects of the first π microwave pulse on the amplitude of the monitor echo decreased as the field step for the first π microwave pulse was increased. The time window for observing the pulsed STELDOR signal was 215 microseconds. No enhancement of the echo signal was observed under any conditions for the irradiated malonic acid sample.

6.3.4 Irradiated dimethyl malonic acid and α–aminoisobutyric acid

Another test of the effect of relative importance of methyl groups, rather than the α-H on the enhanced signal in the pulsed STELDOR experiment used irradiated polycrystalline dimethyl malonic acid and α-aminoisobutyric acid. The radical produced by irradiation of these species has been identified (*41*) as the following radical.

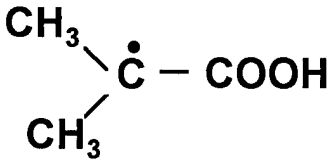

There are 6 methyl protons, and no α-proton. Figure 6.15 shows the field-swept echo-detected EPR spectra of the two samples. Although it was concluded based on CW EPR that irradiation of the samples produce the same radical (*41*), our time-domain measurements reveal that the environments of the unpaired electron are very different. Within the accuracy allowed by the presence of deep proton

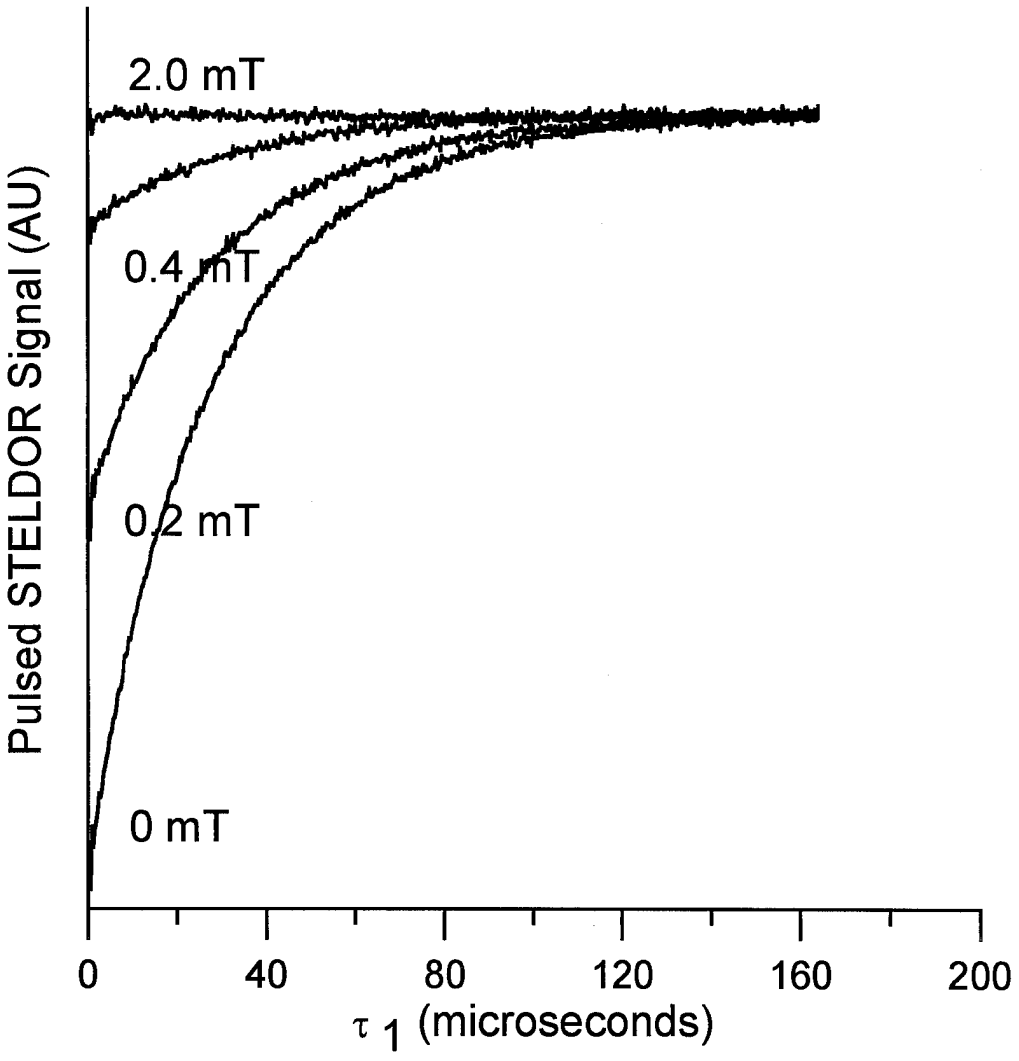

Figure 6.14. Pulsed STELDOR echo signal amplitude of irradiated malonic acid. Echo amplitude at 0 mT position (Fig. 6.14) of the EPR spectrum following a 64-τ_1-32-τ_2-64 ns pulse sequence, τ_2=300 ns, for varying magnitudes of the pulsed stepped-field. The monitor echo in the 2.0 mT shows an artifact common in the earlier version of the pulsed STELDOR apparatus where the B_o would not fully stabilize for up to 4 μs after a field jump greater than 2.0 mT.

modulation in the 2-pulse echo decay signal, the radical in irradiated α-aminoisobutyric acid had a T_m of approximately 0.16 μs while the radical in irradiated dimethyl malonic acid had a T_m of about 0.42 μs. While the X-band CW spectra of the two samples are similar (*41*), the much shorter phase memory time of the radical produced from α-aminoisobutyric acid made the spectra obtained by the field-swept echo-detected method different (Figure 6.15). The inversion recovery data for irradiated dimethyl malonic acid were biexponential with recovery times of approximately 5 and 21 μs. The inversion recovery data for the radical produced from α-aminoisobutyric acid yielded biexponential recovery times of approximately 2 and 10 μs. Although the radical formed in each case has been identified (*41*) and shown to contain two equivalent methyl groups and no other C-H moieties, only the irradiated α–aminoisobutyric acid showed enhancement in the pulsed STELDOR experiment (2-3% enhancement). Clearly, the presence of methyl groups (as in the irradiated L-alanine) play an important role in the enhancement of the pulsed STELDOR echo signal, but other factors also must influence whether an enhancement is observed.

6.3.4 Possible Artifacts

During preliminary communications of these results (*42*), the question was raised by Dr. Michael Bowman whether the enhanced echo observed when the field step was 2.5 mT was caused by the distribution of frequencies generated by short square microwave pulses. The distribution of frequencies for a 60 ns microwave pulse centered at 3.4 GHz was calculated using the Fourier transform Tophat function (Figure 6.16). Calculations show that the first crossover point occurs at approximately 0.6 mT from center frequency, and the first and second

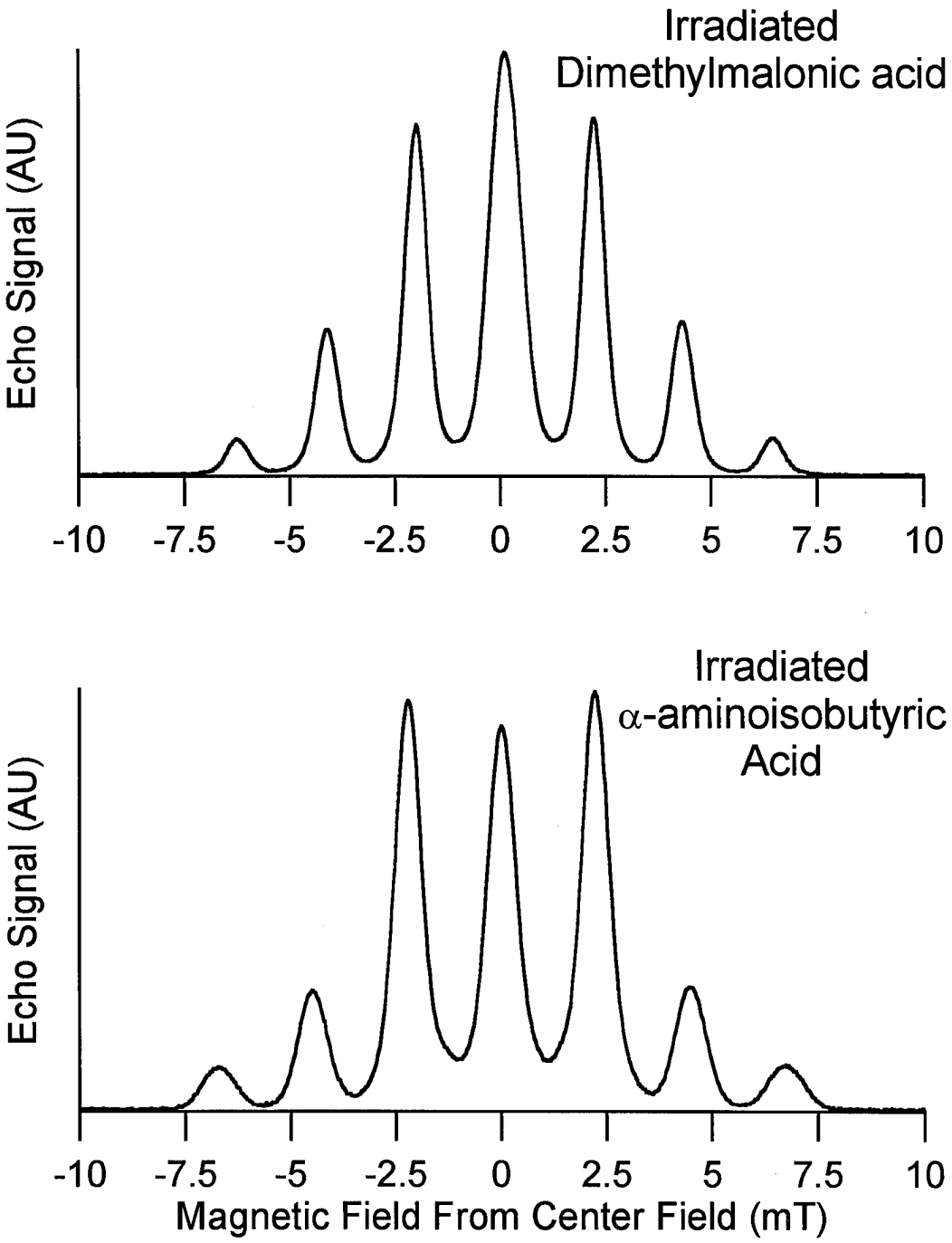

Figure 6.15. Field-swept echo-detected EPR spectra recorded by boxcar integration of the echo following 30-60 ns microwave pulses, using fixed τ_1 = 180 ns.

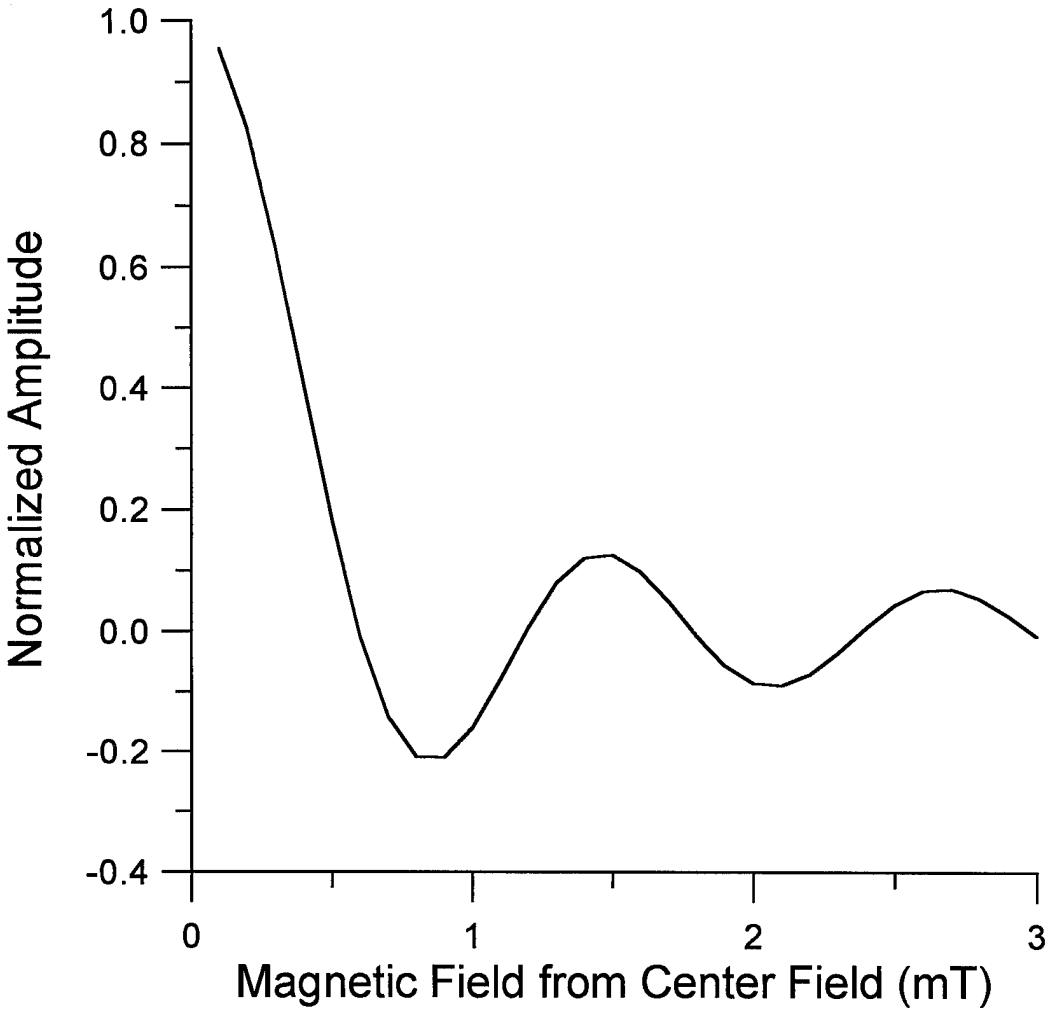

Figure 6.16. Tophat Fourier transform for 60 ns square microwave pulse.

negative peaks occurred at 0.9 and 2.1 mT from the center frequency. Normalizing the function and combining it with the transfer function (bandpass) of a resonator with a loaded Q of 170 at 3.4 GHz showed the calculated amplitude of the negative peak frequencies to be less than 1 percent of the center frequency. They would not be significant at 2.5 mT from the center.

Rapid-passage effects have affected CW ELDOR by providing relaxation pathways that compete with the electron-nuclear dipolar mechanism thereby diminishing the ELDOR effect (*43*). Pulsed STELDOR involves rapid changes in the magnetic field. If these occur while microwaves are incident on the sample, they could cause rapid-passage effects. Since we know that the magnetic field is not perfectly uniform during the microwave pulse (Figure 6.4), we performed tests to determine the significance of the imperfections for pulsed STELDOR. If the pulsed stepped-field is not timed properly, the first microwave π pulse could be subjected to a rapidly changing magnetic field (i.e. the field jump rise or fall). To check what effect a poorly timed magnetic pulse might have on the STELDOR signal, the pulsed stepped-field timing was shifted in relation to the microwave pulse in a variety of ways while observing a 2.5 mT field jump pulsed STELDOR signal of NBS coal. When the pulsed stepped-field was shifted but still encompassed the microwave pulse, no changes were apparent in the pulsed STELDOR signal (i.e., the monitor echo amplitude remained independent of τ_1). When the field jump timing was shifted so that some of the first microwave pulse was applied at the same magnetic field at which the signal was monitored, the pulsed STELDOR signal began to resemble an inversion-recovery signal. As the magnetic field-jump encompassed less of the microwave pulse, the first π microwave pulse excited the same spin systems to be later sampled by the

subsequent 2-pulse sequence. No shift of the magnetic field jump relative to first π microwave pulse produced any enhancement of the monitor echo in any of the experiments using NBS coal. For irradiated L-alanine with 2.5 mT field jump (observe at center 0 mT), as long as the microwave pulse was within the field jump, the enhancement to the pulsed STELDOR monitor echo persisted.

Other spin systems tried, but resulting in no enhanced pulsed STELDOR signal were the nitroxyl radical tempo in glassy sucrose octaacetate and tempo in polystyrene. Of the samples currently investigated, only the irradiated L-alanine and α-aminoisobutyric acid spin systems had the necessary relaxation parameters to produce an enhanced pulsed STELDOR signal. The model used to interpret the enhancement is discussed in chapter 8.

6.5 Conclusion

An S-band pulsed STELDOR system permits examination of cross-relaxation effects. A resonator and magnetic field coil system that can be inexpensively implemented has been described. The advantage of pulsed STELDOR relative to ELDOR using a LGR is that the change in the magnetic field ΔB can be greater than the bandpass of a LGR ($\Delta\omega$). The disadvantage is the slow repetition rate for the pulsed STELDOR system. The advantage of the pulsed STELDOR system relative to a CW ELDOR system is the time resolution. The observation starts with an inverted Boltzman distribution in the pumped transition giving a factor of two advantage over the saturated population condition and the change in the population condition can be observed with respect to time. Also, there is no competition between excitation and relaxation pathways during the observation period.

Room temperature S-band pulsed STELDOR signals of irradiated L-alanine and α-aminoisobutyric acid show an enhancement when the pulsed stepped field is jumped to another hyperfine line.

REFERENCES

1. V. A. Benderskii, L. A. Blumenfeld, P. A. Stunzas, and E. A. Sokolov, *Nature*, **220**, 365 (1968).

2. J. S. Hyde, J. C. W. Chien, and J. H. Freed, *J. Chem. Phys.* **48**, 4211 (1968).

3. L. R. Dalton and L. A. Dalton, *Magn. Res. Rev.* **2,** 361 (1973).

4. L. Kevan and L. D. Kispert, "Electron Spin Double Resonance Spectroscopy", John Wiley & Sons, New York, 1976.

5. J. S. Hyde, W. Froncisz, and C. Mottley, *Chem. Phys. Lett.* **110**, 621 (1984).

6. J. Gorcester and J. H. Freed, *J. Chem. Phys.* **88,** 4678 (1988).

7. J. P. Hornak and J. H. Freed, *Chem. Phys. Lett.* **101**, 115 (1983).

8. S. K. Rengan, V. R. Bhagat, V. S. S. Sastry and B. Venkataraman. *J. Magn. Reson.* **33**, 227 (1979).

9. G. G. Maresch, M. Weber, A. A. Dubinskii, and H. W. Spiess, *Chem. Phys. Lett.* **193**, 134 (1992).

10. S. A. Dzuba, A. G. Maryasov, K. M. Salikhov, and Y. D. Tsvetkov, *J. Magn. Res.*, **58,** 95 (1984).

11. S. Pfenninger, A. Schweiger, J. Forrer, and R. R Ernst, *XXIII Con. Amp. on Magn. Res.* 568 (1986).

12. G. A. Sierra, A. Schweiger, and R. R. Ernst, *Chem. Phys. Lett.* **184**, 363 (1991).

13. A. Schweiger, *in* "Modern Pulsed and Continuous-wave Electron Spin Resonance", (L. Kevan and M. K. Bowman eds.) John Wiley & Sons, New York, 43, 1990.

14. P. T. Callaghan, A. Coy, E. Dormann, R. Ruf, and N. Kaplan, *J. Magn. Res.* A., **111**, 127 (1994).

15. J. Forrer, S. Pfenninger, J. Eisenegger, and A. Schweiger, *Rev. Sci. Instrum.* **61**, 3360 (1990).

16. A. Schweiger, C. Gemperle, and R. R. Ernst, *J. Magn. Res.* **86**, 70 (1990).

17. A. D. Milov, A. Yu. Pusep, S. A. Dzuba, and Yu. D. Tsvetkov, *Chem. Phys. Lett.* **119**, 421 (1985).

18. D. J. Sloop, H. Yu, and T. Lin, *Chem. Phys. Lett.* **124**, 456 (1988).

19. G. G. Maresch, M. Weber, A. A. Dubinskii, and H. W. Spiess, *Chem. Phys. Lett.* **193**, 134 (1992).

20. K. M. Falkowski, C. P. Scholes, and H. Taylor, *J. Magn. Res.* **68**, 453 (1986).

21. G. G. Maresch and M. Mehring, *Physica*, **138B**, 261 (1986).

22. I. Z. Rutkovskii and G. G. Fodoruk, *Pribory i Tekhnika Eksperimenta*, **2**, 454 (1981).

23. A. E. Derome, "Modern NMR Techniques for Chemistry Research", Pergamon Press, New York (1987).

24. E. O. Stejskal and J. E. Tanner, *J. Chem. Phys.* **42**, 288 (1965).

25. R. W. Quine, S. S. Eaton, and G. R. Eaton, *Rev. Sci. Instrum.* **63**, 4251 (1992).

26. R. W. Quine, G. R. Eaton, and S. S. Eaton, *Rev. Sci. Instrum.* **58**, 1709 (1987).

27. R. W. Quine, S. S. Eaton, and G. R. Eaton, to be published.

28. D. J. Sloop, T-S. Lin, J. J. H. Ackerman, and S. I. Weissman, *18th International EPR Symposium*, Denver, CO., Abstract 70 (1995)

29. I. M. Brown and D. J. Sloop, *Rev. Sci. Instrum.* **38**, 695 (1967).

30. S. Pfenninger, J. Forrer, and A. Schweiger, *Rev. Sci. Instrum.* **59**, 752 (1988).

31. B. T. Ghim, G. A. Rinard, R, W. Quine, S. S. Eaton, and G. R. Eaton, to be submitted to Journal of Magnetic Resonance.

32. G. A. Rinard, B. T. Ghim, and G. R. Eaton, *17th International EPR Symposium*, Denver, CO., Abstract 189 (1994).

33. J. F. James, "A Student's Guide to Fourier Transforms with Applications in Physics and Engineering", Cambridge University Press, Great Britain, 14, 1995.

34. I. Miyagawa and W. Gordy, *J. Chem. Phys.* **32,** 255 (1960).

35. J. M. Arber, P. H. G. Sharpe, H. A. Joly, F. R. Morton, and K. F. Preston, *Appl. Radiat. Iso.* **42,** 665 (1991).

36. B.T. Ghim, J-L. Du, S. Pfenninger, G. A. Rinard, R. W. Quine, S. S. Eaton, and G. R. Eaton, *Appl. Radiat. Iso.* submitted for publication.

37. G. T. Trammell, H. Zeldes, and R. Livingston, *J. Phys. Rev.* **110,** 630 (1958).

38. K. Itoh and I. Miyagawa, *J. Chem. Phys.* **40**, 3328 (1964).

39. H. M. McConnell, C. Heller, T. Cole and R. W. Fessenden, *J. Am. Chem. Soc.* **82**, 766 (1961).

40. M. Nechtschein and J. S. Hyde, *Phys. Rev. Lett.* **24**, 672 (1970).

41. L. D. Kispert, K. Chang, and C. M. Bogan, *J. Chem. Phys.* **58**, 2164 (1973).

42. B. T. Ghim, R. W. Quine, G. A. Rinard, S. S. Eaton, and G. R. Eaton, *18th International EPR Symposium*, Denver, CO., Abstract 103 (1995).

43. M. M. Dorio and J. C. W. Chien, *J. Chem. Phys.* **62**, 3963 (1975).

CHAPTER SEVEN

Pulsed Electron-Electron Double Resonance Spectroscopy

7.1 Introduction

Pulsed ELDOR spectroscopy consists of irradiating one part of an EPR spectrum with a microwave pulse, and observing the transient response at another point in the EPR spectrum. Pulsed ELDOR can be used for the direct observation of relaxation processes, and has been implemented in two different ways. The first way pulsed ELDOR has been implemented is two-frequency pulsed ELDOR using CW detection of the observed transition (*1-5*). The second is pulsed STELDOR as discussed in chapter six. Other earlier pulsed ELDOR studies are briefly summarized in the book by Kevan and Kispert (*6*). To compare with our pulsed STELDOR experiments, two different pulsed ELDOR experiments were performed to facilitate assignment of relaxation processes for irradiated L-alanine, and α-aminoisobutyric acid. In one type of experiment, some of the spins were inverted with a π pulse at one frequency and the response of the spin system was monitored with a 90-180-echo sequence at a second frequency. For brevity, this is called inversion-ELDOR. The second type of experiment, which we will call saturation ELDOR, used a longer lower-power first microwave pulse to saturate the pumped transition followed by a 90-180-echo sequence at a second frequency to monitor the return to equilibrium.

7.2 Experimental

The S-band bridge described in chapter six was modified to create microwave pulses from two separate microwave sources. A General Microwave switch model F9120AH was used to switch the microwave source either from an external Wavetek model 962 microwave generator, or the internal microwave source. These switches have a rise and fall time of ca. 10 ns. The pulse sequence for inversion-ELDOR, shown in Figure 7.1, is equivalent to the pulsed STELDOR pulse sequence (Figure 6.1) to the extent that a small increment in field or frequency is equivalent. The first 180° microwave pulse was from the external source, and the subsequent 90 - 180 pulse sequence was from the internal source, which also was used as the reference for the double-balanced mixer detector to insure phase coherence for the detection of the spin echo. Figure 7.2 shows the saturation-ELDOR sequence in which a longer lower power first pulse is used to saturate the pump transition.

For the two-frequency ELDOR experiments, an S-band re-entrant LGR machined from a block of copper with a critical coupled loaded Q of approximately 600 that was described in Figure 4.1 was used. For the inversion-ELDOR and saturation-ELDOR studies, the LGR was overcoupled to a loaded Q of approximately 60 and the Q was estimated by digitizing the ring-down of a reflected pulse measured with a crystal detector. The resonant frequency of the overcoupled LGR was approximately 3.05 GHz.

The software of the PTU allows 64K increments of whatever resolution is picked to be the total time window for the time-domain experiments. To increase the time window of the experiments, the 32 ns resolution of the PTU was used. This resolution allows a first microwave pulse in the standard inversion-recovery

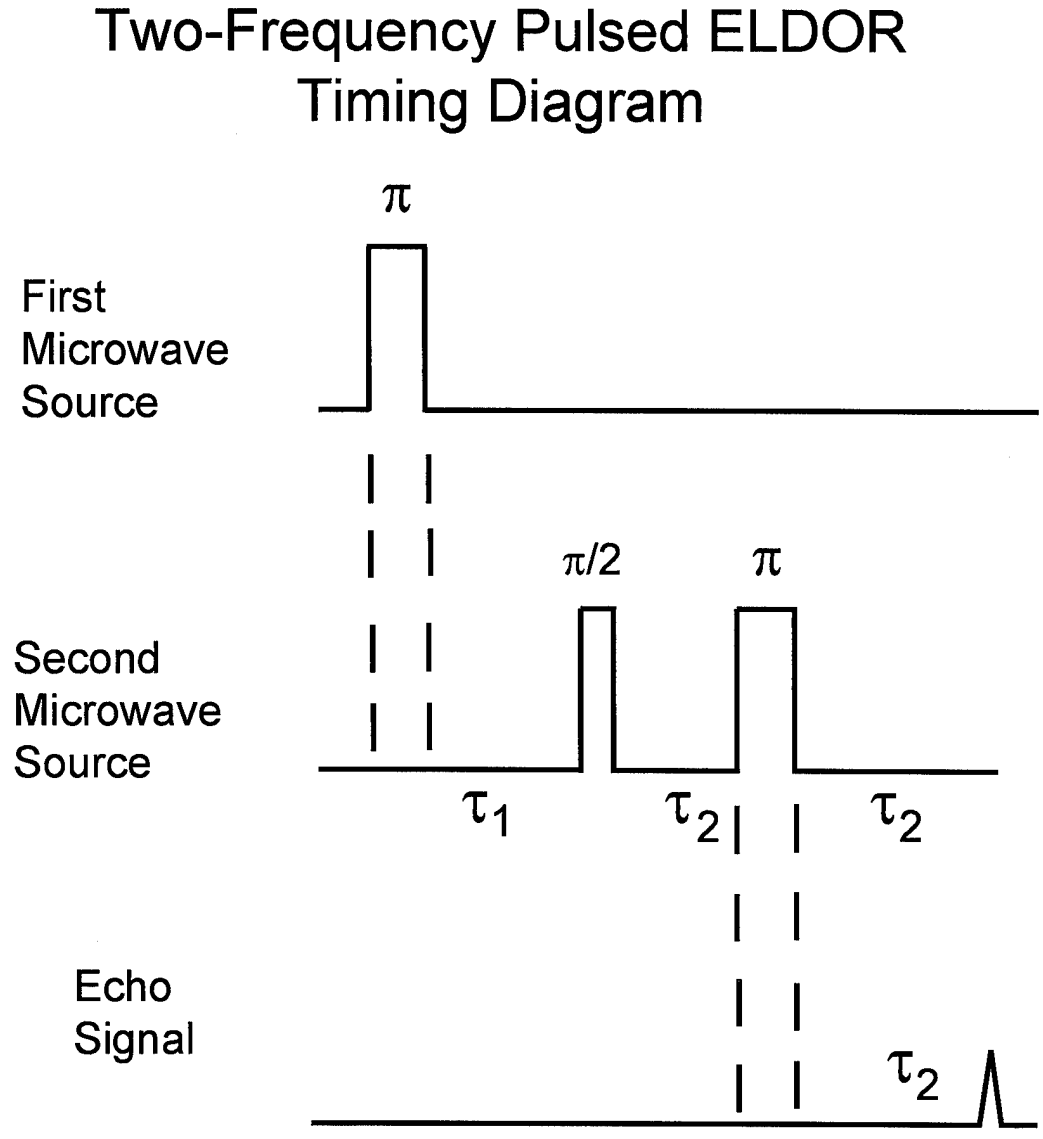

Figure 7.1. Timing diagram for the two-frequency, short first-pulse, pulsed ELDOR (inversion-ELDOR) experiment.

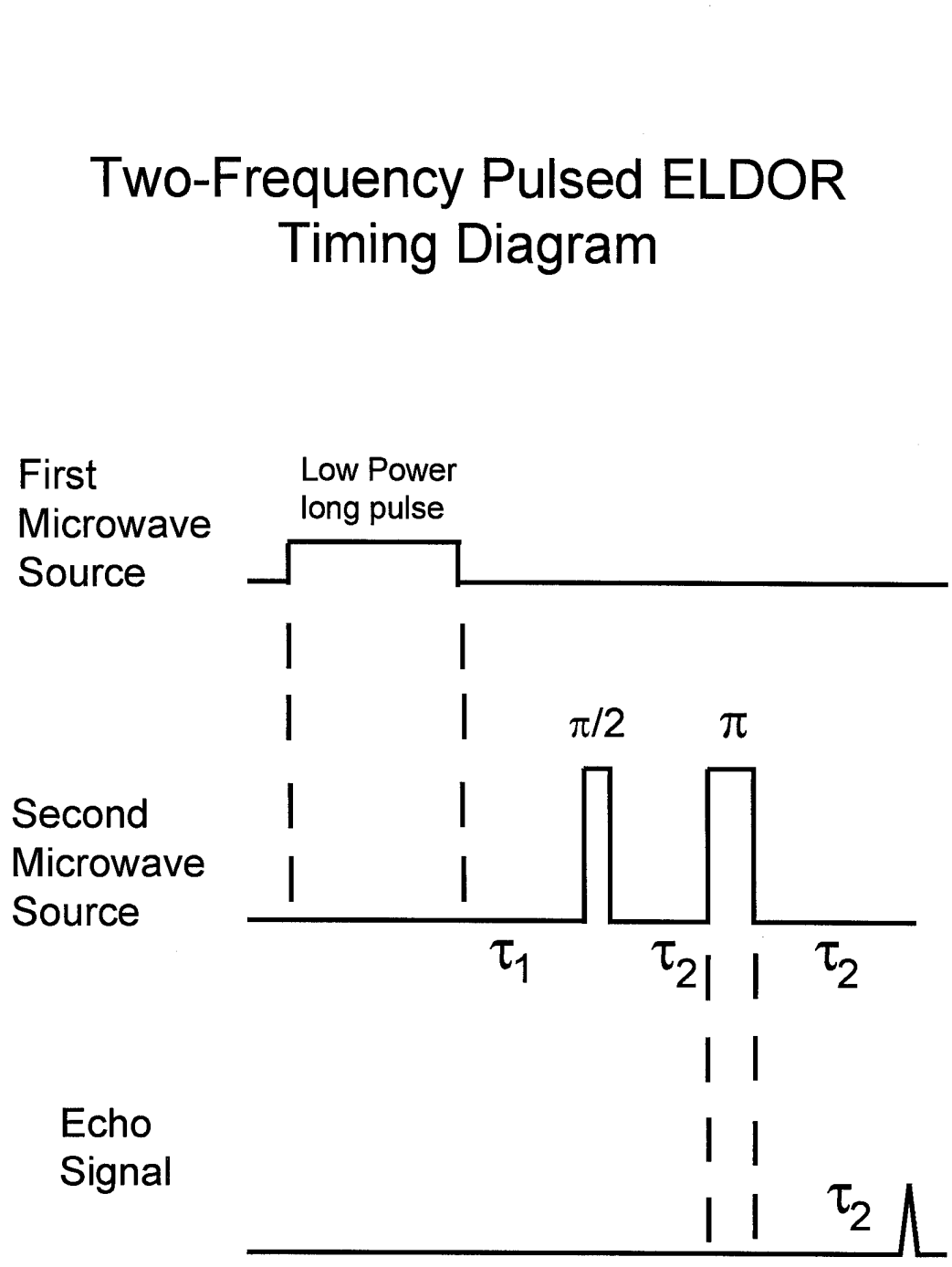

Figure 7.2. Timing diagram for the two-frequency, long first-pulse, pulsed ELDOR (saturation-ELDOR) experiment.

sequence to be from 32 ns to 320 μs long. In this mode all times are multiples of 32 ns. To compare with the pulsed STELDOR experiments, 64 ns- τ_1 -32 ns -τ_2 - 64 ns microwave pulses were used. The same effect as jumping the field in the pulsed STELDOR experiments was achieved by using a frequency difference between the first microwave pulse and the subsequent two-pulse sequence in the inversion-ELDOR experiments. In the inversion-ELDOR and saturation-ELDOR experiments, when the same frequency was used in the first and subsequent pulses, an inversion-recovery or saturation-recovery signal resulted, respectively. By increasing the frequency difference between the first pulse and the subsequent pulses, the experiment resulted in a monitor echo whose amplitude was less dependent on τ_1 except for the effects of magnetization transfer between the pumped and observed transitions.

In the present work, polycrystalline L-alanine and α-aminoisobutyric acid, γ-irradiated to 100 kGy with ^{60}Co were studied at room temperature by inversion-ELDOR and saturation-ELDOR.

7.3 Results

7.3.1 Irradiated L-alanine

An inversion-recovery sequence using 64 ns- τ_1 -32 ns -τ_2 - 64 ns microwave pulses yielded a signal that recovered with three time constants. The recovery times were approximately 0.5, 3, and 10 μs. These times were approximately the same, within experimental error, as observed in the inversion-recovery sequence presented in chapter six. When the first pulse length was changed to 96 μs, and the power of the first pulse was reduced, the three resultant recovery times changed to 0.6, 6, and 26 μs. These last two recovery times are

approximately the same as the recovery times reported in chapter four that were obtained using long-pulse saturation-recovery methods with the same sample.

The inversion-ELDOR experiment (Δfrequency = 70 MHz) yielded results similar to the pulsed STELDOR experiments in chapter 6 and showed about a 5% enhancement of the monitor echo at the highest point compared with the height of the monitor echo when Δfrequency was set to 300 MHz (i.e., off resonance). The enhancement grew in with a time constant about 0.6 μs, and decayed with a time constant about 6 μs (Fig. 7.3 and upper curve in Fig. 7.4). The recovery signal monitored with a 90-180-echo sequence after a long saturating pulse (saturation-ELDOR) that was offset from the observe frequency by 70 MHz is shown in the lower curve of Figure 7.4. The 70 MHz offset corresponds to saturation of one hyperfine line and observation on an adjacent line. The recovery time of the microwave switch on the output of the power amplifier after a long sustained pulse was about 1 μs. This resulted in some artifacts in the spectra acquired at times less than about 1 μs. Subtraction of the background signal (both pump and observe were set off resonance) revealed an initially decaying signal with a time constant of about 8 μs which subsequently began rising with a time constant of about 32 μs.

The intensity of the monitor echo in the absence of magnetization transfer, Y_{ref}, was measured by setting $\Delta\nu = 300$ MHz. With $\Delta\nu = 300$ MHz, the echo was a simple 2-pulse echo. The magnitude of the echo intensity reduction due to magnetization transfer was calculated as reduction = $(Y_{min}-Y_{ref})/Y_{ref}$ where Y_{min} is defined in Figure 7.4. As the length of the pump pulse was increased from 3 to about 30 μs, the reduction increased approximately exponentially with the pump pulse length. Increasing the length of the pump pulse from 30 to 96 μs had no significant impact on the reduction. Based on the dependence of the reduction on

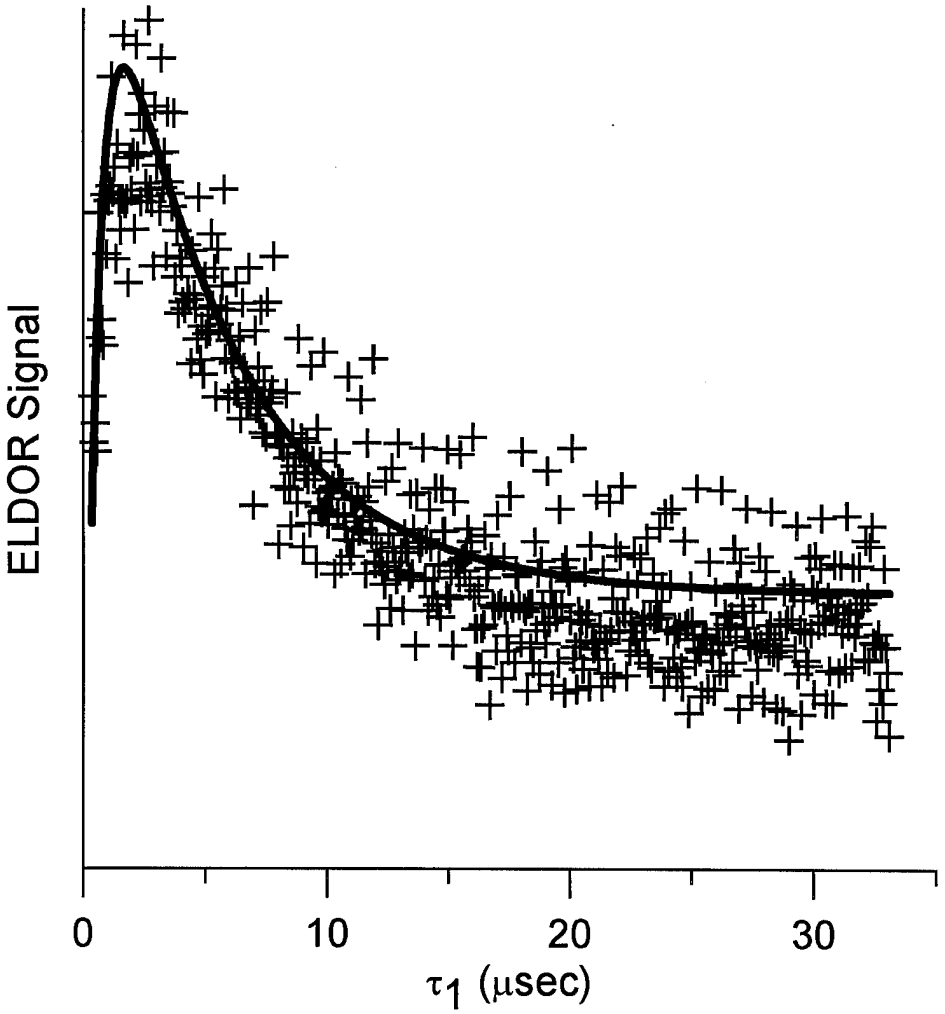

FIG. 7.3. Two-frequency ELDOR signal for L-alanine single crystal in S-band re-entrant LGR overcoupled to Q of approximately 60. (+) denotes signal and (-) denotes simulation. The simulation model is $Signal = (Ae^{-\frac{1}{5.3}t} - Be^{-\frac{1}{0.53}t}) + C$ where A, B, C are constants, and t is time in μs. Experimental parameters: observe frequency, 3.0706 GHz; pump frequency, 3.1406 GHz; number of scans, 40.

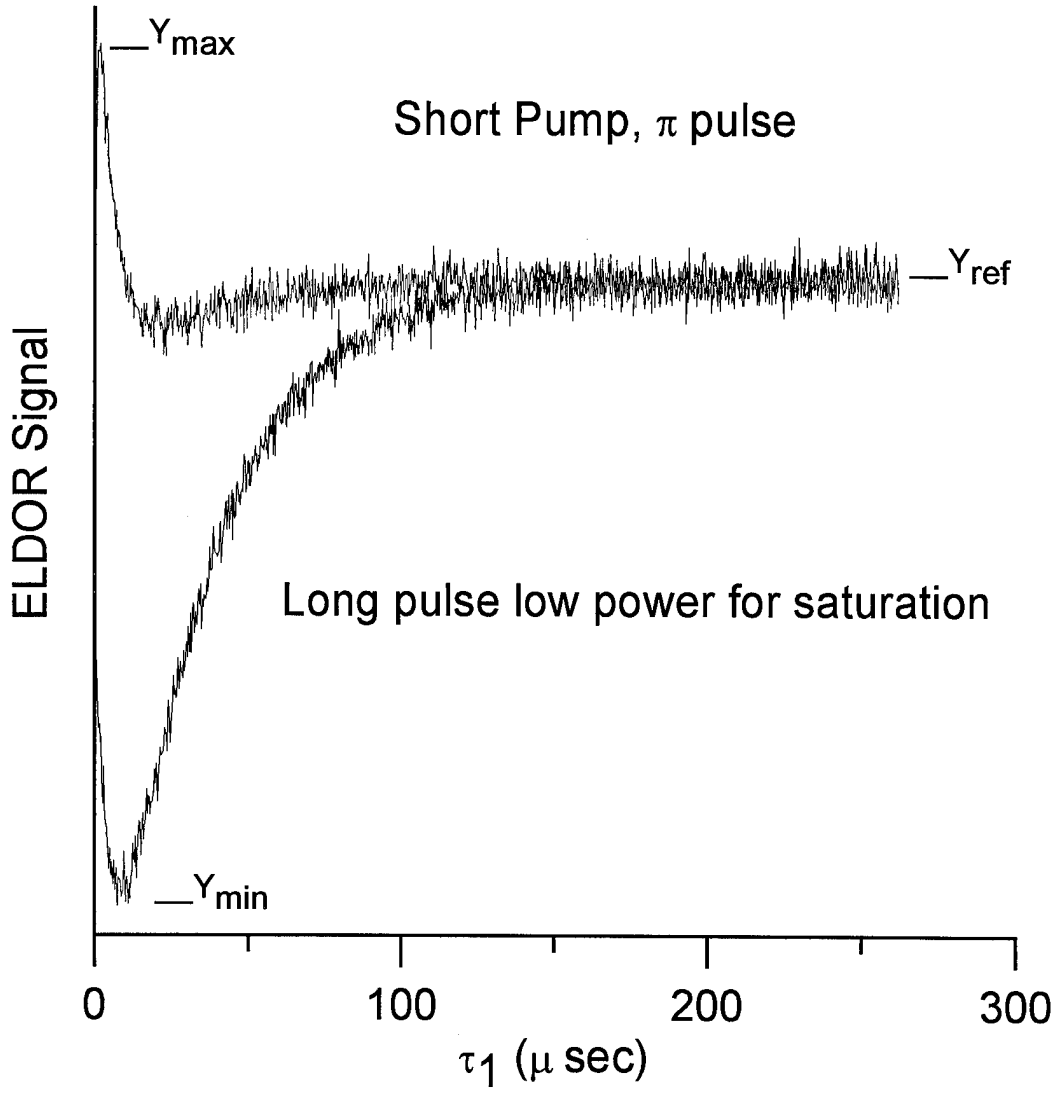

Figure 7.4. Two-frequency pulsed ELDOR signal for irradiated polycrystalline L-alanine.

the length of the pump pulse, the time constant for transfer of magnetization that results in reduction of the intensity of the monitor echo was estimated to be between 5 and 10 μs. The maximum (limiting) value of the reduction was 14%. The observation that this process can be saturated indicated that it was occurring within the irradiated L-alanine spin system.

7.3.2 Irradiated α-aminoisobutyric acid

An inversion-recovery sequence using 64 ns- τ_1 -32 ns -τ_2 - 64 ns microwave pulses yielded a signal that recovered with three time constants of approximately 2, 6, and 20 μs. These times were the same, within experimental error, as the values obtained in the inversion-recovery sequence presented in chapter six. When the pulse lengths were changed to 96 μs -τ_1 - 32 ns - τ_2 - 64 ns, and the first long-pulse power was reduced, the three resultant recovery times were 2, 11, and 41 μs.

The inversion-ELDOR experiments (Δfrequency = 60 MHz) yielded results similar to the pulsed STELDOR experiments in chapter 6 and showed about a 2% enhancement of the monitor echo at the highest point as compared with Y_{ref}. The enhancement grew in with a time constant of ca. 0.2 μs, and decayed with a time constant of ca. 10 μs. The saturation-ELDOR experiments (Δfrequency = 60 MHz) showed an initial decay with a time constant of about 10 μs, and a subsequent recovery with a time constant of about 46 μs. The saturation-ELDOR reduction at Y_{min} was about 10%.

7.4 Discussion

7.4.1 Pulsed STELDOR vs. two frequency pulsed ELDOR

The inversion-ELDOR experiments described in this chapter and the pulsed STELDOR in chapter 6 yielded the same time constants, within experimental error. For the case in which $\Delta\nu$ was less than the bandwidth of the resonator, the 2-frequency ELDOR experiment was the method of choice, because the experiments could be performed faster. Inversion-ELDOR experiments had fewer artifacts, less instrument dead-time, and data collection was faster by two orders of magnitude. Inversion-ELDOR was faster because unlike pulsed STELDOR, it was not limited by the high voltage source and or by the time constant of the recharging power capacitor. The increase in speed of data collection allowed for almost a ten-fold increase in signal to noise for the same length of data collection. To achieve the frequency difference (70 MHz) equivalent to the 25 gauss field jump in the pulsed STELDOR experiments, the resonator has to be more overcoupled (to attain a greater bandwidth) in the inversion-ELDOR experiments than in the pulsed STELDOR experiments. This increased overcoupling in the inversion-ELDOR experiments attenuated the monitor echo by 25% from the monitor echo attained in the pulsed STELDOR experiments, but increase in the speed of the experiment more than compensated for the decrease in echo height.

The greatest advantage of the two-frequency ELDOR system was the additional capability of varying the power and duration of the first pump pulse for the saturation-ELDOR experiments. In chapter four, the differences between the IR recovery times and the long pulse SR recovery times showed the necessity of using longer pump times to reduce the effects of spectral diffusion in studying T_1 relaxation of irradiated L-alanine. Although the long pulse SR data stabilized with

pump times above 200 μs, the recovery was a multi-exponential signal with uncertainties about how to assign the different relaxation signal components. The same time-scale effects are evident in the two-frequency pulsed ELDOR, but unlike the long pulse SR signal, in the saturation-ELDOR the effects of the individual relaxation processes contribute to the observed time dependence with different signs making it easier to separate the components.

REFERENCES

1. B. H. Robinson, D. A. Hass, and C. Mailer, *Science*, **263**, 490 (1994).

2. D. A. Haas, T. Sugano, C. Mailer, and B. Robinson, *J. Phys. Chem.*, **97**, 2914 (1993).

3. G. Rius and A. Hervé, *Solid State Comm.* **15**, 421 (1974).

4. M. Nechtschein and J. S. Hyde, *Phys. Rev. Lett.* **24**, 672 (1970).

5. J. S. Hyde, W. Froncisz, and C. Mottley, *Chem. Phys. Lett.*, **110**, 621 (1984).

6. L. Kevan and L. D. Kispert, "Electron Spin Double Resonance Spectroscopy", John Wiley & Sons, New York, 1976.

CHAPTER EIGHT

Relaxation Times in Irradiated Organic Solids

8.1 Introduction

There is a qualitative understanding that processes variously called spectral diffusion and/or cross-relaxation can affect time-domain EPR measurements. Under certain conditions, experiments to measure T_1 and T_2 actually give an estimate of other physical processes. Although the literature is extensive, very few quantitative measures of the relevant time constants are available. Leading references can be found in several books (*1-3*). Early studies emphasized the contribution of cross-relaxation (*4*) to T_1 measurements in doped ionic solids in the helium temperature range (*1*). Recent nitroxyl radical T_1 measurements in fluid solution were interpreted in terms of competition between electron T_1 and proton T_1 relaxation pathways (*5*). The impact of spectral diffusion on T_1 and T_2 measurements is illustrated in the multifrequency study of the radical in irradiated L-alanine described in chapter 5.

Multiple techniques, each providing a different perspective on spin diffusion and relaxation are applied in this dissertation to radicals in irradiated organic solids. The goal is to measure as directly as possible the rates of spectral diffusion and to understand these rates in terms of physical mechanisms. The apparent relaxation time constants measured in chapters six and seven are summarized in Table 8.1. In this chapter, assignments of the time constants to the physical processes are discussed and values of the fundamental time constants T_1, T_{1n}, and T_{1x} are estimated by simulating the data with a simplified 4-level model.

Table 8.1 Compilation of Time Constants Calculated by Fits of Experimental data to Sums of Exponentials

Sample	Time Constants (μs)			Method
NBS Coal	11			inversion-recovery
L-alanine				
Single Crystal	0.7	6		inversion-recovery, 32 μs window
	0.7	4	10.7	inversion-recovery, 64 μs window
	0.6	6		pulsed STELDOR ΔB=2.0 mT
Polycrystalline		6	23	CW SR
	0.3	1	8	inversion-recovery, 32 μs window
	0.11	0.57		stimulated echo decay
	0.6	6		pulsed STELDOR ΔB=2.0 mT
	1.0	6	26	ESE detected SR
	0.6	6		inversion-ELDOR
		8	32	saturation-ELDOR
L-alanine-d_7	1.7	6.5		inversion-recovery
α-amino-isobutyric acid	2	6	20	inversion-recovery, 262 μs window
		2	10	inversion-recovery, 60 μs window
	3	11	41	ESE detected SR
	2	10		inversion-ELDOR
		10	46	saturation-ELDOR
	2	10		pulsed STELDOR ΔB=2.0 mT
Malonic acid		10	30	inversion-recovery
dimethyl-malonic acid		5	21	inversion-recovery

8.2 Phase Memory Time

Traditionally, the xy-magnetization decay of the electron spin polarization from two-pulse spin-echo experiments is called the phase memory time, T_m, to distinguish it from the true electron T_2. Any mechanism other than the spin-spin interaction that removes excited spins from the set of spins observed in the echo reduces T_m relative to the true T_2 value. Only in the simplest cases will all the spins excited by the first microwave pulse ($\pi/2$) be refocused by the second microwave pulse (π) and be observed in the echo. More commonly, the excited electron spins exchange energy with nuclear spins in their environment. The fluctuating local magnetic fields due to nuclear spins (which could be attributable to thermal motions as well as nuclear T_2 and T_{1n}) causes rapid spectral diffusion, making true electron-electron T_2 measurements difficult. Also, high concentrations of spins and high-power microwave pulses affect neighboring spins resulting in the phenomenon called instantaneous diffusion (*6*). Physical processes, especially rotation of the molecule in the solid lattice (or in fluid solution), can also affect T_m. Only a degree or so of rotational motion can move the Zeeman resonance of a metal complex sufficiently to affect the T_m (*7*). This physical process can occur within the time between microwave pulses. The collapse of two transitions to one, due to a dynamic process (e.g., methyl rotation or spin relaxation of a coupled spin) also affects T_m. Any of these diffusion mechanisms can be relevant to multiple pulse measurements of relaxation phenomena.

Most unpaired electrons are in an environment containing many nuclear spins. The "true T_2" can be obtained by using a Carr-Purcell-Meiboom-Gill (CPMG) microwave pulse sequence of $\pi/2 - \tau - \pi - 2\tau - \pi - 2\tau - \pi \cdots$, where the first ($\pi/2$) microwave pulse is set 90° out of phase from the rest of the pulses and

the echo amplitude is measured at the center of the 2τ intervals. A CPMG experiment eliminates the effects of spectral diffusion. In the case of irradiated alanine, an X-band experiment using CPMG and 2-pulse ESE experiments yielded a T_2 = 700 ns, and a T_m=157 ns respectively for the same sample (*8*). Since the relaxation mechanisms are largely independent, the rates can be combined linearly as $\frac{1}{T_m} = \frac{1}{T_{dif}} + \frac{1}{T_2}$. A measured T_m = 157 ns can result from T_2 = 700 ns, and T_{dif} = 202 ns. There may be many physical processes and mechanisms contributing to the T_{dif}. One contribution to T_{dif} would be the nuclear T_2, which was estimated by Brustolon and Segre (*9*) from Electron Nuclear Double Resonance (ENDOR) linewidths to be 900 ns at 290 K.

8.3 Longitudinal Relaxation

Whether non-equilibrium populations were induced by a short pulse (e.g., an inverting π pulse) or by a long, low-power saturating microwave pulse (CW saturation in the limit), longitudinal spin relaxation to a Boltzmann distribution can proceed by many mechanisms. A possible mechanism can be the coupling of the electron magnetic moment to the orbital angular momentum or to the nuclear moments. Whenever there is an excited state energy for the spins that matches some available combination of energy transitions in the environment, there can be an effective transfer of energy from the spin system to the environment. These have been described in terms of direct, Raman, and Orbach processes. In some special cases there can be very weak coupling of the electron spin to the "lattice" and long electron spin relaxation times. Relaxation rates that depend linearly on temperature over large temperature ranges have been observed and presumably are due to special coupling to unique modes of the environment (*10*). Nitroxyl

radicals in frozen solution (including frozen solvents at room temperature) and metal complexes with axial symmetry exhibit a T_1 dependence on line position (*11,12*). This dependence on line position is probably due to the coupling of vibrations of the discrete compound to orbital angular momentum. For nitroxyl radicals, deuteration of the radical or deuteration of the solvent caused less than the 20% change in T_1. If motion is factored out, the relaxation times of such species are determined by the characteristics of the compound more than by the their intermolecular chemical or nuclear-spin environment. In contrast, the carbon-centered radicals studied in this dissertation exhibited weak dependence on line position, but strong dependence on substitution of ^2H for ^1H. This is an indication of the dominance of an electron-nuclear dipole (END) mechanism for electron spin relaxation. If the END mechanism dominates, several predictions can be made. If nuclear T_1 (which will be distinguished from electron T_1 by using the notation T_{1n}) is the order of the electron T_1, nuclear spin flips will move electron magnetization between the excited spins and the observed spins (e.g., in ELDOR), or move magnetization away from the observed spins faster than T_1. Thus, an experiment designed to measure the electron T_1 could produce data with a recovery time that includes a component due to T_{1n}. For example, a spin flip of one of the nuclei in a methyl group will move the electron Zeeman energy from one hyperfine line to another. Since the CW SR experiment measures a very narrow band of the spectrum, this transfer of magnetization between the excited line and other lines looks like spin-lattice relaxation and shows up as a multiexponential recovery curve. Spectral diffusion of the sort discussed for T_m can also move magnetization between positions in the spectrum. If the spectral diffusion is in the order of T_1, or detectable within the experimental time, it will also contribute to a

multiexponential recovery signal in a SR or inversion-recovery T_1 measurement. In the case of irradiated alanine, under certain conditions, spectral diffusion, nuclear T_{1n}, and electron T_1 all can contribute to the observed recovery time constant in T_1 measurements. These processes come to full thermal equilibrium to different extents during the first exciting pulse of different techniques for T_1 measurement. If, for example, the electron spin of the alanine radical can relax to the thermal rotation reservoir of the diamagnetic alanine host, it may not be possible to bring all parts of the radical spectrum to equilibrium even after multiple relaxation time constants. Because the inversion recovery echo sequence uses a π excitation pulse that is short compared with pump pulse lengths available in CW SR experiments, the inversion recovery measure of T_1 may yield an effective "T_1" that is substantially shortened by spectral diffusion.

8.4 Analysis of Relaxation Times in Terms of 4-level Model

Since the CW SR experiments yield a multiexponential recovery, we do not know which value measured, if any, is T_1. We know that a CW power saturation study of irradiated alanine reveals that the spectrum does not appear to saturate as readily as would be expected based on the measured T_2 and T_1. In fact, it turns out to be practical to use irradiated alanine as a radiation dosimeter at much higher microwave power, and hence better sensitivity, than one would predict based on the measured T_1 and T_2 values. These observations imply that either the nuclear relaxation time or the cross-relaxation time is shorter than T_1.

When multiple processes contribute to the return of magnetization to equilibrium, the time constants obtained by fitting data to a sum of exponentials (as performed in chapters 6 and 7) can be combinations of the fundamental time

constants T_{1e}, T_{1n}, and T_{1x}. When this occurs, it is equivalent to products of exponentials with the fundamental time constants. To analyze the experimental data and obtain the fundamental time constants, a model is needed that describes the inter-related processes. The analysis of the experimental data was based on a 4-level model (Figure 8.1). Rate equations were derived to describe the return of magnetization to equilibrium by pathways described by four rates: $W_e = 1/(2T_1)$, $W_n = 1/(2T_{1n})$, $W_{x1} = 1/(2T_{x1})$, and $W_{x2} = 1/(2T_{x2})$, where T_{x1} and T_{x2} refer to two cross relaxation pathways. The four resulting linear differential equations were solved numerically using MathCad 6.0 Plus.

The kinetic equations used for transfer of magnetization were previously worked out by Hyde (*13*) and by Kevan and Kispert (*14*). The equations were rederived, and those presented by Hyde were checked to insure they reduced to those presented by Kevan and Kispert when the Heisenberg exchange was zero. The change in the populations of the levels (a) - (d) were expressed with equations [1]-[4].

$$d(na)/dt = + W_e[(nd-na)-(Nd-Na)] - W_n(na-nb) - W_{x2}[(na-nc)-(Na-Nc)] \quad [1]$$

$$d(nb)/dt = + W_e[(nc-nb)-(Nc-Nb)] - W_n(nb-na) + W_{x1}[(nd-nb)-(Nd-Nb)] \quad [2]$$

$$d(nc)/dt = - W_e[(nc-nb)-(Nc-Nb)] - W_n(nc-nd) - W_{x2}[(nc-na)-(Nc-Na)] \quad [3]$$

$$d(nd)/dt = - W_e[(nd-na)-(Nd-Na)] - W_n(nd-nc) - W_{x1}[(nd-nb)-(Nd-Nb)] \quad [4]$$

The notation for the processes are as shown in Figure 8.1. N(level) designates the Boltzmann population of the level and n(level) designates the instantaneous population of the level.

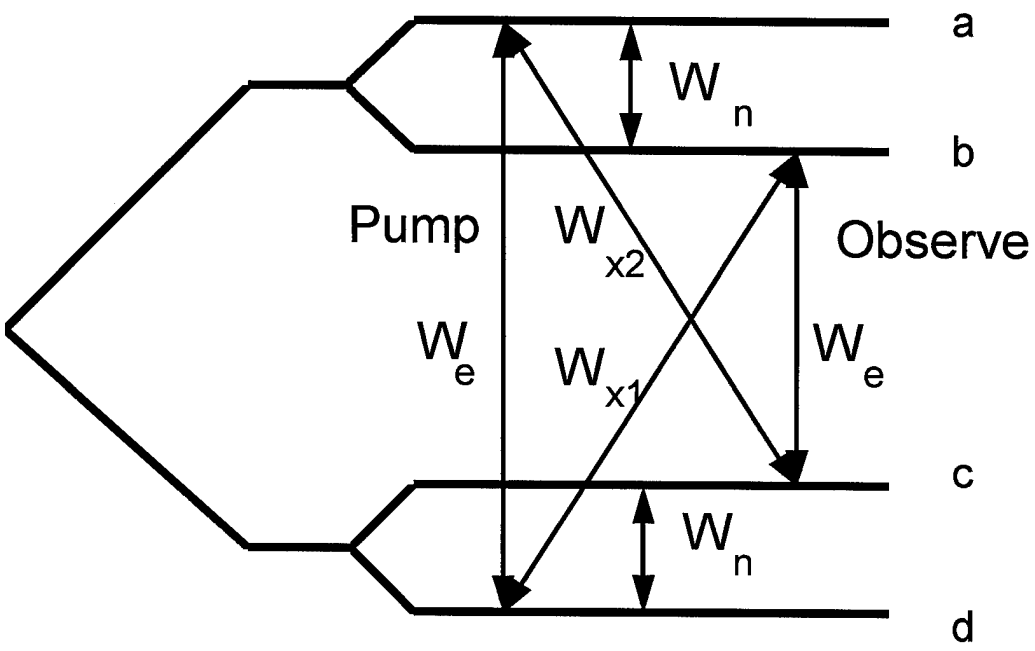

Figure 8.1. Pulsed ELDOR diagram for four level system showing the various relaxation paths. Initial population is a thermal Boltzman distribution where the populations of the levels are: (a), 1-ε; (b), 1-ε; (c), 1; and (d), 1. ε is the Boltzmann population difference between the electron spin states. The population difference between the nuclear spin states are so small compared to the electron population difference that they are assumed to be negligible.

An important time, but not in the equation was the methyl rotation time. Methyl rotation may be the physical process driving many of the different relaxation times in these experiments. According to the report by Dzuba and coworkers, the methyl group rotates about 2.5 x 10^{10} /sec at room temperature (*15*). The near match with EPR microwave frequencies provides for near resonant energy transfer, and could be a physical pathway for the transfer of the alanine radical's spin angular momentum resulting in spectral diffusion.

In working with the model, there were three relevant time periods: a preparation period, an evolution period, and a detection period. The preparation period provided the "initial conditions" present at the start of the evolution period, and the signal obtained during the sampling period described the conditions after a certain length of the evolution period. The differences between CW ELDOR, pulsed ELDOR, STELDOR, etc. are: the initial conditions created by the preparation period, whether microwaves are on during the evolution period, and the method of detecting the signal during the sampling period. Except for the CW SR measurements, which were done in the standard way, there were no microwaves incident on the spins during the evolution period, and the detection was by means of a 2-pulse spin echo sequence. Hence to model the results, we set the initial conditions appropriate to the experiment and used the kinetic equations to calculate the changes during the evolution period. The Boltzmann population of the spin levels after a π microwave pulse inverts from 1-ε for the excited level and 1 for the ground state to 1 for the excited state and 1-ε for the ground state where ε is the Boltzmann population difference between the electron spin states at equilibrium. This distribution is different than after a long saturating long pulse (or CW saturation) which changes both the excited and ground state population to 1-

ε/2, so the observations possible in the pulsed experiment are different from those possible in the CW ELDOR or CW SR experiments.

In the several types of measurements we found relaxation time constants in roughly three ranges for the irradiated organic solids reported in Table 8.1, <2 μs, 6-11 μs, and 20-50 μs. These can contribute to the detected echo signal in different experiments with different signs which helped identify them. The set of samples did not include all combinations one would like to test, but the selection did include species with and without methyl groups, and methyl groups with and without other protons in the radical. Each was embedded in a proton-rich matrix of the diamagnetic parent compound. For L-alanine, the comparison can be made between ^{1}H and ^{2}H. Some relaxation time measurements were available from other labs to help limit the possible assignments and/or help complete the picture of relaxation in these solids.

8.4.1 Irradiated L-alanine and α-aminoisobutyric acid

The spin system in irradiated alanine radical system is complex. A 4-level system of one electron spin and one nuclear spin (Figure 8.1) was used as a simplified model. The methyl group is rotating very rapidly, averaging the otherwise non-equivalent couplings. The three methyl protons and the α-proton are accidentally equivalent, yielding approximately a 5-line pattern at room temperature. We take one pair of these lines and treat them as a doublet, such as would result from any one of the 4 protons individually. Additional nuclear spins will need to be included to fully explain the experimental data.

It was necessary to fit all the irradiated L-alanine data simultaneously. Each experiment put restrictions on the time constants and assignments of the time

constants. The saturation-ELDOR combined with CW SR data provided T_{1n} and T_{1e} values, the pulsed STELDOR and inversion-ELDOR provided the T_{x1} value, and all combined to show that T_{x2} processes are insignificant in this system.

In the inversion-ELDOR experiment the populations of levels a and d were inverted by the first microwave pulse and the intensity of the transition from c to b was monitored. In the experimental data for irradiated L-alanine (Figure 8.2) the intensity of the monitor echo increased to Y_{max} with an apparent time constant of 0.6 μs, then decreased with an apparent time constant of 6 μs and finally returned to Y_{ref} with a longer time constant. The process that caused the initial increase in echo intensity was transfer of magnetization from level b to level d. This was a cross-relaxation process with a rate that was designated as W_{x1}. The data showed the effects of two other processes, but based only on these data it was not possible to determine which one was W_n and which was W_e.

In the saturation ELDOR experiment for the populations of levels a and d were equalized (transition was saturated) by the long low-power pulse and the intensity of the transition between c and b was monitored. In the experimental data for irradiated L-alanine (Figure 8.3) the intensity of the monitor echo immediately after the instrument dead time was smaller than Y_{ref}. The intensity initially decreased with an apparent time constant of 6 μs and then returned to Y_{ref} with an apparent time constant of 32 μs. The initial decrease in echo intensity was due primarily to transfer of magnetization from level c to d, which was a W_n process. The slow return to Y_{ref} was the W_e process. Thus by comparison of the inversion-ELDOR and saturation-ELDOR data it was possible to uniquely assign the three relaxation processes. All three of these processes contributed to the

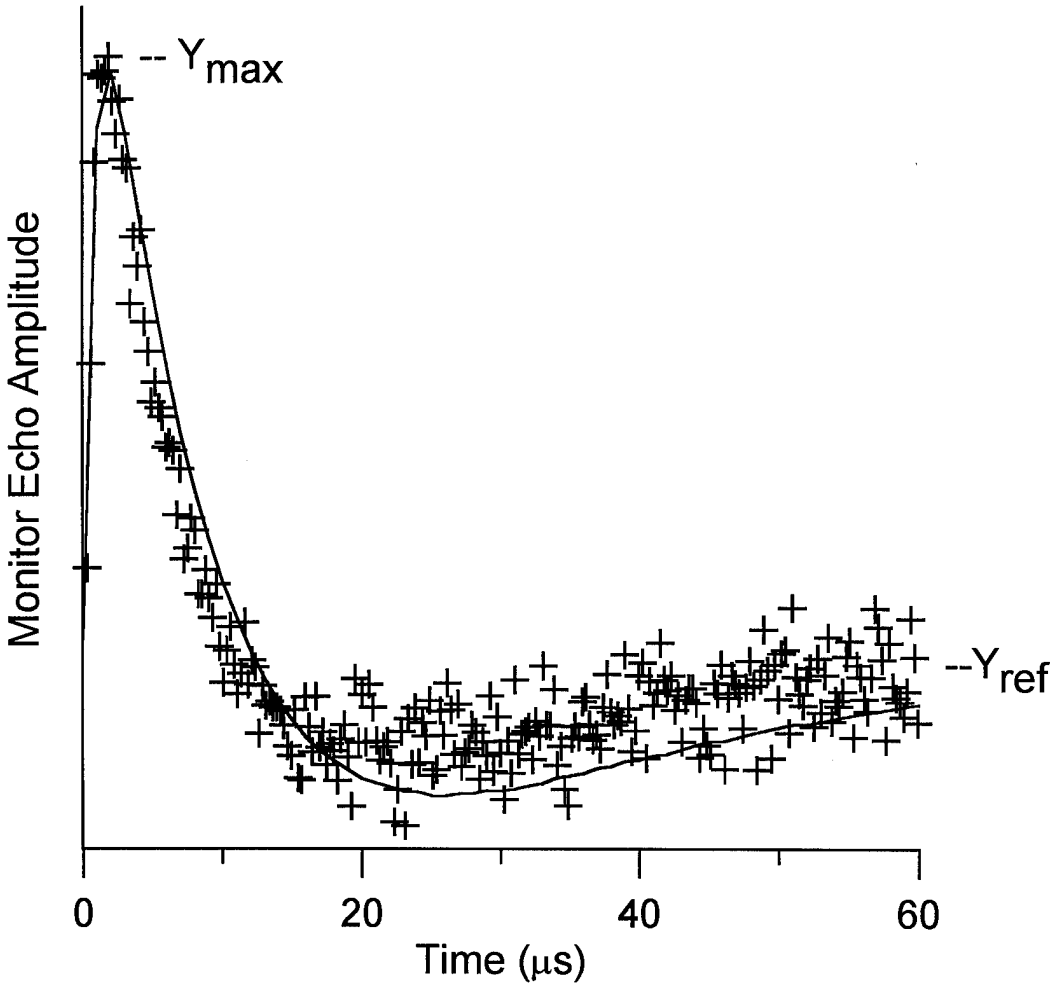

Figure 8.2. Simulated (—)and experimental (+) inversion-ELDOR signal for irradiated L-alanine. The experimental data is the inversion ELDOR signal presented in Figure 7.4. The time constants used in the model were T_{1e} = 240 μs, T_{1n} = 10 μs, and T_{x1} = 0.6 μs. The inverting pulse was applied to the transition between a and d, and the intensity of the transition between c and b was calculated. The initial populations of the levels (Figure 8.1) were (a), 1; (b), 1-ε; (c), 1; and (d), 1-ε. ε is the Boltzmann population difference between the electron spin states at equilibrium.

recovery times observed in the CW saturation data for irradiated L-alanine (Figure 8.4).

The apparent time constants are not equal to the fundamental time constants so the values of the fundamental time constants in the curves simulated based on the 4-level model were adjusted to simultaneously fit to 3 types of experimental data. Due to the noise in the experimental data, non-linear least-squares fits of simulations to experiments have not yet been attempted. Parameters were adjusted to get reasonable match with the experimental data, but further work will be needed to get optimum values. To show some of the uncertainty, two sets of simulation parameters are shown in Figures 8.3 and 8.4. In both sets of simulations $T_1 = 240$ μs and $T_{x1} = 0.6$ μs. A value of $T_{1n} = 10$ μs gave better agreement with the saturation-ELDOR data, while $T_{1n} = 12$ μs gave better agreement with the CW SR data. T_{x2} was $>> T_1$.

The simulations of the inversion-ELDOR data for irradiated L-alanine (Figure 8.2) and α-aminoisobutyric acid (Figure 8.5) were overlayed by scaling the y-axes. The shape of the calculated curves were in reasonable agreement with experiments, but the magnitude of $(Y_{max} - Y_{ref})/Y_{ref}$ in the calculated curves were about 0.40 for both samples whereas the experimental values were 0.05 to 0.07 for irradiated L-alanine and about 0.02 for α-aminoisobutyric acid. The inversion-recovery data for irradiated L-alanine showed approximately 67% of the observed spins had been inverted. When this was used to estimate the initial populations, the simulation produced a $(Y_{max} - Y_{ref})/Y_{ref}$ magnitude of 24%. The inversion-recovery data for irradiated α-aminoisobutyric acid showed approximately 50% of the observed spins had been inverted. When this was used to estimate the initial populations, the simulation produced a $(Y_{max} - Y_{ref})/Y_{ref}$ magnitude of 21%. This

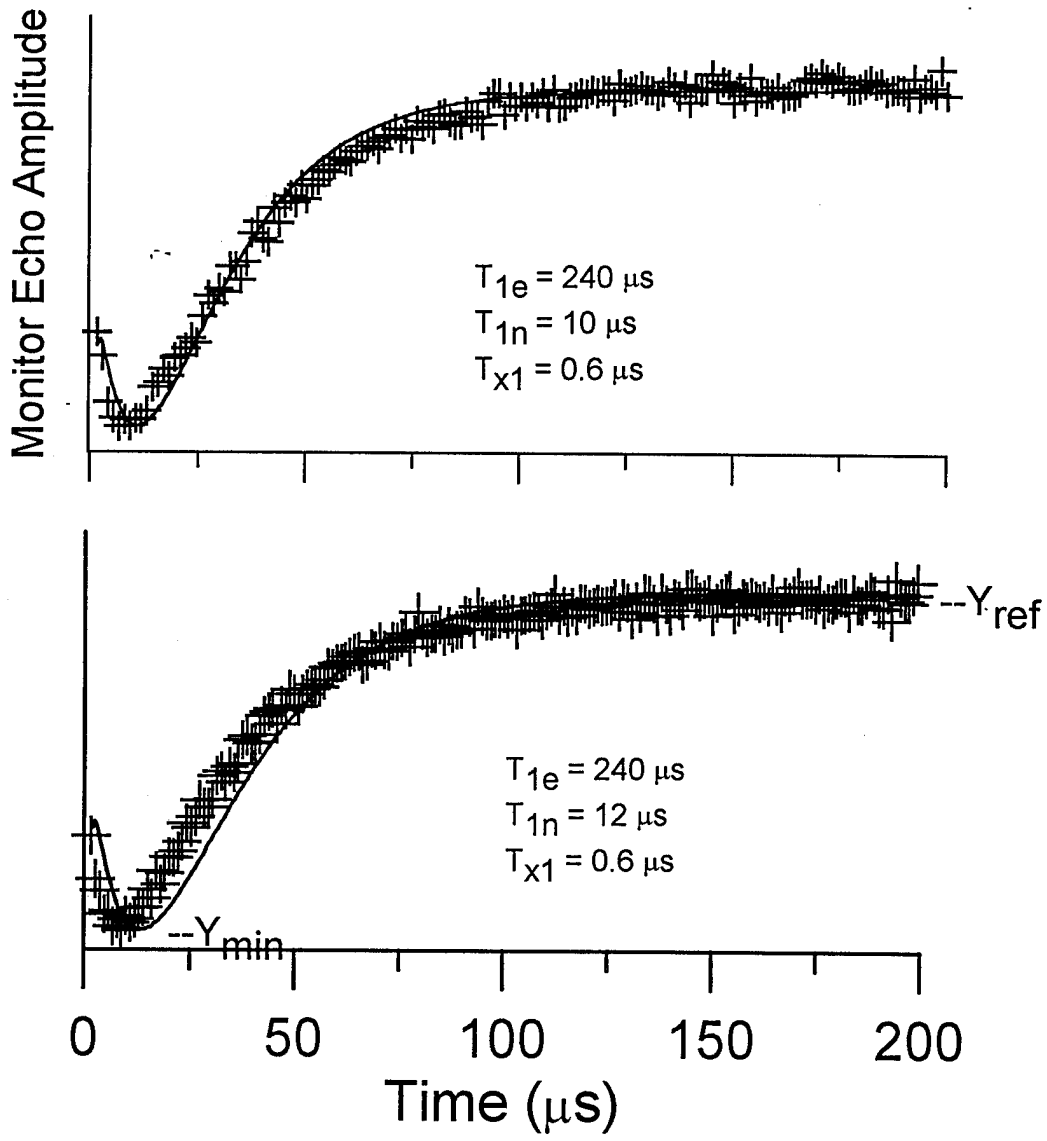

Figure 8.3. Simulated (—) and experimental (+) saturation-ELDOR signal of irradiated L-alanine. The experimental data is the saturation-ELDOR data presented in Figure 7.4. The long saturating pulse equalized the populations of levels a and d and partial transfer of saturation to levels b and c is assumed. The intensity of the transition between c and b was calculated. The initial populations of the levels (Figure 8.1) were: (a), 1-ε/2; (b), 1-0.82ε; (c), 1-0.18ε; and (d), 1-ε/2. ε is the Boltzmann population difference between the electron spin states.

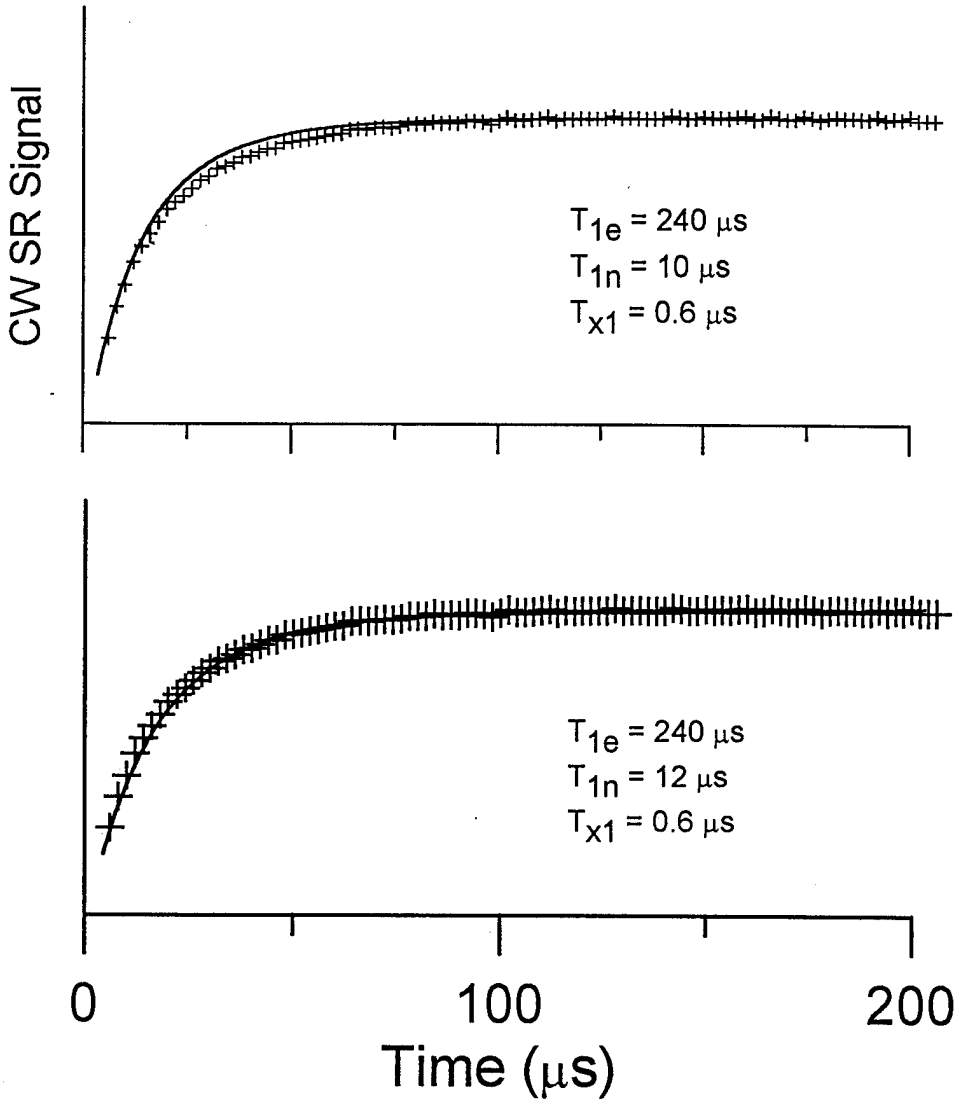

Figure 8.4 Simulated (—) and experimental (+) CW SR signal of irradiated L-alanine. The long saturating pulse equalized the populations of levels a and d and partial transfer of saturation to levels b and c is assumed. The intensity of the transition between levels a and d was calculated to simulate the CW SR signal. The initial populations of the levels (Figure 8.1) were: (a), 1-ε/2; (b), 1-0.82ε; (c), 1-0.18ε; and (d), 1-ε/2. ε is the Boltzmann population difference between the electron spin states.

discrepancy suggested that the 4-level model was too simplistic and additional relaxation pathways for the other L-alanine and α-aminoisobutyric acid lines must be considered to refine the model.

To simulate the saturation-ELDOR data for irradiated L-alanine it was assumed that there was only partial transfer of magnetization from the transition that was saturated to the transition that was observed. The intensity of the echo immediately after the deadtime was strongly dependent on the extent of magnetization transfer. It seems reasonable that magnetization would partially be transferred to other transitions, but this will need to be checked with a more complete model for the spin system.

Simulation of the inversion-ELDOR (Figure 8.5) and saturation-ELDOR (Figure 8.6) data for irradiated α-aminoisobutyric acid resulted in preliminary fundamental time constant values of T_1 =300 ± 60 μs, T_{1n} = 20± 6 μs, T_{x1} = 2.0± 0.4 μs, and $T_{x2} >> T_1$. Obtaining and simulating SR data for irradiated α-aminoisobutyric acid will be needed to get optimum values for the fundamental time constants associated with the radical in α-aminoisobutyric acid.

The model showed that the rate constants obtained by a multiexponential fit to CW SR recovery curves of a sample showing spectral diffusion are not the fundamental rate constants. CW SR rate constants from a sample showing spectral diffusion provide a starting point, and a model must be developed and a simulation must be done on the multiexponential signal to find the fundamental rate constants of the relaxation process. Assigning relaxation times for irradiated L-alanine shows that modeling of data from multiple experimental methods has to be used to assign time constants to fundamental processes and accurately determine the time constants.

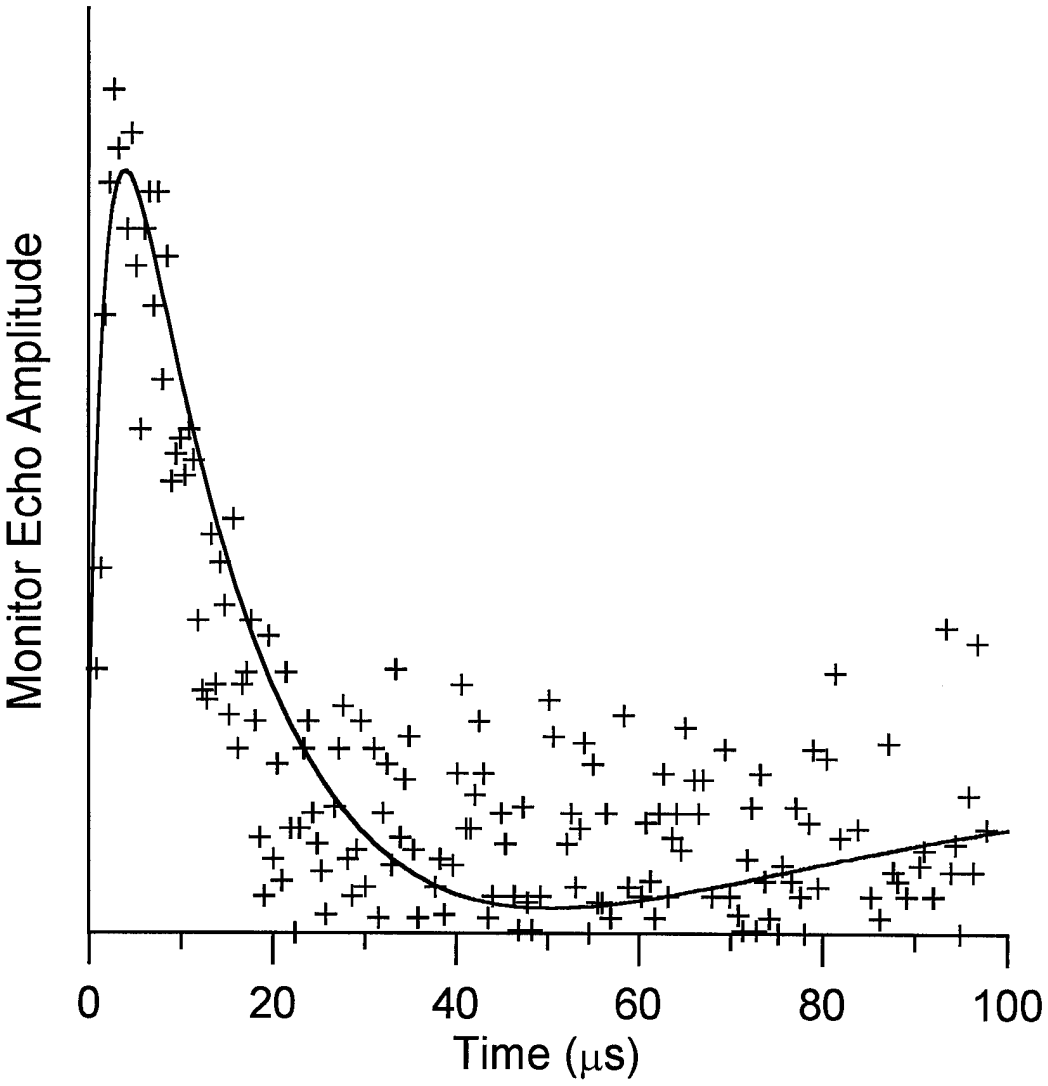

Figure 8.5. Simulated (—)and experimental (+) inversion-ELDOR signal for irradiated α-aminoisobutyric acid. The time constants used in the model were T_{1e} = 300 μs, T_{1n} = 20 μs, and T_{x1} = 2.0 μs. The inverting pulse was applied to the transition between a and d, and the intensity of the transition between c and b was calculated. The initial populations of the levels (Figure 8.1) were (a), 1; (b), 1-ε; (c), 1; and (d), 1-ε. ε is the Boltzmann population difference between the electron spin states at equilibrium.

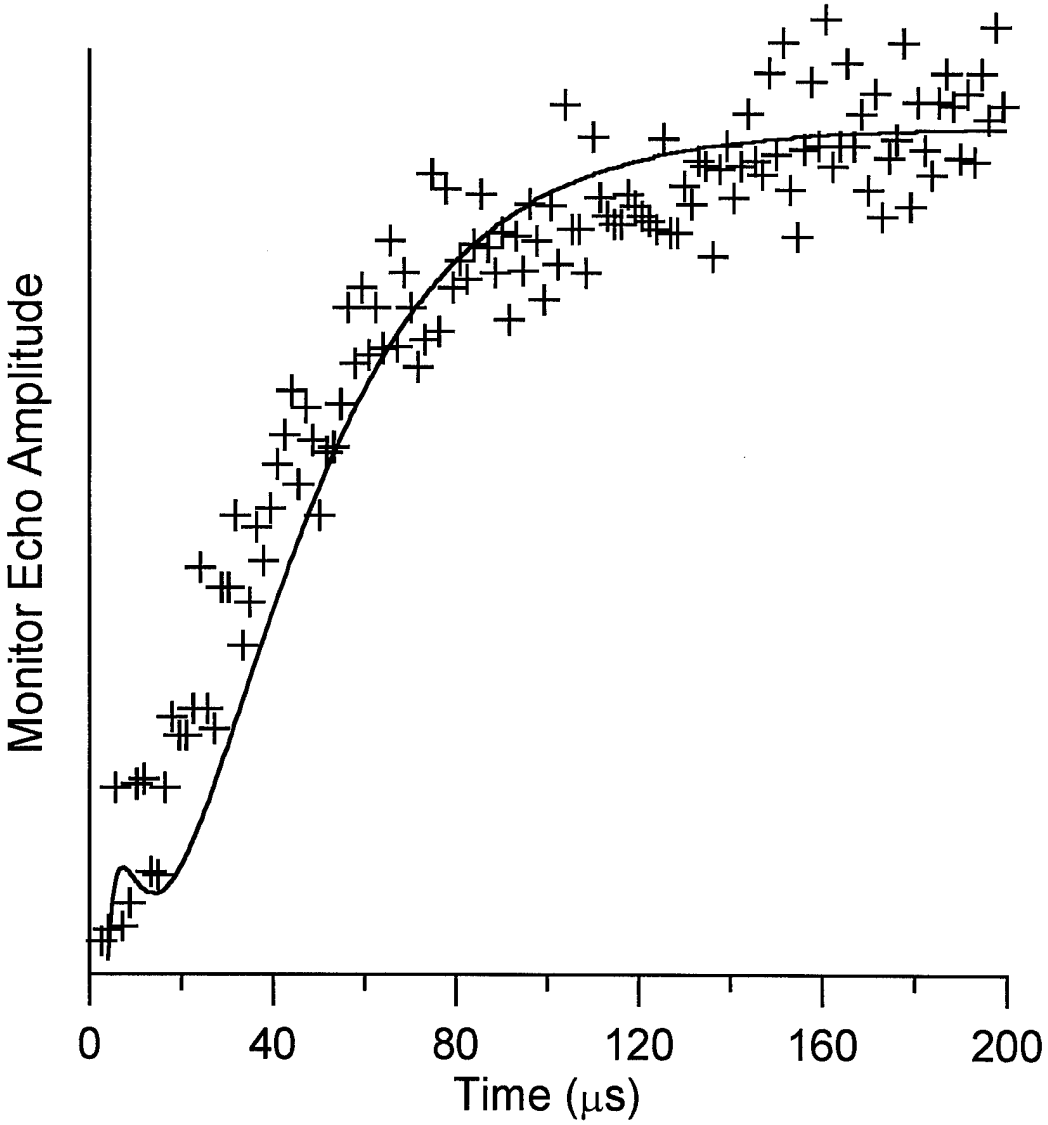

Figure 8.6 Simulated (—) and experimental (+) saturation-ELDOR signal of irradiated α-aminoisobutyric acid. The time constants used in the model were T_{1e} = 300 μs, T_{1n} = 20 μs, and T_{x1} = 2.0 μs. The long saturating pulse equalized the populations of levels a and d and partial transfer of saturation to levels b and c is assumed. The intensity of the transition between c and b was calculated. The initial populations of the levels (Figure 8.1) were: (a), 1-ε/2; (b), 1-0.82ε; (c), 1-0.18ε; and (d), 1-ε/2. ε is the Boltzmann population difference between the electron spin states.

8.4.2 Irradiated L-alanine-d_7

The results for L-alanine-d_7 do not fit the model without the additional consideration of spectral diffusion within the inhomogeneously broadened line. Deuteration is expected to change relaxation rates because the γ for deuterium is 6.5 times smaller than for the proton. Deuterium nuclear relaxation rates have not been directly measured for species comparable to those studied here, but fragmentary data in the literature suggest that T_{1n} values in the microsecond to tens of microsecond range are possible (*16*). A ^2H T_{1n} relaxation time might be as much as 42.5 times longer than for ^1H. However, since the hyperfine nuclear coupling energy for ^2H is 6.5 less than for ^1H, and the smaller hyperfine splitting has 3 lines instead of 2, the resultant increased overlap between the lines may make the spectral diffusion among unresolved ^2H-spin lines as much as 6.5 times faster than in the ^1H analog. Even though T_1 and T_{1n} are longer in L-alanine-d_7 than in the proton analog, spectral diffusion throughout the unresolved line (Figure 6.13) could be fast relative to the experimental times, preventing observation of the tradeoffs between T_{1n} and T_1 evident in the responses of alanine and α-aminoisobutyric acid. In this regard, the radical in irradiated L-alanine-d_7 behaves more like the radicals in coal. No saturation-ELDOR experiment was performed for irradiated L-alanine-d_7, so we do not have this result to compare with the models.

8.4.3 Dimethyl Malonic Acid

There were striking differences in the time-domain experimental observations for the radicals formed by irradiation of α-aminoisobutyric acid and dimethyl malonic acid. Although the CW spectra were similar (chapter 6.3.4), the

time-domain measurements revealed substantial differences, both in relaxation times and in depth of ESEEM. The echo modulation was probably due to intermolecular interactions with protons in the diamagnetic parent species in the lattice. The different intermolecular interaction as shown by T_m and ESEEM will result in different T_1s for the two species if the END mechanism is the main relaxation process. Even if, as reported previously, the chemical composition of the radicals was the same, the different intermolecular interactions can make the spin relaxation environment different.

Enhancement was not seen in the monitor echo amplitude in the pulsed STELDOR and the inversion-ELDOR experiments in dimethyl malonic acid. A saturation-ELDOR experiment suggested a recovery time of 280 μs from Y_{min} (defined in Figure 8.3) to Y_{ref} in the experimental data. However, the longest pump time that was available on the spectrometer (320 μs) was not long enough to saturate the system to achieve true Y_{min}. Thus the initial decrease could not be observed and there was substantial uncertainty in the apparent time constant. The observation of this time constant, which was much longer than the 5 and 21 μs times observed in the inversion recovery curves indicated that spectral diffusion processes are present in the irradiated dimethyl malonic acid. Subsequent experiments will be necessary to explore the spin relaxation properties of the system.

8.4.4 Irradiated Malonic Acid

Nechtschein and Hyde (*17*) measured both T_1 and T_x for a single crystal of irradiated malonic acid, oriented to give maximum intensity of the forbidden lines. They found $T_1 = 40$ μs, and $T_x = 300 \pm 30$ μs. They concluded that the ratio of

T_1/T_x was in good agreement with the intensity ratio of the forbidden/allowed lines. The forbidden lines are expected to be more intense at S-band than at X-band by the square of the frequency difference. The increase in forbidden line intensity was not seen in the S-band CW spectrum, and no enhancement was seen in the pulsed STELDOR experiments. Inversion-recovery experiments failed to show the cross-relaxation time reported by Hyde (*17*), because faster processes dominate the inversion-recovery signal. Simulating an inversion-recovery signal with the 4-level model using $T_{1e} = 40$ μs, $T_{1x} = 300$ μs, $T_{1n} = 300$ μs, and $T_{x2} = 1600$ μs showed a recovery profile dominated by the shorter T_{1e} process. It was reported in chapter five that the apparent T_1 was shorter at S-band than at X-band for irradiated L-alanine. The inversion-recovery time constants of 10 and 30 μs can be strongly influenced by T_{1n} and /or spin diffusion. CW SR and saturation-ELDOR results will be needed before any assignment of relaxation times can be made for this sample.

8.4.5 Coal

The use of the coal sample as a "calibrant" of the pulse STELDOR technique was based on a fundamental assumption that spectral diffusion within the single inhomogeneously broadened line of the coal sample was fast relative to experimental times. The results on the coal sample validated the assumption. Caution should be exercised in extending this assumption to other samples, especially if the spin concentration is significantly less than that of the coal sample, because spectral diffusion can be both intermolecular and intramolecular, requiring only some spin flip that changes the electron Zeeman energy. Our model states that no echo amplitude enhancements or decay will be observed in the ELDOR and

STELDOR experiments if all parts of the line are equilibrated via spectral diffusion during the evolution period.

REFERENCES

1. K. J. Standley and R. A. Vaughn, "Electron Spin Relaxation Phenomena in Solids", Plenum Press, New York, 1969.

2. C. P. Poole, Jr. and H. A. Farach, "Relaxation in Magnetic Resonance", Wiley-Interscience, New York, 1983.

3. L. T. Muus and P. W. Atkins, "Electron Spin Relaxation in Liquids", Plenum Press, New York, 1972.

4. N. Bloembergen, S. Shapiro, P. S. Pershan, and J. O. Artman, *Phys. Rev.* **114**, 445 (1959)

5. B. H. Robinson, D. A. Haas, C. Mailer, *Science*, **263**, 490 (1994).

6. K. M. Salikhov and Yu. D. Tsvetkov, in "Time Domain Electron Spin REsonance" (L. Kevan and R. N. Schwartz, Eds.), Chap. 7, Wiley, New York, 1979.

7. J.-L. Du, G. R. Eaton, and S. S. Eaton, *Appl. Magn. Reson.* **6**, 373 (1994).

8. P. Höfer, K. Holczer, and D. Schmalbein, *Appl. Radiat. Isot.* **40**, 1233 (1989).

9. M. Brustolon, T. Cassol, L. Micheletti, and U. Segre, *Mol. Phys.* **57**, 1005 (1986).

10. J. Turkevitch, J. Soria, and M. Che, *J. Chem. Phys.* **56**, 1463 (1972).

11. J.-L. Du, S. S. Eaton, and G. R. Eaton, *J. Magn. Reson.*, A. **115**, 256 (1995).

12. J.-L. Du, G. R. Eaton, and S. S. Eaton, *J. Magn. Reson.*, A. **117**, 67 (1995).

13. J.-J. Yin and J. S. Hyde, *J. Magn. Reson.* **74**, 82 (1987).

14. L. Kevan and L. D. Kispert, "Electron Spin Double Resonance Spectroscopy", John Wiley & Sons, New York, 1976.

15. S. A. Dzuba, K. M. Salikhov, and Y. D. Tsvetkov, *Chem. Phys. Lett.* **79**, 568 (1981).

16. K. Liu, D. Ryan, K. Nakanishi, and A. McDermott, *J. Am. Chem. Soc.* **117**, 6897 (1995).

17. M. Nechtschein and J. S. Hyde, *Phys. Rev. Lett.* **24**, 672 (1970).

CHAPTER NINE

Future Work

This research provides a method for exploring spin relaxation using multiple frequencies and multiple time-domain experimental techniques. These techniques have been used to characterize an irradiated vitreous silica defect center, and irradiated L-alanine and α-aminoisobutyric acid. These measurements revealed several relaxation times, but it is unlikely that a full picture has emerged. It is necessary to push the range of pulse times, especially with variable temperature experiments at various microwave frequency, to further explore the spin dynamics. Various contributions to relaxation could dominate in different chemical species (e.g. metal complexes, carbon-based radicals, heteroatom-based radicals). There is little information in the literature about the actual mechanisms of spin diffusion or even about the time constants of the processes. Table 9.1 summarizes a list of experiments needed to help complete the analysis of irradiated organic materials started in this dissertation.

In working with lower microwave frequencies (vs. X-band), there is still an unresolved question of sensitivity vs. frequency (*1-5*). The dependence has been reported anywhere from linear to higher-powers (e.g. 2.5), and the true dependence may be crucial in determining whether lower frequencies are a reasonable path to generally pursue in EPR for biological purposes. No one knows what one could expect from a well-designed spectrometer. The difficulty will be eliminating all variables except microwave frequency in making sensitivity measurements. Since lower frequency bridges used in this dissertation are very

Table 9.1 Future experiments on irradiated organic materials

Compound	**S-band experiments**	**X-band experiments**
L-alanine		VT SR inversion-recovery inversion-ELDOR saturation-ELDOR ESE-detected SR
L-alanine-d_7	SR inversion-ELDOR saturation-ELDOR ESE-detected SR T_m	VT SR inversion-recovery inversion-ELDOR saturation-ELDOR ESE-detected SR T_m
α-aminoisobutyric acid	SR ESE-detected SR	VT SR inversion-recovery inversion-ELDOR saturation-ELDOR ESE-detected SR T_m
malonic acid	SR inversion-ELDOR saturation-ELDOR ESE-detected SR T_m	VT SR inversion-recovery inversion-ELDOR saturation-ELDOR ESE-detected SR T_m
dimethylmalonic acid	SR saturation-ELDOR ESE-detected SR	VT SR inversion-recovery inversion-ELDOR saturation-ELDOR ESE-detected SR T_m

similar in design, it may be possible to reduce the variables to a workable number. One of the critical needs is to find the true filling factor, which requires being able to calculate the true perpendicular magnetic component of the microwaves in the resonantor. The copper-film LGR with its consistent construction may be a possible tool in designing a methodology to answer this fundamental question. Also other resonator designs are currently in progress, which will improve signal to noise at lower frequencies.

For the pulsed STELDOR capability, other experimental designs are possible. Whether to use the two-frequency pulsed ELDOR or pulsed STELDOR depends on the needs of the experiment. The tradeoff is between the possible larger separation between points in the spectrum studied by the pulsed STELDOR vs. the higher repetition rate of the two-frequency ELDOR. However, the equipment developed to do pulsed STELDOR has other unique applications. The equipment is currently configured to create a single magnetic field pulse. With minor modifications to include: a modified anti-Helmholtz coil instead of the current modified Helmholtz coil, a larger discharge capacitor with a concurrent larger charging capacitor, and reprogramming of the PTU program; a series of magnetic field gradient pulses could be implemented. These capabilities would permit a series of experiments to examine spin-diffusion effects likened to the spin-diffusion NMR experiments accomplished by Stjeskal and Tanner in the 1960s (*6*).

Another direction currently being pursued is cryogenic capabilities for the MFEPR. Current research projects include placing the pre-amplifier and circulator or other directional devices as well as the resonator and sample into the cryostat to enhance signal to noise. With the development of cryogenic capabilities for the MFEPR, studying the temperature dependence of the spin relaxation may help

identify the role of various mechanisms, such as methyl rotation in the relaxation of irradiated L-alanine and α-aminoisobutyric acid and other species. Placing the pulsed STELDOR equipment in a cryogenic environment will be a tricky engineering feat because the high-current pulse would be transmitted a long distance, and the materials properties change with temperature. The two-frequency pulsed ELDOR could be accommodated more easily. This may help refine and fully characterize the complex relaxation patterns of irradiated organic samples.

The two-frequency pulsed ELDOR shows great promise for measuring spin relaxation effects. The engineering of two-frequency pulsed ELDOR systems is already in progress for the other frequencies including X-band. The X-band capabilities will be developed on the X-band ESE spectrometer. A Medical Advances X-band LGR is already available for the X-band instrument and the frequency dependence of the enhancement may answer what contribution methyl rotation, and forbidden transition cross-relaxation effects make to the EPR signal.

The current two-frequency pulsed ELDOR could also be improved to enhance system operation. The current second source for the pump pulse has no automatic frequency control (AFC). Currently, the stability of the source is dependent only on thermal stability and manual dexterity. If an AFC system with external source lock is incorporated into the system; the time for data acquisition could be increased, the signal to noise ratio should be enhanced, and other irradiated organic radicals with perhaps a much smaller enhancement or reduction could be studied. Increasing microwave frequency stability, variable temperature control, and other microwave frequency bands for the two-frequency pulsed ELDOR method would greatly enhance its utility. Also, new designs for

microwave resonators are being considered which will eliminate the bandpass problem of using an LGR for two-frequency pulsed ELDOR.

Most of the engineering items listed above as currently under development involve the efforts of George A. Rinard and Richard W. Quine.

REFERENCES

1. C. P. Poole Jr., "Electron Spin Resonance: A Comprehensive Treatise on Experimental Techniques", Interscience, New York, 1967, p. 550.
2. M. Romanelli, K. Kurshev, and L. Kevan, *Appl. Magn. Reson.*, 7, 427 (1994).
3. J. A. Weil, J. R. Bolton, and J. E. Wertz, "Electron Paramagnetic Resonance: Elementary Theory and Practical Applications", Wiley-Interscience, New York, 1994, p. 471.
4. Y. S. Levedev, in "Modern Pulsed and Continuous-Wave Electron Spin Resonance" (eds. L. Kevan and M. K. Bowman), Wiley-Interscience, New York, 1990, p. 372.
5. H. J. Halpern and M. K. Bowman, in "EPR Imaging and In Vivo EPR" (eds. G. R. Eaton, S. S. Eaton, and K. Ohno), CRC Press, Boca Raton, 1991, p. 45.
6. E. O. Stejskal and J. E. Tanner, *J. Chem. Phys.* **42**, 288 (1965).

APPENDIX

Computer Program For Copper-Film Dimension Calculations

```
REM    CUFILM CALCULATES THE SCALED DRAWING DIMENSIONS
REM    FOR ETCHED LGRs
REM    A SOLDER STRIP IS PROVIDED THAT IS INDEPENDENT
REM    OF THE LGR ETCHES TO HELP LINE UP THE DRAWINGS
REM    FOR ETCHING PURPOSES
REM
DIM S1(20, 20), S2(20, 20), GM(20)
FLY = 40
ZIP = 20
PI = 3.1415926#
EPS0 = 8.85E-12
MU = 4 * PI * .0000001
NMAX = 7
REM    ENTER LGR PARAMETERS AND CONVERT TO RMKS SYSTEM
PRINT " HARD COPY OUTPUT?"
INPUT A$
IF A$ = "y" THEN HC = 1
IF A$ = "Y" THEN HC = 1
PRINT " ENTER LOOP WIDTH IN mm"
INPUT W: WM = W * .001
PRINT "ENTER LOOP DIAMETER IN mm"
INPUT DIA: DIAM = DIA * .001: RM = DIAM / 2
PRINT " ENTER GAP THICKNESS IN Mills"
INPUT T: TM = T * .001 / 39.37
PRINT " ENTER GAP DIELECTRIC CONSTANT"
INPUT EPSR
PRINT "ENTER RESONANT FREQUENCY IN GHz"
INPUT F0
PRINT "ENTER DRAWING SCALE FACTOR"
INPUT DSF
CON = 39.37 * 1000 * DSF
PRINT "WHEN LOOP HAS EVEN NUMBER OF TOTAL GAPS,"
PRINT "THE FREE END GAP HAS TWICE THE THICKNESS"
PRINT
REM    CALCULATE CIRCUMFERENCE
CIRM = 2 * PI * (RM + TM)
REM    CALCULATE CIRCUMFERENCE IN WAVELENGTHS
CIRWL = CIRM * 1000 * F0 / 300
REM    CALCULATE INDUCTANCE
```

```
L = MU * PI * RM ^ 2 / (WM + .9 * RM)
REM    CALCULATE C
OMEGA0 = 2 * PI * F0 * 1E+09
C = 1 / OMEGA0 ^ 2 / L
REM    CALCULATE PATTERN DIMENSIONS
FOR N = 1 TO NMAX
GM(N) = N * C * TM / EPSR / EPS0 / (WM + TM) - TM
FM = (CIRM - (N + (N + 1) MOD 2) * GM(N)) / N
IF FM < 0 THEN
        NMAX = N - 1
        GOTO 99
END IF
FOR I = 1 TO N
IF N = 1 THEN
        S1(1, 1) = FM + 2 * GM(N)
        S2(1, 1) = FM + 2 * GM(N)
ELSEIF I = 1 THEN
                IF N MOD 2 = 0 THEN
                S1(N, I) = FM + 3 * GM(N)
                S2(N, I) = FM + 2 * GM(N)
                ELSE
                S1(N, I) = FM + 2 * GM(N)
                S2(N, I) = FM + GM(N)
                END IF
ELSEIF I = N THEN
        IF N MOD 2 = 0 THEN
                S1(N, I) = FM + 2 * GM(N)
                S2(N, I) = FM + 3 * GM(N)
                ELSE
                S1(N, I) = FM + 2 * GM(N)
                S2(N, I) = FM + GM(N)
                END IF
ELSEIF I MOD 2 <> 0 THEN
        S1(N, I) = FM + 2 * GM(N)
        S2(N, I) = FM
ELSE
        S1(N, I) = FM
        S2(N, I) = FM + 2 * GM(N)
END IF
NEXT I
PRINT
PRINT "N= "; N; " LOOP CIRCUMFERENCE= "; CIRM * 39.37; " INCHES", "
GAP= "; GM(N) * 39.37 * 1000; "Mills"
```

```
PRINT " FM= "; FM
NEXT N

99 PRINT
PRINT "W= "; W; "mm"; "  DIA= "; DIA; " mm"; "  T= "; T; "Mill"; "  EPSr= ";
EPSR
PRINT "L= "; L; "  C= "; C; "  Fo= "; F0; " GHz"
FOR N = 1 TO NMAX
PRINT
PRINT "N= "; N
PRINT " I          S1          S2"
FOR I = 1 TO N
PRINT I, S1(N, I) * 39.37, S2(N, I) * 39.37
NEXT I
NEXT N
IF HC = 0 THEN GOTO 9999
LPRINT
LPRINT "W= "; W; "mm"; "  DIA ="; DIA; " mm"; "  T= "; T; "Mills"; "  EPSr=
"; EPSR
LPRINT "L= "; L; "  C= "; C; "  Fo= "; F0; " GHz"
LPRINT
LPRINT "CIRCUMFERENCE IN WAVELENGTHS = "; CIRWL
LPRINT
LPRINT "All Dimensions Below in Mills:"
LPRINT
LPRINT "CONDUCTOR WIDTH= "; W / 25.4 * 1000
LPRINT
LPRINT "First Segment of Side 1 is a Conductor -- Dimensions are WIDTHS in
mills"
FOR N = 1 TO NMAX
        TL1 = 0
        TL2 = 0
        LPRINT
        LPRINT "N= "; N, "Side 1        Side 2"
        FOR I = 1 TO N
                LPRINT I, S1(N, I) * 39.37 * 1000, S2(N, I) * 39.37 * 1000
                TL1 = TL1 + S1(N, I) * 39.37 * 1000
                TL2 = TL2 + S2(N, I) * 39.37 * 1000
        NEXT I
        LPRINT "Total Length", TL1, TL2, "Gap Width ="; GM(N) * 39.37 *
1000
NEXT N
REM   NOW CALCULATE THE SCALED DRAWING DIMENSIONS
```

```
LPRINT CHR$(12)
LPRINT "W= "; W; "mm"; "  DIA ="; DIA; " mm"; "  T= "; T; "Mills"; "  EPSr=
"; EPSR
LPRINT "L= "; L; "  C= "; C; "  Fo= "; F0; " GHz"
LPRINT
LPRINT "CIRCUMFERENCE IN WAVELENGTHS = "; CIRWL
LPRINT
LPRINT "Dimensions Below are Coordinantes in Mills for the Drawing with Scale
Factor = ";
LPRINT USING "##"; DSF
LPRINT
LPRINT "CONDUCTOR WIDTH= ";
LPRINT USING "#####"; W / 25.4 * 1000 * DSF
LPRINT
LPRINT "First Segment of Side 1 is Conductor"
FOR N = 1 TO NMAX
        LPRINT
        LPRINT "N= "; N, "Side 1          Side 2", "Gap Width ="; GM(N) * 39.37
* 1000 * DSF
        TL1 = 0
        TL2 = 0
        FOR I = 1 TO N + 3 - N MOD 2
        IF I MOD 2 = 0 THEN
                S1$ = "Diel."
                S2$ = "Cond."
        ELSE
                S1$ = "Cond."
                S2$ = "Diel."
        END IF
                IF N MOD 2 <> 0 THEN
                        IF I = 1 THEN
                                TL2 = TL2 + FLY * DSF + GM(N) * CON
                        ELSEIF I = 2 THEN
                                TL2 = TL2 + ZIP * DSF
                        ELSEIF I = 3 THEN
                                TL2 = S2(N, I - 2) * CON
                        ELSEIF I > N + 2 THEN
                                TL2 = 0
                        ELSE
                                TL2 = TL2 + S2(N, I - 2) * CON
                        END IF
                        IF I - 2 = N THEN TL2 = TL2 + (FLY + ZIP) * DSF
                        IF I = N + 1 THEN
```

```
                    TL1 = TL1 + FLY * DSF
                ELSEIF I = N + 2 THEN
                    TL1 = TL1 + ZIP * DSF
                ELSEIF I > N + 2 THEN
                TL1 = 0
                ELSE
                    TL1 = TL1 + S1(N, I) * CON
                END IF
        ELSE
                IF I = 1 THEN
                    TL2 = TL2 + FLY * DSF + 2 * GM(N) * CON
                ELSEIF I = 2 THEN
                    TL2 = TL2 + ZIP * DSF
                ELSEIF I = 3 THEN
                    TL2 = S2(N, I - 2) * CON
                ELSE
                    TL2 = TL2 + S2(N, I - 2) * CON
                END IF
                    IF I = N + 3 THEN TL2 = TL2 + (FLY + ZIP) *
DSF
                IF I = N THEN
                    TL1 = TL1 + S1(N, I) * CON + FLY * DSF
                ELSEIF I = N + 1 THEN
                    TL1 = TL1 + ZIP * DSF
                ELSEIF I > N + 1 THEN
                TL1 = 0
                ELSE
                    TL1 = TL1 + S1(N, I) * CON
                END IF
        END IF
            LPRINT I,
            LPRINT USING "#####  "; TL1;
            LPRINT S1$; "    ";
            LPRINT USING "#####  "; TL2;
            LPRINT S2$
            NEXT I
NEXT N
LPRINT CHR$(12)

9999 END
```

Electron Spin Relaxation in Irradiated Solids

An Abstract of a Dissertation

Presented to

the Faculty of Natural Sciences, Mathematics, and Engineering

University of Denver

In Partial Fulfillment

of the Requirements for the Degree

Doctor of Philosophy

---

by

Barnard Tongjoo Ghim

Major, United States Air Force

March 1996

163 pages

Abstract

This investigation has four separate sections related to analysis of irradiated materials using pulsed electron paramagnetic resonance (EPR) techniques.

The first part documents the design and fabrication of versatile loop-gap resonators (LGR) made of copper-film (CuFlon®) for use at various microwave frequencies. The LGRs are almost transparent to 100 KHz magnetic field modulation used in CW-EPR and allow 90% transmission of a 200 ns magnetic field pulse (2.5 mT) used in stepped-field electron-electron double resonance (STELDOR) experiments.

The second part is a multi-frequency investigation of the E' center of irradiated vitreous silica. The longitudinal relaxation time, T_1, changed little between 1.1 and 9.1 GHz, but was systematically longer at 19.4 GHz. T_1 was dependent upon orientation, with T_1 values decreasing about 50% between the parallel and perpendicular orientations of the g-tensor with respect to the external magnetic field.

The third part is a multi-frequency CW and time-domain EPR investigation of irradiated L-alanine which is used as a dosimeter for radiation. The time-domain EPR analysis shows the presence of spectral diffusion.

The fourth part is the development and use of ELDOR techniques to study the spectral diffusion in irradiated L-alanine and other irradiated organic solids. Pulsed STELDOR, and pulsed two-frequency ELDOR methods were developed and the details of the implementation is reported. The assignment of relaxation times that gave the best simulation of the experimental data was an electron relaxation time of 240 μs, a nuclear relaxation time of 10-12 μs, and a cross-relaxation time of 0.6 μs. The results showed the power of a multi-method analysis and simulation to assign relaxation times for samples exhibiting spectral diffusion.

REFERENCES

J. M. Arber, P. H. G. Sharpe, H. A. Joly, J. R. Morton, and K. F. Preston, *Appl. Radiat. Isot.* **42**, 665 (1991).

P. T. Callaghan, A. Coy, E. Dormann, R. Ruf, and N. Kaplan, *J. Magn. Res.* A., **111**, 127 (1994).

S. A. Dzuba, A. G. Maryasov, K. M. Salikhov, and Y. D. Tsvetkov, *J. Magn. Res.*, **58,** 95 (1984).

B. T. Ghim, S. S. Eaton, G. R. Eaton, R. W. Quine, G. A. Rinard, and S. Pfenninger, *J. Magn. Reson.* A, **115**, 230 (1995).

J. Gorcester and J. H. Freed, *J. Chem. Phys.* **88,** 4678 (1988).

J. P. Hornak and J. H. Freed, *Chem. Phys. Lett.* **101**, 115 (1983).

J. S. Hyde and W. Froncisz, *Ann. Rev. Biophys. Bioeng.* **11**, 391 (1982).

L. Kevan and R. N. Schwartz, "Time Domain Electron Spin Resonance", Wiley-Interscience, New York, 1979.

S. Pfenninger, A. Schweiger, J. Forrer, and R. R Ernst, *XXIII Con. Amp. on Magn. Res.* 568 (1986).

C. P. Poole Jr., "Electron Spin Resonance: A Comprehensive Treatise on Experimental Techniques", Wiley-Interscience, 1967, 2nd. edition, Wiley, New York, 1983.

S. K. Rengan, V. R. Bhagat, V. S. S. Sastry and B. Venkataraman. *J. Magn. Reson.* **33**, 227 (1979).

A. Schweiger, *Angew. Chemie. Int. Ed. Engl.*, **30**, 265 (1991).

A. Schweiger, *in* "Modern Pulsed and Continuous-wave Electron Spin Resonance", (L. Kevan and M. K. Bowman eds.) John Wiley & Sons, New York, 43 (1990).

G. A. Sierra, A. Schweiger, and R. R. Ernst, *Chem. Phys. Lett.* **184**, 363 (1991).

C. P. Slichter, "Principles of Magnetic Resonance", 3rd. edition, Springer-Verlag, Berlin, 1992.

J. E. Wertz, J. R. Bolton, and J. E. Wertz, "Electron Spin Resonance", Wiley-Interscience, New York, 1994.